UNIVERSIDADE ESTADUAL DE CAMPINAS
Faculdade de Engenharia Elétrica e de Computação

Fernando Darío Almeida García

Analytical Contributions for Modern Radar Systems

Contribuições Analíticas para Sistemas de Radar Modernos

Campinas

2021

UNIVERSIDADE ESTADUAL DE CAMPINAS
Faculdade de Engenharia Elétrica e de Computação

Fernando Darío Almeida García

Analytical Contributions for Modern Radar Systems

Contribuições Analíticas para Sistemas de Radar Modernos

Thesis presented to the School of Electrical and Computer Engineering of the University of Campinas in partial fulfillment of the requirements for the degree of Doctor in Electrical Engineering, in the area of Telecommunications and Telematics.

Tese apresentada à Faculdade de Engenharia Elétrica e de Computação da Universidade Estadual de Campinas como parte dos requisitos exigidos para a obtenção do título de Doutor em Engenharia Elétrica, na Área de concentração: Telecomunicações e Telemática.

Supervisor/*Orientador*: Prof. Dr.
José Cândido Silveira Santos Filho

Este exemplar corresponde à versão final da tese defendida pelo aluno Fernando Darío Almeida García, e orientada pelo Prof. Dr. José Cândido Silveira Santos Filho.

Campinas

2021

Ficha catalográfica
Universidade Estadual de Campinas
Biblioteca da Área de Engenharia e Arquitetura
Rose Meire da Silva - CRB 8/5974

García, Fernando Darío Almeida, 1989-
G165a Analytical contributions for modern radar systems / Fernando Darío Almeida García. – Campinas, SP : [s.n.], 2021.

Orientador: José Cândido Silveira Santos Filho.
Tese (doutorado) – Universidade Estadual de Campinas, Faculdade de Engenharia Elétrica e de Computação.

1. Radar. 2. Detectores. 3. Alvos de radar. 4. Processamento de sinais. 5. Detecção de sinais. I. Santos Filho, José Cândido Silveira, 1979-. II. Universidade Estadual de Campinas. Faculdade de Engenharia Elétrica e de Computação. III. Título.

Informações para Biblioteca Digital

Título em outro idioma: Contribuições analíticas para sistemas de radar modernos
Palavras-chave em inglês:
Radar
Detectors
Radar targets
Signal processing
Signal detection
Área de concentração: Telecomunicações e Telemática
Titulação: Doutor em Engenharia Elétrica
Banca examinadora:
José Cândido Silveira Santos Filho [Orientador]
Renato Machado
João Roberto Moreira Neto
Paulo Cardieri
Hugo Enrique Hernández Figueroa
Data de defesa: 26-02-2021
Programa de Pós-Graduação: Engenharia Elétrica

Identificação e informações acadêmicas do(a) aluno(a)
- ORCID do autor: https://orcid.org/0000-0003-3747-1511
- Currículo Lattes do autor: http://lattes.cnpq.br/1169485936295925

COMISSÃO JULGADORA - TESE DE DOUTORADO

Candidato: Fernado Darío Almeida García, RA: 151557

Data da Defesa: 26 de fevereiro de 2021

Título da Tese: "Contribuições Analíticas para Sistemas de Radar Modernos".

Prof. Dr. José Cândido Silveira Santo Filo (FEEC/UNICAMP) (Presidente)
Prof. Dr. Renato Machado (ITA)
Dr. João Roberto Moreira Neto (EMBRAER)
Prof. Dr. Paulo Cardieri (FEEC/UNICAMP)
Prof. Dr. Hugo Enrique Hernández Figueroa (FEEC/UNICAMP)

A ata de defesa, com as respectivas assinaturas dos membros da Comissão Julgadora, encontra-se no SIGA (Sistema de Fluxo de Dissertação/Tese) e na Secretaria de Pós-Graduação da Faculdade de Engenharia Elétrica e de Computação.

To my parents Fernando and Luisa.

To Gabriela.

Acknowledgements

I thank God for being my strength and guiding my path.

To my parents, Fernando and Luisa, for their unconditional love and support.

To Gabriela, my beloved wife, who always encouraged me to conclude this work. She is the sparkle in my eyes.

I would like to thank Prof. José Cândido and Marco Miranda for the moments of kind dedication and guidance throughout the development of this work. My special thanks to Prof. José Cândido for allowing me to carry out my master's and doctoral studies in Brazil.

I deeply thank my beloved family for being my inspiration and always showing me the right way. I love them so much.

My thanks to my friends and colleagues who accompanied me and helped me during my stay in Brazil. My special thanks to Henry, Nathaly, David, Shirley, Cecilia, Lenin, Rafael, Rony, Diana, and Byron for their invaluable friendship. I wish them always the best.

This study was financed in part by the Coordenação de Aperfeiçoamento de Pessoal de Nível Superior - Brasil (CAPES) - Finance Code 001.

Finally, I would like to thank SENESCYT–Ecuador and Bradar (now Embraer) for the financial support.

"One of the painful things about our time is that
those who feel certainty are stupid, and those
with any imagination and understanding are
filled with doubt and indecision.
Let doubt prevail."
(Bertrand Russell)

Resumo

Esta tese tem como objetivo avançar no campo de sistemas de radar ao lidar com os seguintes problemas centrais: (i) detecção de alvos distribuídos e pontuais imersos em ruído Gaussiano branco complexo; (ii) desempenho de sistemas de radar na presença de *clutter* terrestre do tipo Weibull; e (iii) estimação Doppler para alvos de alta velocidade sob ruído Gaussiano de fundo. A primeira parte da tese (Capítulos 2–4) ataca o primeiro problema, por meio do projeto e da análise de detectores *phased array* ótimos e subótimos para alvos distribuídos e alvos pontuais não-flutuantes. Para cada detector, as estatísticas da variável de decisão são analisadas sob a hipótese de algum – ou mesmo nenhum – conhecimento acerca dos parâmetros do alvo e da potência média do ruído. A partir daí, calculam-se a probabilidade de detecção e a probabilidade de falso alarme. A segunda parte da tese (Capítulos 5 e 6) confronta o segundo problema, fornecendo ferramentas matemáticas eficientes para avaliar o desempenho de um detector *square-law* operando em *clutter* terrestre do tipo Weibull. Aqui, as probabilidades de detecção e falso alarme são obtidas em forma fechada e em representação por séries de convergência rápida. Para isso, faz-se uso da função-H de Fox, bem como de um cálculo abrangente de resíduos. Finalmente, na terceira parte da tese (Capítulo 7), é fornecida uma análise estatística completa da estimação Doppler de alvos com alta velocidade sujeitos a ruído Gaussiano de fundo. A solução apresentada combina duas técnicas de processamento de sinais: o processamento de subpulso e o Teorema Chinês do Resto clássico. Além disso, o desempenho dessa técnica híbrida é avaliado em forma fechada. Vale ressaltar que todas as expressões supracitadas da tese são contribuições originais, com destaque para aquelas obtidas em representações por série, que se mostram atrativas pela ampla economia tanto de tempo de execução quanto de carga computacional.

Palavras-chaves: Detecção ótima, radar *phased array*, alvos não-flutuantes, probabilidade de detecção, probabilidade de falso alarme, teste por razão de verossimilhança generalizada, *clutter* terrestre, processamento de subpulso, Teorema Chinês do resto.

Abstract

This dissertation aims to advance in the field of radar systems by dealing with the following key problems: (i) detection of distributed and point-like targets embedded in complex white Gaussian noise; (ii) radar performance in the presence of Weibull-distributed ground clutter; and (iii) doppler estimation for high-velocity targets in background Gaussian noise. The first part of this dissertation (Chapters 2–4) addresses the first problem by designing and analyzing optimal and suboptimal phased-array detectors for distributed and non-fluctuating point-like targets. For each detector, the decision-variable statistics are investigated assuming a certain or no knowledge about the parameters of the target echoes and the average noise power. In each case, the probability of detection and the probability of false alarm are derived. The second part of this dissertation (Chapters 5 and 6) addresses the second problem by providing efficient mathematical tools to evaluate the performance of a square-law detector operating in Weibull-distributed ground clutter. In this case, the probabilities of detection and false alarm are expressed in terms of both closed-form expressions and fast convergent series. To do so, we rely upon the Fox H-function as well as a comprehensive calculus of residues. Finally, in the third part of this dissertation (Chapter 7), we provide a thorough statistical analysis for the Doppler estimation of high-speed targets in background Gaussian noise. The proposed solution combines two signal processing techniques: subpulse processing and the classic Chinese Remainder Theorem. Also, the performance of this hybrid technique is assessed in closed form. It is worth mentioning that all the aforementioned expressions from this dissertation are original contributions, with emphasis on those obtained in terms of series representations, which proved attractive for large savings in both execution time and computational load.

Keywords: Optimum detection, phased-array radar, non-fluctuating targets, probability of detection, probability of false alarm, generalized likelihood ratio test, ground clutter, subpulse processing, Chinese Remainder Theorem.

List of Figures

List of Tables

List of Acronyms

CA-CFAR	cell-averaging constant false-alarm rate
CCRT	classic Chinese Remainder Theorem
CDF	cumulative distribution function
CFAR	constant false-alarm rate
CPI	coherent processing interval
CRT	Chinese Remainder Theorem
CUT	cell under test
CCS	central chi-squared
CWGN	complex white Gaussian noise
DFT	discrete Fourier transform
GCD	greatest common divisor
GLRT	generalized likelihood ratio test
GO-CFAR	greatest of constant false-alarm rate
LCM	least common multiple
LRT	likelihood ratio test
MLE	maximum-likelihood estimate
NCCS	noncentral chi-squared
NP	Neyman-Pearson
OS-CFAR	order statistics, constant false-alarm rate
PMF	probability mass function
PD	probability of detection
PDF	probability density function
PFA	probability of false alarm
PRF	pulse repetition frequency
PRI	pulse repetition interval
ROC	receiver's operating characteristic
RCRT	robust Chinese Remainder Theorem
RV	random variable
SNR	signal-to-noise ratio
SCR	signal-to-clutter ratio
SO-CFAR	small of constant false-alarm rate
SP	subpulse processing

List of Symbols

$\Gamma(\cdot)$	gamma function
$\Gamma(\cdot,\cdot)$	upper incomplete gamma function
$\Gamma(\cdot,\cdot,\cdot)$	generalized incomplete gamma function
$f_Z(\cdot)$	probability density function of a generic random variable Z
$F_Z(\cdot)$	cumulative distribution function of a generic random
$\Pr[\cdot]$	probability of an event
$\mathbb{E}[\cdot]$	expectation
$\mathbb{VAR}[\cdot]$	variance
$\mathbb{COV}[\cdot]$	covariance
$\det(\cdot)$	determinant
$\max\{\cdot\}$	maximum function
$\min\{\cdot\}$	minimum function
${}_1F_1(\cdot;\cdot;\cdot)$	Kummer confluent hypergeometric function
$B(\cdot,\cdot)$	beta function
$B_{(\cdot)}(\cdot,\cdot)$	incomplete beta function
$G_{m,n}^{p,q}[\cdot]$	Meijer G-function
$\arg\max\{\cdot\}$	argument of the maximum
$\mathrm{Res}[\cdot]$	residue operation
$\lvert\cdot\rvert$	absolute value
$\lfloor\cdot\rfloor$	floor operation
$\mathrm{round}(\cdot)$	rounding operation
$\mathrm{LCM}(\cdot)$	least common multiple operation
$\mathbf{Re}[\cdot]$	real argument
$\mathbf{Im}[\cdot]$	imaginary argument
$\lVert\cdot\rVert$	Euclidean norm
${}_2F_1(\cdot,\cdot;\cdot;\cdot)$	Gauss hypergeometric function
f_d	Doppler frequency
$(a)\mathrm{mod}(b)$	remainder of the euclidean division of a by b
$\mathscr{F}\{\cdot\}$	Fourier transform
${}_2\tilde{F}_1(a,b;c;x)$	regularized Gauss hypergeometric function
$I_0(\cdot)$	modified Bessel function of the first kind and order zero

List of Publications

Journal Articles

- F. D. A. García, A. C. F. Rodriguez, G. Fraidenraich, and J. C. S. Santos Filho, "CA-CFAR detection performance in homogeneous Weibull clutter," *IEEE Geosci. Remote Sens. Lett.*, vol. 16, no. 6, pp. 887-891, Jun. 2019. DOI:10.1109/LGRS.2018.2885451.

- F. D. A. García, H. R. C. Mora, G. Fraidenraich and J. C. S. Santos Filho, "Square-law detection of exponential targets in Weibull-distributed ground clutter," to appear in *IEEE Geosci. Remote Sens. Lett.*, 2021. DOI:10.1109/LGRS.2020.3009304.

- F. D. A. García, H. R. C. Mora, N. V. O. Garzón, and J. C. S. Santos Filho, "Alternative representations for the probability of detection of non-fluctuating targets," *IET Electron. Lett.*, vol. 56, no. 21, pp. 1136-1139, Oct. 2020. DOI:10.1049/el.2020.1810.

- F. D. A. García, M. A. M. Miranda and J. C. S. Santos Filho, "New findings on GLRT radar detection of nonfluctuating targets via phased arrays," *IEEE Access*, under review, 2021.

- F. D. A. García, A. S. Guerreiro, G. R. de Lima Tejerina, J. C. S. Santos Filho, G. Fraidenraich, and M. D. Yacoub, "Doppler estimation for high-velocity targets using subpulse processing and the Chinese Remainder Theorem," *IEEE Trans. Signal Process.*, under review, 2021.

Conference Articles

- F. D. A. García, M. A. M. Miranda and J. C. S. Santos Filho, "Optimum detection for a class of stationary meteorological radars," in *Proc. 26th European Signal Processing Conference (EUSIPCO)*, pp. 2258-2262, Italy, Rome, Sept. 2018. DOI:10.23919/EUSIPCO.2018.8553329.

- F. D. A. García, A. S. Guerreiro, G. R. de Lima Tejerina, J. C. S. Santos Filho, G. Fraidenraich, M. D. Yacoub, M. A. M. Miranda, and H. Cioqueta, "Probability of Detection for unambiguous doppler frequencies in pulsed radars using the Chinese

Remainder Theorem and Subpulse Processing," in *Proc. 53th IEEE Asilomar Conference on Signals, Systems, and Computers*, pp. 138-142, Pacific Grove, CA, USA, Nov. 2019. DOI:10.1109/IEEECONF44664.2019.9048664.

Co-Authored Journal Articles

- N. V. O. Garzón, H. R. C. Mora, E. B. Aragón, F. D. A. García, and C. D. Altamirano, "On the bit error probability and the spectral efficiency of opportunistic wireless transmissions in Rician fading channels," *ELSEVIER: Physical Communication*, under review, 2021.

Co-Authored Conference Articles

- R. A. C. Flores, F. D. A. García, G. R. de Lima Tejerina, G. Fraidenraich, J. C. S. Santos Filho, M. D. Yacoub, M. A. M. Miranda, A. Bertetich, and J. R. Moreira Neto, "Radar coverage over irregular terrain: A practical algorithm for multipath propagation," in *Proc. 2018 IEEE Radar Conference (RadarConf18)*, Oklahoma, USA, 2018, pp. 1383-1388. DOI: 10.1109/RADAR.2018.8378766.
- H. R. C. Mora, N. V. O Garzón, F. D. A. García, and C. de Almeida, "On the Bit Error Rate of OFDMA Employing Short Cyclic Prefix and Maximal Ratio Combining," in *Proc. 2019 IEEE Colombian Conference on Communications and Computing (COLCOM)*, Barranquilla, Colombia, 2019, pp. 1-6. DOI: 10.1109/ColComCon.2019.8809120.

Contents

1 Introduction

This dissertation comprises an assortment of somewhat independent contributions to the field of modern radar systems. Before setting into them, we briefly review two required mathematical tools and some essential theoretical background on radar signal processing.

1.1 Preliminaries

In this section, we shortly describe the multivariate Fox H-function and the Residue Theorem as those tools will be extensively used in the next chapters.

1.1.1 The Multivariate Fox H-function

The Fox H-function has been used in a wide variety of recent applications, including mobile communications and radar systems (cf. [1, 2, 3, 4, 5] for a detailed discussion on this). In [6], the authors considered the most general case of the Fox H-function for multiple variables, defined as

$$\mathbf{H}\left[\mathbf{x};\left(\delta,\mathbf{D}\right);\left(\beta,\mathbf{B}\right);\mathcal{L}_{S}\right]\triangleq\left(\frac{1}{2\pi j}\right)^{N}\oint_{\mathcal{L}_{\mathbf{s}}}\Theta\left(\mathbf{s}\right)\mathbf{x}^{-\mathbf{s}}\mathrm{d}\mathbf{s},\tag{1.1}$$

in which $j=\sqrt{-1}$ is the imaginary unit, $\mathbf{s}\triangleq[s_1,\cdots,s_N]$, $\mathbf{x}\triangleq[x_1,\cdots,x_N]$, $\beta\triangleq[\beta_1,\cdots,\beta_N]$, and $\delta\triangleq[\delta_1,\cdots,\delta_N]$ denote vectors of complex numbers, and $\mathbf{B}\triangleq\left(b_{i,j}\right)_{n\times N}$ and $\mathbf{D}\triangleq\left(d_{i,j}\right)_{m\times N}$ are matrices of real numbers. Also, $\mathbf{x}^{-\mathbf{s}}\triangleq\prod_{i=1}^{N}x_i^{-s_i}$, $\mathrm{d}\mathbf{s}\triangleq\prod_{i=1}^{N}\mathrm{d}s_i$, $\mathcal{L}_{\mathbf{s}}\triangleq\mathcal{L}_{\mathbf{s},1}\times\cdots\times\mathcal{L}_{\mathbf{s},N}$, $\mathcal{L}_{\mathbf{s},k}$ is an appropriate contour on the complex s_k plane, and

$$\Theta\left(\mathbf{s}\right)\triangleq\frac{\prod_{i=1}^{m}\Gamma\left(\delta_i+\sum_{k=1}^{N}d_{i,k}s_k\right)}{\prod_{i=1}^{n}\Gamma\left(\beta_i+\sum_{k=1}^{N}b_{i,k}s_k\right)},\tag{1.2}$$

in which $\Gamma(\cdot)$ is the gamma function [7, Eq. (6.1.1)].

1.1.2 The Residue Theorem

Let $f\left(z\right)$ be an analytic complex function defined on and inside a simple closed path C on the complex plane, except for finitely many singular points $z_1,z_2,\ldots,z_k$ inside C. Then, the integral of $f\left(z\right)$ taken counterclockwise around C equals $2\pi j$ times the sum of residues of $f\left(z\right)$ at $z_1,z_2,\ldots,z_k$. That is [8],

$$\oint_{C}f\left(z\right)\mathrm{d}z=2\pi j\sum_{i=1}^{k}\mathrm{Res}\left[f\left(z\right);z=z_i\right],\tag{1.3}$$

where $\mathrm{Res}\left[f\left(z\right);z=z_i\right]$ represents the residue of $f\left(z\right)$ evaluated at the poles z_i $(i=1,2,\ldots,k)$. The residue of $f\left(z\right)$ at an mth-order pole at z_0 is defined as [8, Eq. (16.3.5)]

$$\mathrm{Res}\left[f\left(z\right);z=z_0\right]\triangleq\frac{1}{(m-1)!}\lim_{z\to z_0}\left[\frac{d^{m-1}}{dz^{m-1}}\left(\left(z-z_0\right)^m f\left(z\right)\right)\right]. \tag{1.4}$$

1.2 Theoretical Background

In this section, we revisit important concepts that will be used throughout this dissertation.

1.2.1 Radar Cross Section

The target's radar cross section (RCS) plays an essential role in radar detection. It determines the amount of energy reflected by a target, directly affecting the power of the target echoes received by the radar. RCS depends on various system parameters: target's geometry and composition; transmitter's position relative to the target; receiver's position relative to target; operational frequency; transmitter's polarization; and receiver's polarization [9]. Since the target's RCS is extremely sensitive to those parameters, it is common and more effective to describe its behaviour on a statistical basis [10]. This argument leads to considering the target's RCS as a random variable (RV) with a suitable probability density function (PDF). It is important to emphasize that, in reality, the RCS is not random. If it was possible to describe the target's surface shape, materials, and location in enough detail, then its RCS could in principle be calculated accurately using deterministic methods [11]. However, in practice, the RCS databases are obtained for industrial applications and military purposes and are not available for the civil scientific community.

1.2.2 Distributed and Point-like Targets

A distributed target (also called extended target or volume target) is an object whose physical extent occupies several resolution cells (e.g., ships, tanks, precipitation, and clouds) [10]. This type of target is characterized by several particles occupying the same resolution volume,[1] the echoes of which overlap in the resulting back-propagation signal. Distributed targets are commonly used to represent meteorological phenomena, in which the phase and amplitude characteristics are considered to follow a statistical distribution [12]. Occasionally distributed targets are composed of several particles moving at different speeds. In that case, their frequency spectrum exhibits a certain dispersion. This

[1] A resolution volume is the smallest three-dimensional region (range, azimuth, and elevation) in which the radar can still distinguish multiple targets [10].

behavior is a direct consequence of turbulence and variations in the movement of particles within the meteorological phenomena. Such behavior imposes serious complications in the processing of this type of signal [13].

On the other hand, a point-like target is defined as an object with small spatial extent, confined within a single resolution cell [10]. As in the case of distributed targets, the amplitude and phase characteristics are also governed by statistical distributions. The random variations of the received target echo can be characterized by the widely used Swerling models [14]. In essence, these models intend to address the common problem of making a detection decision based on a block of echo samples from a given resolution cell [9]. Specifically, the Swerling models (labeled from 0 to IV) seek to characterize the RCS of point-like targets. The exponential and fourth-degree chi-squared distributions are used. The exponential distribution arises when there is a large number of individual scatterers randomly distributed in space and each with approximately the same individual RCS. This distribution is used in the Sweling cases I and II [14, 15, 16]. In case there is a large number of individual scatterers, one being dominant and the rest having the same RCS, the exponential distribution is no longer a good fit. The noncentral chi-squared distribution with two degrees of freedom gives the exact PDF for this case, but this PDF is considered somewhat difficult to work with because its expression contains a Bessel function. Instead, the fourth-degree chi-squared distribution is used in the Swerling cases III and IV, since it is an analytically more tractable approximation [15, 17]. The case where the target's RCS exhibits no random behavior is called Swerling 0 [10].

1.2.3 Optimal and Suboptimal Detectors

Before the radar performs any task (e.g., searching, tracking, or imaging), the system must decide whether a target of interest is present or absent in a certain angle, range, or Doppler bin [9]. Unfortunately, the presence of unwanted signals such as thermal noise, clutter, and jamming, ubiquitous in practice, often renders this decision more complicated. The optimal decision is achieved by applying the *likelihood ratio test* (LRT) [18]. This decision is based on the Neyman-Pearson (NP) criterion, which maximizes the probability of detection (PD) for any given probability of false alarm (PFA) [19]. But the LRT provides an optimal decision only if the probability density functions of the received samples are fully known, and this requirement does not fit most practical problems. In view of this, a more general decision rule is commonly used to deal with these types of scenarios: the so-called *generalized likelihood ratio test* (GLRT) [20]. In the GLRT, all unknown PDF parameters are replaced by their maximum likelihood estimates (MLEs). This structure allows the GLRT to work over a wide range of scenarios. Although there is no optimality associated with the GLRT, it turns out to work quite well, in practice.

1.2.4 Detection in Weibull-Distributed Ground Clutter

Different types of interference signals, such as thermal noise, clutter, and jamming can hinder the detection process of a radar system [9]. Clutter is a radar return from one or more objects of no interest to the radar mission. For example, the mission of many radar systems is the detection and tracking of aircraft, ships, or ground vehicles. To these systems, the clutter may be an interfering return from a natural object such as precipitation, vegetation, soil, rocks, or the sea. However, to radars designed for remote sensing such as synthetic aperture radar (SAR) imagers, those natural objects may be the primary targets of interest [21]. Throughout this dissertation but Chapter 2, we assume that the targets of interest are man-made, while natural target returns are unwanted (i.e., clutter).

The clutter statistics can be similar to those of noise when the natural targets are composed of small, nearly equal-sized scatterers but can be quite different when the nature of the scatterers change or when scatterers of different types (e.g., a tree line) are present in the radar's field of view. For these cases, amplitude distributions having much longer tails than the Rayleigh distribution (used to model thermal noise) have been observed. More importantly, although the noise is independent of transmission frequency, spatial position, and environmental parameters, the clutter varies with all of these parameters, making its characterization very complex [22]. The clutter can be classified in two main categories: surface clutter and volume clutter. The surface clutter includes trees, vegetation, ground terrain, man-made structures, and sea surface (sea clutter). The volume clutter normally has large extent (size) and includes chaff, precipitation, clouds, birds, and insects [23]. In particular, the radar performance can be significantly degraded in the presence of ground clutter. Through experimental data, it has been observed that the ground-clutter statistics are well modeled by the Weibull distribution [24, 25]. As a result, this distribution has been widely used to assess the radar performance in the presence of ground clutter. In this dissertation, we focus on Weibull-distributed ground clutter.

1.2.5 CFAR Detection

As mentioned earlier, the radar detection is strongly affected by unwanted interference signals like thermal noise, clutter, and jamming. To overcome this problem, modern radar systems employ dedicated constant false-alarm rate (CFAR) detectors. These detectors have the property of maintaining a constant false-alarm rate in the presence of strong interference. In essence, a CFAR detector dinamically sets the detection threshold above the interference level. This is carried out by continuously estimating the interference power over a data window [26, 23]. The CFAR architecture is illustrated in

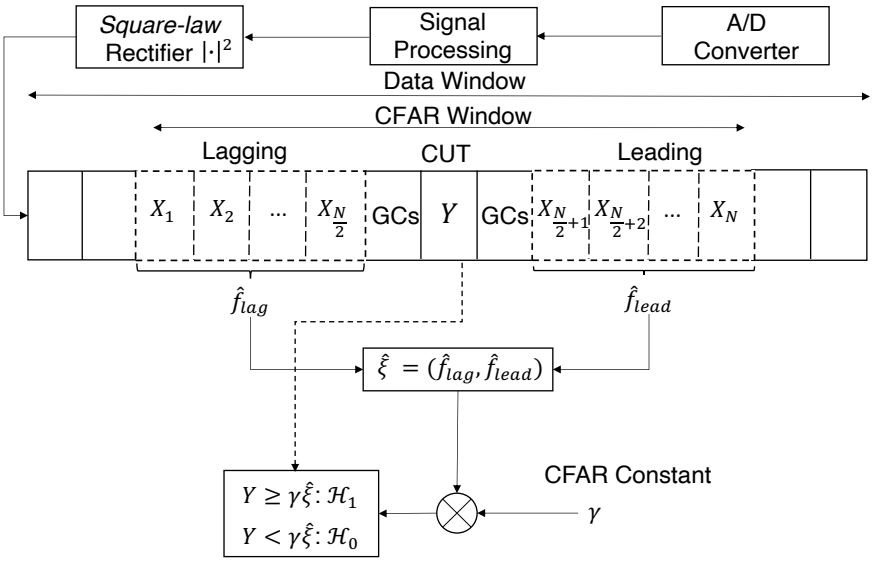

Figure 1.1 – The CFAR architecture.

Fig. 1.1, and the detection algorithm runs as follows. First, the samples at the output of the rectifier are stored in a computer memory as a one-dimensional (1-D) vector, also called data window, composed of several thousand range cells. The CFAR window resides within the data window and is composed of leading and lagging reference windows, guard cells (GCs), and the cell under test (CUT) [9], as shown in Fig. 1.1. The number of cells within the CFAR window depends strongly on the range resolution of the radar. Secondly, the unknown interference power, ξ, is estimated by applying a specific function, $\hat{\xi} = (\hat{f}_{lag}, \hat{f}_{lead})$, given in terms of the data contained in the leading and lagging windows. This function is chosen based on the type of effect that must be mitigated. At last, a detection decision on whether a target is present or absent, is carried out by comparing the sample value within the CUT, Y, with a combined threshold, say, $\gamma\hat{\xi}$, where γ is the CFAR constant [9]. If Y exceeds the threshold, then the system decides for "target present"; otherwise, the system decides for "target absent". Among a wide variety of existing CFAR detectors, we highlight the following:

- Cell-averaging constant false-alarm rate (CA-CFAR): The CA-CFAR detector raises the detection threshold above the interference power. This detector is relatively simple in that it computes the detection threshold by averaging the interference power in the reference window [25].

- Greatest-of cell-averaging constant false-alarm rate (GOCA-CFAR): The GOCA-CFAR detector was conceived to reduce clutter-edge false alarms. These false alarms are suppressed by computing the average interference power in the lagging and leading windows separately and selecting the largest sample mean as the CFAR

statistic [27].

- Smallest-of cell-averaging constant false-alarme rate (SOCA-CFAR): The SOCA-CFAR detector estimates the interference power in the lagging and leading reference windows and selects the smallest estimate as the CFAR statistic. In so doing, this detector can suppress interfering targets that may reside in the either leading or lagging window but not targets in both windows [9].

1.2.6 Doppler Estimation

Suppose that a target is approaching the radar with a radial velocity v and the radar transmits a series of M pulses separated by a pulse repetition interval (PRI) of T seconds. The range to the target when the m-th pulse ($1 \leq m \leq M$) is transmitted is $R_0 - mvT$ meters, with R_0 being the initial range. Then, the phase shift of the m-th pulse will be $(-4\pi/\lambda)(R_0 - mvT)$ radians [10]. Accordingly, when the radar samples (at $t = 2R_0 + mT$) the signals collected during a coherent processing interval (CPI), the measured output for the m-th pulse will be [9]

$$\begin{aligned} y[m] =& A \exp\left[j\left(\theta_0 - \left(\frac{4\pi}{\lambda}\right)(R_0 - vmT)\right)\right] \\ =& A \exp\left[j\left(2\pi\left(\frac{2v}{\lambda}\right)(mT) + \underbrace{\theta_0 - \left(\frac{4\pi R_0}{\lambda}\right)}_{\theta'}\right)\right] \\ =& A \exp\left[j\left(2\pi f_d mT + \theta'\right)\right], \end{aligned} \tag{1.5}$$

where $j = \sqrt{-1}$ is the imaginary unit, A is the received amplitude, θ_0 is the initial phase, and f_d is the Doppler frequency shift. The shift will be positive for closing targets and negative for receding targets. The sinusoid in (1.5) is the result of the changing echo phases, which in turn are caused by the changes in the target range between pulses [9]. Since the discrete Fourier transform (DFT) provides the mechanism to test multiple candidate frequencies, it is then applied over the $y[m]$ samples so as to capture the target's Doppler shift.

1.2.7 Chinese Remainder Theorem

Measurements made with a pulse waveform can be ambiguous in range, Doppler, or both. Pulsed radars frequently operate in scenarios that are ambiguous in one or both of the range and Doppler dimensions. Fortunately, there are some techniques that can resolve such ambiguities, although at the cost of extra measurement time and processing load. These techniques make use of multiple pulse repetition frequencies (PRFs) [28, 29, 30].

Among them, the most known and used technique is the classic Chinese Remainder Theorem (CCRT). It is a fast and accurate method to resolve range and Doppler ambiguities [31, 32]. Next, we briefly explain its operation.

For now, let us consider only range ambiguity. Once the PRF is selected, it establishes an unambiguous range $R_{ua} = c/2\text{PRF} = c\text{PRI}/2$. A target at an actual range $R_t > R_{ua}$ will be detected at an apparent range R_a that satisfies [9]

$$R_t = R_a + kR_{ua} \tag{1.6}$$

for some integer k. That is, when the radar detects a target at an apparent range R_a, the actual range could be R_a plus any multiple of R_{ua}. It is convenient to express the apparent, true, and unambiguous ranges in terms of their corresponding range bins. For example, $n_a \triangleq R_a/\Delta R$, where ΔR is the range bin spacing. Dividing both parts by ΔR, Eq. (1.6) then becomes

$$n_t = n_a + kN, \tag{1.7}$$

where N the total number of range bins. The basic approach to resolving range ambiguities relies on multiple PRFs. Suppose there are N_i ($i \in \{1, 2, \ldots, I\}$, with I being the number of PRFs) range bins in the unambiguous range interval on PRF i. Then, we have that $R_{ua,i} = N_i \Delta R_i$. Note that the unambiguous range is different for each PRF. Therefore, assuming that the range bin spacing is the same for each PRF used, the true range bin must satisfy Eq. (1.7) for each of the PRFs used:

$$n_t = n_{a_1} + k_1 N_1 = n_{a_2} + k_2 N_2 = \ldots = n_{a_I} + k_I N_I. \tag{1.8}$$

The CCRT solves the above set of congruences by using the estimated measurements $n_{a_1}, n_{a_2}, \ldots, n_{a_I}$ of each PRF [33, 34, 35]. It is worth noting that the major disadvantage of the CCRT is that the use of multiple PRFs consumes a large amount of the radar timeline. Additionally, if the number of targets to be detected exceeds the number of PRFs, then *ghosts* may appear.[2]

1.3 Summary of Contributions and Dissertation Outline

This dissertation comprises most of our research results in the field of radar systems across the following topics: (i) detection of distributed and point-like targets embedded in complex white Gaussian Noise (CWGN); (ii) radar performance in the presence of Weibull-distributed ground clutter; (iii) Doppler estimation for high-velocity targets in

[2] *Ghosts* are false targets resulting from false coincidences of Doppler- or range-ambiguous data [1].

background Gaussian noise. The dissertation is presented as a compilation of papers published in technical journals and conference proceedings, as well as papers currently under review. The contents presented here are copies of our published or submitted materials. The corresponding permission grants to reproduce the published papers are attached in Appendix A. The remainder of the dissertation is structured in three main parts as follows.

Part I: Optimal and suboptimal phased-array detectors for distributed and non-fluctuating point-like targets

Chapter 2. This chapter, named Contribution I, is a replica of our paper entitled "Optimum detection for a class of stationary meteorological radars", published in the Proceedings of the 26th European Signal Processing Conference (EUSIPCO 2018) [36]. That work is an extension of [37, 38], in which the authors proposed an optimum detector for meteorological phenomena by exploiting the correlation between the received signals from two fixed wide-beam antennas. In those works, it was observed that an extremely large amount of signal samples would be required to render the radar performance acceptable, and that such a problem could be alleviated by increasing the number of antennas. The chapter is a first step in this direction, extending the original radar proposal from two to an arbitrary number of antennas. In addition to designing an optimum detector for the new radar, we assess its performance by deriving asymptotic, closed-form expressions for the resulting detection and false-alarm probabilities. As a term of comparison, we also design and analyze a suboptimal detection scheme based on the traditional phased-array approach. All our derivations are validated via Monte-Carlo simulations.

Chapter 3. This chapter, named Contribution II, is a replica of our paper entitled "Alternative representations for the probability of detection of non-fluctuating targets," published in the IET Electronic Letters [5]. In that work, we address the phased-array detection problem of weak signals in background noise. More specifically, we consider a non-fluctuating target embedded in CWGN, with both the target amplitude and the noise power being unknown. Scanning the open technical literature, we realized that no closed-form solutions nor analytically tractable approximations for the associated PD were available. This is mainly because the computation of the PD requires evaluating a cumbersome PDF for the target-plus-noise scenario [39, 40]. In the chapter, we derive an exact closed-form expression and a fast convergent series representation for the aforementioned PD. To do so, we rely on the bivariate Fox H-function and a comprehensive calculus of residues. In particular, the series representation proves efficient and computationally attractive, achieving a high accuracy even for a small number of terms, while showing a remarkable reduction in both the computational load and the computation time as compared to the numerical evaluation of the existing integral-form solution.

Chapter 4. This chapter, named Contribution III, is a replica of our paper entitled "New findings on GLRT radar detection of non-fluctuating targets via phased arrays," currently under review in the IEEE Access. In that work, we design and analyze a new GLRT-based detector which takes place after the analog beamforming operation. For the analysis, we consider a *non-fluctuating* target embedded in CWGN, with the amplitude of the target echo and the noise power being assumed unknown. Distinguished works have analyzed the performance for the referred scenario and proposed GLRT-based detectors [40, 41, 42, 43]. But those detectors appear at an early stage (i.e., prior to the formation of any beamforming waveform), thereby imposing high demands on hardware, processing, and data storage. From a hardware perspective, most radar systems fail to meet such strong requirements. In fact, due to hardware and computational constraints, most radars use a combination of analog and digital beamformers (sums) before any estimation or further pre-processing. Our main motivation in the chapter is to derive a GLRT detector that meets acceptable hardware and system requirements and, in turn, delivers accurate decisions. To this end, we design and analyze a more practical and easy-to-implement GLRT detector after the analog beamforming operation. The performance of the proposed detector is analyzed and the PD and PFA are derived in closed form. An alternative fast convergent series for the PD is also derived. This series proves to be very efficient and computationally tractable, saving both computation time and computational load. Remarkably, we show that in the low signal-to-noise ratio (SNR) regime, our proposed post-beamforming GLRT detector outperforms the classic pre-beamforming GLRT detector (and the workhorse square-law detector). This finding suggests that when the signals are weak, we had better reinforce (add) them before applying the GLRT decision framework. It is also shown that the PFA of the proposed post-beamforming GLRT detector is independent of the number of antennas, which allows us to adjust the PD while maintaining a fixed PFA.

Part II: Square-law detection over Weibull-distributed ground clutter

Chapter 5. This chapter, named Contribution IV, is a replica of our paper entitled "CA-CFAR detection performance in homogeneous Weibull clutter," published in the IEEE Geoscience and Remote Sensing Letters [1]. That work presents a novel, highly accurate approximation for the PD of a CA-CFAR radar system operating in an homogeneous Weibull-clutter environment. More importantly, we consider a realistic scenario with both target returns and clutter residues within the CUT. Due to the mathematical complexity surrounding this type of scenario, no performance analysis had been carried out in the literature to date. The contributions of the chapter are two-fold: first, we de-

rive novel closed-form expressions for the PDF and the cumulative distribution function (CDF) of the sum of an exponentially fluctuating target embedded in Weibull clutter; and then, we obtain a closed-form expression for the corresponding PD. All derived closed-form expressions are given in terms of the bivariate Fox H-function, for which we provide a portable and efficient MATHEMATICA's routine. In addition, we provide alternative and easily computable series representations. The validity of all expressions is confirmed via Monte-Carlo simulations. Our results are compared with the idealized Neyman-Pearson detector so as to quantify the CFAR losses, indicating that even a small change in the shape parameter of the clutter distribution can significantly affect the radar detection performance.

Chapter 6. This chapter, named Contribution V, is a replica of our paper entitled "Square-law detection of exponential targets in Weibull-distributed ground clutter," to appear in the IEEE Geoscience and Remote Sensing Letters [44]. In that work, we focus on the PD of a square-law detector in the presence of exponential targets and Weibull-distributed ground clutter. To the best of our knowledge, no radar performance analysis has been published so far using the exact statistics of a square-law detector when subject to exponential targets and Weibull clutter interference. In the chapter, we derive a closed-form solution and a fast convergent series for the aforementioned PD. The closed-form solution is given in terms of the Fox H-function, whereas the series representation is obtained by exploiting the orthogonal selection of poles in Cauchy's residue theorem. In passing, we also obtain closed-form solutions and series representations for the PDF and CDF of the sum statistics that govern the output of a square-law detector.

Part III: Doppler estimation of high-speed targets in background Gaussian noise

Chapter 7. This chapter, named Contribution IV, is a replica of our paper entitled "Doppler estimation for high-velocity targets using subpulse processing and the Chinese Remainder Theorem," currently under review in the IEEE Transactions on Signal Processing. A preliminary version of these results were published in the Proceedings of the IEEE 53th Asilomar Conference on Signals, Systems, and Computers [35]. That work addresses the problem of estimating the velocity of fast-moving targets. In pulsed Doppler radars, the Chinese Remainder Theorem (CRT) is a common method to resolve Doppler ambiguities caused by fast-moving targets [28, 29, 30, 32, 33]. Another issue concerning high-velocity targets is related to SNR losses after performing *range compression*. This loss can be partially mitigated by the use of subpulse processing (SP) [45, 46]. Modern radars combine the CRT and SP in order to reliably unfold the target velocity. However, both techniques have hardware and physical limitations when it comes to estimating high target

velocities. Besides, the performance of such techniques may be degraded in the presence of background Gaussian noise. In the chapter, we provide a comprehensive statistical analysis of Doppler estimation. More precisely, we derive closed-form expressions for the PD and PFA when both the CRT and SP are used. A comparison between SP and the classic pulse processing (PP) technique is also carried out. Numerical results and Monte-Carlo simulations corroborate the validity of our expressions and show that the SP–plus–CCRT technique can greatly reduce the PFA compared to previous studies.

1.4 Bibliography

[1] F. D. G. Almeida, A. C. F. Rodriguez, G. Fraidenraich, and J. C. S. S. Filho, "CA-CFAR detection performance in homogeneous Weibull clutter," *IEEE Geosci. Remote Sens. Lett.*, vol. 16, no. 6, pp. 887–891, Jun. 2019.

[2] Y. Abo Rahama, M. H. Ismail, and M. S. Hassan, "On the sum of independent Fox's H -function variates with applications," *IEEE Trans. Veh. Technol.*, vol. 67, no. 8, pp. 6752–6760, Aug. 2018.

[3] C. R. N. da Silva, E. J. Leonardo, and M. D. Yacoub, "Product of two envelopes taken from $\alpha-\mu$, $\kappa-\mu$ and $\eta-\mu$ distributions," *IEEE Trans. Commun.*, vol. PP, no. 99, pp. 1–1, Mar. 2017.

[4] C. H. M. de Lima, H. Alves, and P. H. J. Nardelli, "Fox H-function: A study case on variate modeling of dual-hop relay over Weibull fading channels," in *2018 IEEE Wireless Communications and Networking Conference (WCNC)*, Apr. 2018, pp. 1–5.

[5] F. D. A. García, H. R. C. Mora, G. Fraidenraich, and J. C. S. S. Filho, "Alternative representations for the probability of detection of non-fluctuating targets," *Electron. Lett.*, vol. 56, no. 21, pp. 1136–1139, Oct. 2020.

[6] N. T. Hai and H. M. Srivastava, "The convergence problem of certain multiple Mellin-Barnes contour integrals representing H-functions in several variables," *Computers & Mathematics with Applications*, vol. 29, no. 6, pp. 17–25, 1995.

[7] M. Abramowitz and I. A. Stegun, *Handbook of Mathematical Functions with Formulas, Graphs, and Mathematical Tables*, 10th ed. Washington, DC: US Dept. of Commerce: National Bureau of Standards, 1972.

[8] E. Kreyszig, *Advanced Engineering Mathematics*, 10th ed. New Jersey, NJ, USA: John Wiley & Sons, 2010.

[9] M. A. Richards, J. Scheer, W. A. Holm, and W. L. Melvin, *Principles of Modern Radar: Basic Principles*, 1st ed. West Perth, WA, Australia: SciTech, 2010.

[10] M. A. Richards, *Fundamentals of Radar Signal Processing*, 2nd ed. Ney York, NY, USA: McGraw-Hill, 2014.

[11] W. A. Skiliman, "Comments on "On the derivation and numerical evaluation of the Weibull-Rician distribution"," *IEEE Trans. Aerosp. Electron. Syst.*, vol. AES-21, no. 3, pp. 427–429, May 1985.

[12] H. Sauvageot, *Radar Meteorology*. Massachusetts, MA, USA: Artech House, 1992.

[13] L. V. Blake, *Radar Range-performance Analysis*, 1st ed. Norwood, MA, USA: Artech House, 1986.

[14] P. Swerling, "Probability of detection for fluctuating targets," *IRE Transactions on Information Theory*, vol. IT-6, pp. 269–308, Apr. 1960.

[15] D. A. Shnidman, "Radar detection probabilities and their calculation," *IEEE Trans. Aerosp. Electron. Syst.*, vol. 31, no. 3, pp. 928–950, Jul. 1995.

[16] ——, "Expanded swerling target models," *IEEE Trans. Aerosp. Electron. Syst.*, vol. 39, no. 3, pp. 1059–1069, Jul. 2003.

[17] H. Lim and D. Yoon, "Refinements of binary integration for Swerling target fluctuations," *IEEE Trans. Aerosp. Electron. Syst.*, vol. 55, no. 2, pp. 1032–1036, July 2019.

[18] H. Chernoff, "On the distribution of likelihood ratio," *Ann. Math. Statist.*, vol. 25, no. 3, pp. 573–578, Sept. 1954.

[19] A. Leon-Garcia, *Probability and Random Processes for Electrical Engineering*, 3rd ed. New Jersey, NJ, USA: Pearson Prentice Hall, 1994.

[20] S. M. Kay, *Fundamentals of Statistical Signal Processing: Estimation Theory*, 1st ed. New Jersey, NJ, USA: Prentice Hall PTR, 1993.

[21] S. Huber, M. Younis, A. Patyuchenko, G. Krieger, and A. Moreira, "Spaceborne reflector SAR systems with digital beamforming," *IEEE Trans. Aerosp. Electron. Syst.*, vol. 48, no. 4, pp. 3473–3493, Oct. 2012.

[22] M. I. Skolnik, *Introduction to Radar Systems*, 3rd ed. Ney York, NY, USA: McGraw-Hill, 2001.

[23] B. R. Mahafza, *Radar Systems Analysis and Design Using Matlab*, 3rd ed. CRC Press, 2013.

[24] T. Bucciarelli, "CFAR problems in Weibull clutter," *Electron. Lett.*, vol. 21, no. 8, pp. 286–304, Apr. 1985.

[25] M. Sekine, S. Ohtani, T. Musha, T. Irabu, E. Kiuchi, T. Hagisawa, and Y. Tomita, "Weibull-distributed ground clutter," *IEEE Trans. Aerosp. Electron. Syst.*, vol. AES-17, no. 4, pp. 596–598, Jul. 1981.

[26] P. P. Gandhi and S. A. Kassam, "Analysis of CFAR processors in nonhomogeneous background," *IEEE Trans. Aerosp. Electron. Syst.*, vol. 24, no. 4, pp. 427–445, Jul. 1988.

[27] R. Rifkin, "Analysis of CFAR performance in Weibull clutter," *IEEE Trans. Aerosp. Electron. Syst.*, vol. 30, no. 2, pp. 315–329, Apr. 1994.

[28] G. V. Trunk, "Range resolution of targets using automatic detectors," *IEEE Trans. Aerosp. Electron. Syst.*, vol. AES-14, no. 5, pp. 750–755, Sept. 1978.

[29] S. A. Hovanessian, "An algorithm for calculation of range in a multiple PRF radar," *IEEE Trans. Aerosp. Electron. Syst.*, vol. AES-12, no. 2, pp. 287–290, Mar. 1976.

[30] X.-G. Xia and G. Wang, "Phase unwrapping and a robust chinese remainder theorem," *IEEE Signal Process. Lett.*, vol. 14, no. 4, pp. 247–250, Apr. 2007.

[31] V. A. Aalo, "Performance of maximal-ratio diversity systems in a correlated Nakagami-fading environment," *IEEE Trans. Commun.*, vol. 43, no. 8, pp. 2360–2369, 1995.

[32] X. Li, H. Liang, and X. Xia, "A robust chinese remainder theorem with its applications in frequency estimation from undersampled waveforms," *IEEE Trans. Signal Process.*, vol. 57, no. 11, pp. 4314–4322, Nov. 2009.

[33] W. Wang and X. Xia, "A closed-form robust chinese remainder theorem and its performance analysis," *IEEE Trans. Signal Process.*, vol. 58, no. 11, pp. 5655–5666, Nov. 2010.

[34] G. V. Trunk and W. M. Kim, "Ambiguity resolution of multiple targets using pulse-Doppler waveforms," *IEEE Trans. Aerosp. Electron. Syst.*, vol. 30, no. 4, pp. 1130–1137, Oct. 1994.

[35] F. D. A. García, A. S. Guerreiro, G. R. L. Tejerina, J. C. S. Santos Filho, G. Fraidenraich, M. D. Yacoub, M. A. M. Miranda, and H. Cioqueta, "Probability of detection for

unambiguous doppler frequencies in pulsed radars using the chinese remainder theorem and subpulse processing," in *Proc. 53rd Asilomar Conference on Signals, Systems, and Computers*, Pacific Grove, CA, USA, Nov. 2019, pp. 138–142.

[36] F. D. A. García, M. A. M. Miranda, and J. C. S. Santos Filho, "Optimum detection for a class of stationary meteorological radars," in *Proc. 26th European Signal Processing Conference (EUSIPCO)*, Rome, Italy, Sept. 2018, pp. 2258–2262.

[37] M. A. M. Miranda, J. C. S. Santos Filho, G. Fraidenraich, M. D. Yacoub, J. R. Moreira Neto, and Y. C. Zúñiga, "Correlation between signals from spaced antennas of stationary meteorological radars," *IEEE Trans. Geosci. Remote Sens.*, vol. 52, no. 6, pp. 3116–3124, Jun. 2014.

[38] ——, "Radar meteorológico com antenas fixas: Projeto e análise de detector ótimo," in *Proc. XXXI Brazilian Symposium of Telecommunications*, Fortaleza, Brazil, 01-04, Sept. 2013.

[39] W. G. Bulgren, "On representations of the doubly non-central F distribution," *J. Amer. Statist.*, vol. 66, no. 333, pp. 184–186, Mar. 1971.

[40] S. S. Haykin and A. O. Steinhardt, *Adaptive Radar Detection and Estimation*, 1st ed. New Jersey, NJ, USA: J. Wiley, 1992.

[41] E. J. Kelly, "An adaptive detection algorithm," *IEEE Trans. Aerosp. Electron. Syst.*, vol. AES-22, no. 2, pp. 115–127, Mar. 1986.

[42] I. S. Reed, J. D. Mallett, and L. E. Brennan, "Rapid convergence rate in adaptive arrays," *IEEE Trans. Aerosp. Electron. Syst.*, vol. AES-10, no. 6, pp. 853–863, Nov. 1974.

[43] S. Bose and A. O. Steinhardt, "Optimum array detector for a weak signal in unknown noise," *IEEE Trans. Aerosp. Electron. Syst.*, vol. 32, no. 3, pp. 911–922, Jul. 1996.

[44] F. D. A. García, H. R. C. Mora, G. Fraidenraich, and J. C. S. S. Filho, "Square-law detection of exponential targets in Weibull-distributed ground clutter," *IEEE Geosci. Remote Sens. Lett.*, to be published, doi: 10.1109/LGRS.2020.3009304.

[45] G. Beltrao, L. Pralon, M. Menezes, P. Vyplavin, B. Pompeo, and M. Pralon, "Subpulse processing for long range surveillance noise radars," in *Proc. International Conference on Radar Systems (Radar 2017)*, Belfast, UK, Oct. 2017, pp. 1–4.

[46] A. Barreto, L. Pralon, B. Pompeo, G. Beltrao, and M. Pralon, "FPGA design and implementation of a real-time subpulse processing architecture for noise radars," in

Proc. 2019 International Radar Conference (RADAR), Toulon, France, Sept. 2019, pp. 1–6.

2 Contribution I

This chapter is a replica of the paper below:

- F. D. A. García, M. A. M. Miranda and J. C. S. Santos Filho, "Optimum detection for a class of stationary meteorological radars," in *Proc. 26th European Signal Processing Conference (EUSIPCO)*, pp. 2258-2262, Italy, Rome, Sept. 2018. DOI:10.23919/EUSIPCO.2018.8553329.

Optimum Detection for a Class of Stationary Meteorological Radars

Fernando Darío Almeida García, Marco Antonio Miguel Miranda,
and José Cândido Silveira Santos Filho

Abstract

Recently, an innovative low-cost approach for the construction of meteorological radars has been introduced by exploiting the correlation between the received signals from two fixed wide-beam antennas. Yet, it was then found that a very large amount of signal samples would be required to ensure a satisfactory performance of the proposed radar. On the other hand, it was also envisaged that such a problem could be circumvented by the use of more than two antennas. This work is a first step in this direction, extending the original radar proposal from two to an arbitrary number of antennas. In addition to designing an optimum detector for the new radar, we assess its performance by deriving asymptotic, closed-form expressions for the resulting detection and false-alarm probabilities. As a term of comparison, we also design and analyze a suboptimal detection scheme based on the traditional phased-array approach. Numerical examples are given to validate the provided analysis and to illustrate the performance gain achieved from the use of additional antennas.

2.1 Introduction

Radar applications have provided important advances in different technological areas, such as remote sensing, meteorology, air traffic control, spatial monitoring, and national security [1, 2, 3]. In particular, for meteorological applications, three main types of radar exist, in terms of structure and operation mode: (i) the large narrow-beam antenna; (ii) the antenna array; and (iii) spaced antennas. In the first radar type, a horn-shaped antenna and parabolic reflectors with circular aperture are used. The azimuth scanning is obtained by rotating the antenna through a motor, and the elevation scanning is obtained by changing the tilt in each rotation [4]. Because of this, the scanning cycle is relatively long (circa 15–20 min). In addition, this approach requires a very robust mechanical equipment and high maintenance costs. In the second radar type, an equivalent narrow beam is obtained by appropriately controlling the relative phases and amplitudes of each radiating element in the antenna array. Therefore, the beam position can be adjusted electronically, rendering a minimum scanning cycle, generally in the order

of microseconds [5, 6]. On the other hand, this approach has a high implementation cost due to the use of a massive number of antenna elements. Finally, the third radar type is a special employment of the second one. In particular, only a few radiating elements of the antenna array are activated to determine the position and the radial velocity of the meteorological phenomenon of interest. Interferometric techniques are then used to properly combine the amplitude and phase information of the received signals [7, 6].

In [8], an innovative low-cost, fast-scanning approach with potential use for nowcasting weather predictions was introduced. The approach is based on two stationary (i.e., fixed) wide-beam antennas. The central idea is to achieve narrow-beam resolution by exploiting the signal correlation between the two wide-beam antennas. Whenever there is a meteorological target in the intersection area between the resolution cells of the two antennas, the received antenna signals are expected to be mutually correlated. Otherwise, these signals are expected to be independent. Therefore, the amount of correlation between the antenna signals may serve as a basis for a detection algorithm. The higher the correlation in the presence of a target, the better the expected detection performance. This correlation has been derived in [8] in terms of radar parameters such as frequency bandwidth, baseline distance, and antenna directivity. Related material on the correlation between received radar signals can be found in [9, 10], although for the different contexts of a single rotating, narrow-beam antenna and polarization diversity, respectively (cf. [8] for more discussion on this).

In [11], an optimum detector was provided for the two-antenna radar scheme proposed in [8]. Also, analytical expressions were obtained for the corresponding probabilities of detection (PD) and false alarm (PFA). However, it was then observed that an extremely large amount of signal samples would be required to render the radar performance acceptable, and that such a problem could be alleviated by increasing the number of antennas.

This work is a first step in that direction. In particular, we generalize the radar scheme investigated in [8, 11] from two to an arbitrary number of antennas, by deriving the optimum detection algorithm and associated closed-form expressions of PD and PFA[1]. Sample cases are presented to show the detection improvement achieved with beyond two antennas. For comparison, a suboptimal detection algorithm is also considered, based on the traditional approach of phased arrays.

In what follows, $f_{(\cdot)}(\cdot)$ denotes probability density function (PDF); $\mathbb{E}[\cdot]$, expectation; $\mathbb{VAR}[\cdot]$, variance; $\det(\cdot)$, determinant; $(\cdot)^T$, transposition; and $(\cdot)^{-1}$, matrix inversion.

[1] The results presented herein have been used to assist in the design of meteorological radar systems for Bradar Indústria S.A., a branch of Embraer Defense and Security.

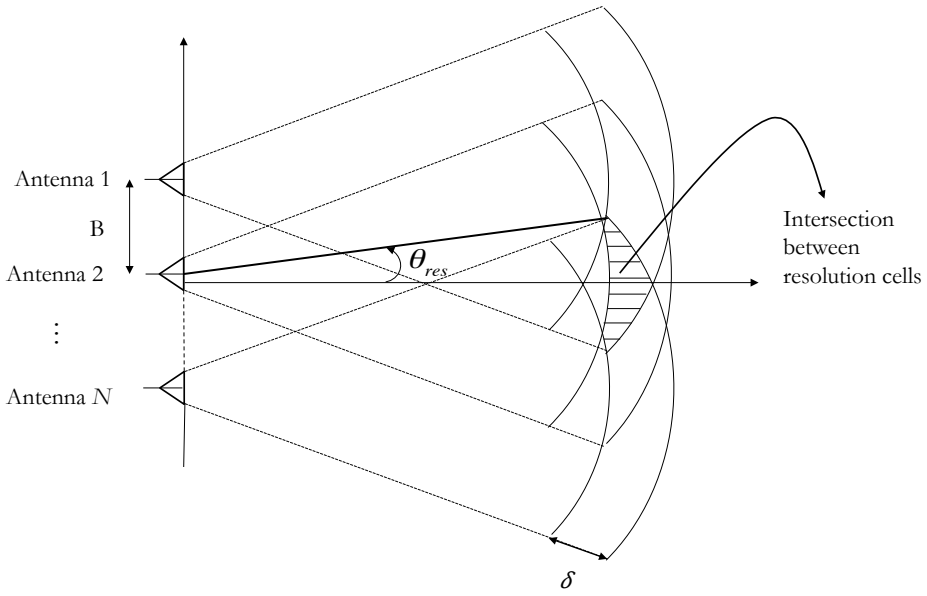

Figure 2.1 – Top view of the investigated radar system.

2.2 Radar Model

We consider a multi-static radar system composed of N fixed wide-beam antennas. The antennas are aligned and separated by a certain baseline distance B in the azimuth direction, as shown in Fig. 2.1. A single antenna transmits a linear frequency-modulated pulse, whereas all antennas receive the echo signals. In addition, pulse compression is assumed at the reception [12].

The ability of a radar system to resolve two targets over range, azimuth, or elevation defines its resolution cell [2]. Fig. 2.1 shows a top view of the range-azimuth resolution cells of each antenna, for a given range distance. The resolution cells form an intersection (hatched) region, inside of which the existence or absence of targets is to be determined. Therefore, the angular span of the intersection region gives the equivalent azimuthal resolution θ_{res} of the radar system. Note that θ_{res} decreases as the number N of antennas increases. This should be considered in practice for a proper radar design. In meteorological applications, $\theta_{\text{res}} < 2^{\text{o}}$ is typically required. As for the range resolution δ, this is given by $\delta = c/(2\Delta f)$ from the assumption of pulse compression, where c is the speed of light and Δf is the bandwidth of the transmitted signal [2].

The signal received by each antenna is a sum of the echoes coming from a large amount of scatterers within the resolution cell. These scatterers represent the meteorological phenomenon under observation (e.g., rain or clouds). Already taking into account

the presence of noise and clutter, the signals received by the antennas can be written as

$$S_{k,i} = X_{k,i} + jY_{k,i} \tag{2.1}$$

where $i \in \{1, \ldots, n\}$ is a discrete-time index, n is the number of samples observed in each antenna, $X_{k,i}$ is the in-phase component at the k-th antenna, and $Y_{k,i}$ is the associated quadrature component, $k \in \{1, \ldots, N\}$. As argued in [8], $X_{k,i}$ and $Y_{l,i}$ are mutually independent random processes, $\forall(k, l)$. In addition, assuming that the pulse repetition interval is much larger than the coherence time associated with the random motion of the scatterers, $S_{k,i}$ is independent of $S_{l,m}$, $\forall(k, l)$ and $\forall i \neq m$ [13, 14, 15]. On the other hand, depending on the absence or existence of a target in the intersection region among the antennas' resolution cells, $X_{k,i}$ and $X_{l,i}$, as well as $Y_{k,i}$ and $Y_{l,i}$, $\forall k \neq l$, can either be mutually independent or bear a certain correlation coefficient ρ_{kl}, respectively. Finally, under quite general conditions, $S_{k,i}$ can be modeled as a circularly symmetrical Gaussian random process, $\forall k$. Herein, for simplicity, we also consider that $S_{k,i}$ and $S_{l,m}$ are identically distributed, $\forall(i, k, l, m)$.

The signal variance and the correlation coefficient ρ_{kl} for an arbitrary pair of antennas have been fully characterized in [8] as a function of the radar's relevant physical parameters. Hence, no further discussion on this topic shall be presented here. Instead, our aim is to design and analyze an optimum detector for the proposed extended radar setup, in terms of arbitrary values of the variance and ρ_{kl}, $k, l \in \{1, \ldots, N\}$. This is attained in the next section.

2.3 Hypothesis Test

The fundamental problem of a radar system is to decide for the absence or existence of a target. In our case, this problem is posed over each intersection region among the antennas' resolution cells, for multiple range combinations (cf. Fig. 2.1). In so doing, the radar system scans the entire sector illuminated by the antennas. For simplicity, the observables S_{ki} defined in (2.1) shall be denoted in compact form as

$$\underline{X} \triangleq [X_{1,1}, X_{2,1}, \ldots, X_{N,1}, X_{1,2}, X_{2,2}, \ldots, X_{N,2}, \ldots, X_{1,n}, X_{2,n}, \ldots, X_{N,n}] \tag{2.2}$$

$$\underline{Y} \triangleq [Y_{1,1}, Y_{2,1}, \ldots, Y_{N,1}, Y_{1,2}, Y_{2,2}, \ldots, Y_{N,2}, \ldots, Y_{1,n}, Y_{2,n}, \ldots, Y_{N,n}]\,. \tag{2.3}$$

We have the following binary hypothesis test:

- Hypothesis $\mathcal{H}_0$: target is absent. In this case, from the radar model described in the previous section, $\underline{X}$ and $\underline{Y}$ are formed by mutually independent Gaussian components with zero mean and variance σ_0^2.

- Hypothesis $\mathcal{H}_1$: target is present. In this case, $\underline{X}$ is still independent of $\underline{Y}$, but now $X_{k,i}$ and $X_{l,i}$ (as well as $Y_{k,i}$ and $Y_{l,i}$) are jointly Gaussian random variables with zero mean, variance σ_1^2, and correlation coefficient ρ_{kl}. It is worth noting that $\sigma_1^2 > \sigma_0^2$, since σ_1^2 represents the variance of noise plus target echo, whereas σ_0^2 represents the variance of noise alone.

2.4 Detection Schemes

2.4.1 Optimum Detection

The joint PDF of $\underline{X}$ and $\underline{Y}$ can be written as [16]

$$f_{\underline{XY}}\left(\underline{X},\underline{Y}|\mathcal{H}_\nu\right) = \frac{1}{\left((2\pi)^N \det\left(\mathcal{M}_{\mathcal{H}_\nu}\right)\right)^n} \exp\left[-\frac{1}{2}\sum_{i=1}^{n}\left(\underline{X}_i{}^T \mathcal{M}_{\mathcal{H}_\nu}{}^{-1} \underline{X}_i + \underline{Y}_i{}^T \mathcal{M}_{\mathcal{H}_\nu}{}^{-1} \underline{Y}_i\right)\right], \tag{2.4}$$

where $\nu \in \{0,1\}$, depending on the hypothesis, $\underline{X}_i \triangleq [X_{1i}\, X_{2i} \cdots X_{Ni}]^T$, and $\underline{Y}_i \triangleq [Y_{1i}\, Y_{2i} \cdots Y_{Ni}]^T$. In addition, $\mathcal{M}_{\mathcal{H}_0} \triangleq \sigma_0^2\mathbf{I}$ and $\mathcal{M}_{\mathcal{H}_1} \triangleq \sigma_1^2\Sigma$ are the covariance matrices of $\underline{X}_i$ (as well as $\underline{Y}_i$) under each hypothesis, with $\mathbf{I}$ being the identity matrix and

$$\Sigma \triangleq \begin{bmatrix} 1 & \rho_{12} & \rho_{13} & \cdots & \rho_{1N} \\ \rho_{21} & 1 & \rho_{23} & & \rho_{2N} \\ \rho_{31} & \rho_{32} & 1 & & \rho_{3N} \\ \vdots & & & \ddots & \vdots \\ \rho_{N1} & \rho_{N2} & \rho_{N3} & \cdots & 1 \end{bmatrix}. \tag{2.5}$$

Note that $\mathcal{M}_{\mathcal{H}_0}$ and $\mathcal{M}_{\mathcal{H}_1}$ are $N \times N$ symmetrical matrices.

2.4.1.1 Detection Design

In a binary hypothesis test, the optimum decision (i.e., one that maximizes PD for any given PFA) is established by the Neyman-Pearson Lemma [16]. According to this, the system decides for $\mathcal{H}_1$ whenever the likelihood ratio test (LRT) of $\mathcal{H}_1$ over $\mathcal{H}_0$ exceeds a certain threshold, say γ', and it decides for $\mathcal{H}_0$ otherwise. In other words,

$$\Lambda_{\text{opt}} \triangleq \frac{f_{\underline{XY}}\left(\underline{X},\underline{Y}|\mathcal{H}_1\right)}{f_{\underline{XY}}\left(\underline{X},\underline{Y}|\mathcal{H}_0\right)} \underset{\mathcal{H}_0}{\overset{\mathcal{H}_1}{\gtrless}} \gamma'. \tag{2.6}$$

Substituting (2.4) into (2.6), and making the necessary simplifications, we obtain

$$\Lambda_{\text{opt}} = \left(\frac{\det\left(\mathcal{M}_{\mathcal{H}_0}\right)}{\det\left(\mathcal{M}_{\mathcal{H}_1}\right)}\right)^n \exp\left[-\frac{1}{2}\sum_{i=1}^{n}\left(\underline{X}_i^T \mathcal{M} \underline{X}_i + \underline{Y}_i^T \mathcal{M} \underline{Y}_i\right)\right], \tag{2.7}$$

where $\mathcal{M} \triangleq \mathcal{M}_{\mathcal{H}_1}^{-1} - \mathcal{M}_{\mathcal{H}_0}^{-1}$.

For simplicity, we use equivalently the so-called log-LRT representation, given as [1]

$$\ln\left[\Lambda_{\text{opt}}\right] \underset{\mathcal{H}_0}{\overset{\mathcal{H}_1}{\gtrless}} \ln\left[\gamma'\right]. \tag{2.8}$$

Now, absorbing the terms that do not depend on $\underline{X}_i$ and $\underline{Y}_i$ into a new corresponding decision threshold, γ, we can reformulate the decision rule as

$$W \underset{\mathcal{H}_0}{\overset{\mathcal{H}_1}{\gtrless}} \gamma, \tag{2.9}$$

where W is the new decision variable, obtained as

$$W \triangleq -\frac{1}{n}\sum_{i=1}^{n}\left(\underline{X}_i^T\mathcal{M}\underline{X}_i + \underline{Y}_i^T\mathcal{M}\underline{Y}_i\right). \tag{2.10}$$

2.4.1.2 Detection Analysis

From the Central Limit Theorem, W approaches a Gaussian distribution as the amount of signal samples approaches infinity [16]. In what follows, we consider that n is large enough to render the Gaussian assumption a good approximation, thereby allowing for an asymptotic performance analysis of the proposed radar system[2]. In this case, W can be fully characterized by its mean value and variance under each hypothesis, as calculated next.

For convenience, we obtain each element of Σ^{-1} in terms of the correlation matrix Σ as [17]

$$\Sigma^{-1}_{(p,q)} = \frac{(-1)^{p+q}\det\left(\tilde{\Sigma}\left[p,q\right]\right)}{\det\left(\Sigma\right)}, \tag{2.11}$$

with $(\cdot)_{(p,q)}$ denoting the element at the p-th row and the q-th column of a matrix, and $\tilde{\Sigma}\left[p,q\right] \in \mathbb{R}^{(N-1)\times(N-1)}$ being an auxiliary matrix obtained by removing the p-th row and the q-th column of Σ.

Now, using (2.5), (2.10), and (2.11), and applying the Laplace Theorem [17], we eventually show that the mean values of W under each hypothesis are given by

$$\mathbb{E}\left[W|\mathcal{H}_0\right] = 2\left(N - \frac{\sigma_0^2}{\sigma_1^2\det\left(\Sigma\right)}\sum_{p=1}^{N}\det\left(\tilde{\Sigma}\left[p,p\right]\right)\right) \tag{2.12}$$

$$\mathbb{E}\left[W|\mathcal{H}_1\right] = 2N\left(\frac{\sigma_1^2}{\sigma_0^2} - 1\right), \tag{2.13}$$

[2] As shall be seen from the numerical examples, the Gaussian assumption proves to be very accurate for practicable values of n, say, 100–200 samples.

and that the corresponding variances are given, respectively, by

$$\mathbb{VAR}\left[W|\mathcal{H}_0\right] = \frac{4\sigma_0^4}{n}\left(\sum_{p=1}^{N}\left(-\frac{1}{\sigma_0^2}+\frac{\det\left(\tilde{\Sigma}\left[p,p\right]\right)}{\sigma_1^2\det\left(\Sigma\right)}\right)^2+\frac{1}{\sigma_1^4\det\left(\Sigma\right)^2}\sum_{\substack{p=1\\p<q}}^{N-1}\sum_{q=2}^{N}\det\left(\tilde{\Sigma}\left[p,q\right]\right)^2\right) \tag{2.14}$$

$$\begin{aligned}\mathbb{VAR}\left[W|\mathcal{H}_1\right] = \frac{2\sigma_1^4}{n}&\left(\sum_{\substack{p=1\\p\leq q}}^{N}\sum_{q=1}^{N}\sum_{\substack{r=1\\r\leq s}}^{N}\sum_{s=1}^{N}\left(|\mathrm{sgn}(p-q)|+1\right)\left(\frac{(-1)^{p+q}\det\left(\tilde{\Sigma}\left[p,q\right]\right)}{\sigma_1^2\det(\Sigma)}-\frac{\mathbf{I}_{(p,q)}}{\sigma_0^2}\right)\right.\\&\left.\times\left(|\mathrm{sgn}(r-s)|+1\right)\left(\frac{(-1)^{r+s}\det\left(\tilde{\Sigma}\left[r,s\right]\right)}{\sigma_1^2\det(\Sigma)}-\frac{\mathbf{I}_{(r,s)}}{\sigma_0^2}\right)\left(\Sigma_{(p,r)}\Sigma_{(q,s)}+\Sigma_{(p,s)}\Sigma_{(q,r)}\right)\right),\end{aligned} \tag{2.15}$$

where $\mathrm{sgn}\left(\cdot\right)$ represents the sign function.

From (2.12)–(2.15), PFA and PD can be finally obtained with use of the following general formulas for a Gaussian decision variable along with a binary threshold detector [2]:

$$P_{\mathrm{FA}} = Q\left(\frac{\gamma-\mathbb{E}\left[W|\mathcal{H}_0\right]}{\sqrt{\mathbb{VAR}\left[W|\mathcal{H}_0\right]}}\right) \tag{2.16}$$

$$P_{\mathrm{D}} = Q\left(\frac{\gamma-\mathbb{E}\left[W|\mathcal{H}_1\right]}{\sqrt{\mathbb{VAR}\left[W|\mathcal{H}_1\right]}}\right), \tag{2.17}$$

where $Q(x) \triangleq \int_x^\infty (1/\sqrt{2\pi})\exp(-t^2/2)dt$ is the complementary cumulative distribution function of a standard (zero mean, unit variance) Gaussian random variable.

2.4.2 Phased-Array Detection

In this section, for comparison, we consider a suboptimal detection scheme based on the operation mode of a traditional phased array. In such a radar, each antenna element is assigned a certain gain and a certain phase shift, with the resulting antenna signals being added at the processing stage [6]. For simplicity, and to render a fair comparison with the optimum detector, here we assume a unity gain and a null phase shift for all antenna elements. Like for the optimum detector, we consider a collection of n signal samples for each of the N antennas. Therefore, the received signals can be written as

$$\underline{S} = \sum_{k=1}^{N}\left(\underline{X_S}_k + j\underline{Y_S}_k\right), \tag{2.18}$$

where $\underline{X_S}_k \triangleq \left[X_{k,1}, X_{k,2}, \cdots, X_{k,n}\right]^T$ and $\underline{Y_S}_k \triangleq \left[Y_{k,1}, Y_{k,2}, \cdots, Y_{k,n}\right]^T$. The PDF of $\underline{S}$ can be written as

$$f_{\underline{S}}\left(\underline{S}|\mathcal{H}_\nu\right) = \frac{1}{\left(2\pi N\sigma_{\mathcal{H}_\nu}^2\right)^n}\exp\left[-\frac{\sum_{i=1}^{n}\left(\left(\sum_{k=1}^{N}X_{k,i}\right)^2+\left(\sum_{k=1}^{N}Y_{k,i}\right)^2\right)}{2N\sigma_{\mathcal{H}_\nu}^2}\right], \tag{2.19}$$

in which $\sigma^2_{\mathcal{H}_0} = N\sigma_0^2$ and $\sigma^2_{\mathcal{H}_1} = \sigma_1^2 \mathbf{1}^T \Sigma \mathbf{1}$ represent the variance of the sum of N Gaussian components under the hypotheses $\mathcal{H}_0$ and $\mathcal{H}_1$, respectively, $\mathbf{1} = [1, 1, \cdots, 1]^T \in \mathbb{N}^N$ being the unitary vector.

2.4.2.1 Detection Design

The LRT for the phased array detector is defined as

$$\Lambda_{\text{pha}} \triangleq \frac{f_{\underline{S}}\left(\underline{S}|\mathcal{H}_1\right)}{f_{\underline{S}}\left(\underline{S}|\mathcal{H}_0\right)} \underset{\mathcal{H}_0}{\overset{\mathcal{H}_1}{\gtrless}} \gamma'. \tag{2.20}$$

Substituting (2.19) in (2.20), and after some minor simplifications, we obtain

$$\Lambda_{\text{pha}} = \left(\frac{\sigma^2_{\mathcal{H}_0}}{\sigma^2_{\mathcal{H}_1}}\right)^n \exp\left[\left(\frac{\sigma^2_{\mathcal{H}_1} - \sigma^2_{\mathcal{H}_0}}{2\sigma^2_{\mathcal{H}_1}\sigma^2_{\mathcal{H}_0}}\right) \sum_{i=1}^{n} \left\{ \left(\sum_{k=1}^{N} X_{k,i}\right)^2 + \left(\sum_{k=1}^{N} Y_{k,i}\right)^2 \right\}\right]. \tag{2.21}$$

After applying the log-LRT transformation, and since the term $\frac{\sigma^2_{\mathcal{H}_1} - \sigma^2_{\mathcal{H}_0}}{2\sigma^2_{\mathcal{H}_1}\sigma^2_{\mathcal{H}_0}}$ is always positive, we arrive at a new decision rule in terms of $X_{k,i}$ and $Y_{k,i}$ alone, namely

$$Z \underset{\mathcal{H}_0}{\overset{\mathcal{H}_1}{\gtrless}} \gamma, \tag{2.22}$$

where

$$Z \triangleq \sum_{i=1}^{n} \left\{ \left(\sum_{k=1}^{N} X_{k,i}\right)^2 + \left(\sum_{k=1}^{N} Y_{k,i}\right)^2 \right\}. \tag{2.23}$$

2.4.2.2 Detection Analysis

Note that $Z/\sigma^2_{\mathcal{H}_\nu}$ follows a chi-squared distribution with $2n$ degrees of freedom. Therefore, after a simple transformation of variables, we obtain the PDF of Z under each hypothesis as

$$f_Z\left(z|\mathcal{H}_\nu\right) = \frac{1}{z\Gamma(n)} \exp\left(-\frac{z}{2\sigma^2_{\mathcal{H}_\nu}}\right) \left(\frac{z}{2\sigma^2_{\mathcal{H}_\nu}}\right)^n, \tag{2.24}$$

where $\Gamma\left(\cdot\right)$ represents the gamma function. Finally, PFA and PD can be calculated as

$$P_{\text{FA}} = \int_{\gamma}^{\infty} f_Z\left(z|\mathcal{H}_0\right) dz = \frac{\Gamma\left(n, \frac{\gamma}{2N\sigma_0^2}\right)}{\Gamma(n)} \tag{2.25}$$

$$P_{\text{D}} = \int_{\gamma}^{\infty} f_Z\left(z|\mathcal{H}_1\right) dz = \frac{\Gamma\left(n, \frac{\gamma}{2\sigma_1^2 \mathbf{1}^T \Sigma \mathbf{1}}\right)}{\Gamma(n)}, \tag{2.26}$$

in which $\Gamma\left(\cdot,\cdot\right)$ represents the incomplete gamma function.

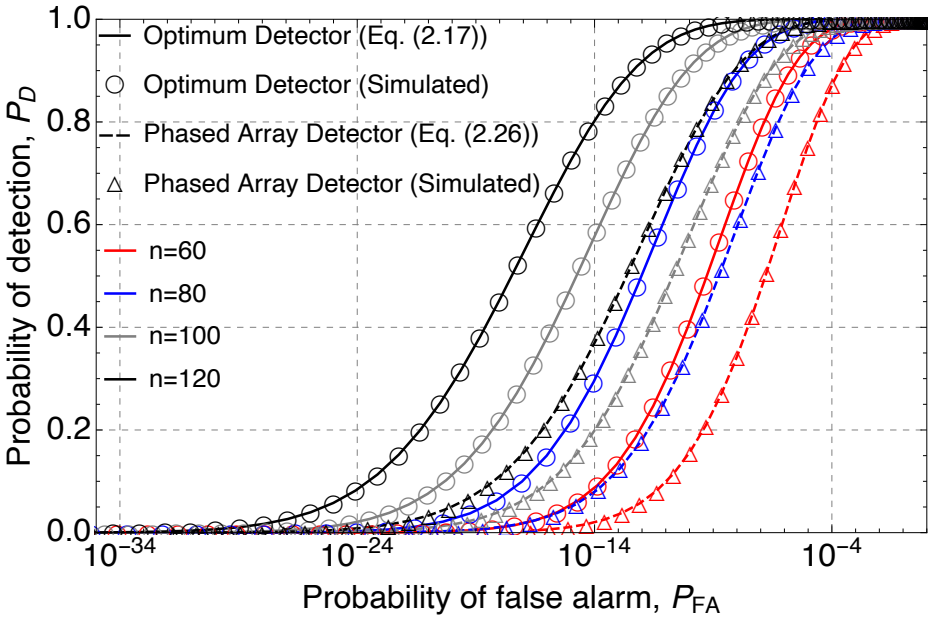

Figure 2.2 – ROC curves for the optimum and phased-array detectors ($\rho_{12} = 0.5$, $N = 2$, $\sigma_0^2 = 1$, and $\sigma_1^2 = 1.1$).

2.5 Numerical Results

In this section we present comparative numerical results in terms of the amount of antennas (N), the amount of signal samples per antenna (n), and the correlation matrix (Σ). The optimum and phased-array detectors we proposed are assessed both analytically and via simulation. For illustration purposes, we consider $\rho_{12} = 0.05$, $\rho_{13} = 0.03$, $\rho_{14} = 0.01$, $\rho_{23} = 0.05$, $\rho_{24} = 0.03$, and $\rho_{34} = 0.05$.

Fig. 2.2 shows the receiver operating characteristic (ROC) curves for both detectors, with $N = 2$, $\sigma_0^2 = 1$, $\sigma_1^2 = 1.1$, and varying n. Note how the analytical expressions we derived for the detection and false-alarm probabilities of the optimum detector perfectly agree with the simulation results, confirming the validity of the Gaussian assumption for the decision variable. Also note the improvement for both detectors as the number of samples increases, and how the optimum detector performs much better than the phased-array detector, yielding a much higher PD for any given PFA. In particular, for $P_{\text{FA}} = 10^{-10}$ and $n = 120$, the PD values are 98.1% for the optimum detector and 78.1% for the phased-array detector.

Fig. 2.3 shows the ROC curves for the optimum detector with two antennas proposed in [11] and the optimum detector with three and four antennas proposed here, for $n = 100$, $\sigma_0^2 = 1$, and $\sigma_1^2 = 1.2$. Once again, note how analytical expressions and simulation results fully match each other, validating (2.16), (2.17), (2.25), and (2.26). Also note how the optimum detector performs much better with four antennas.

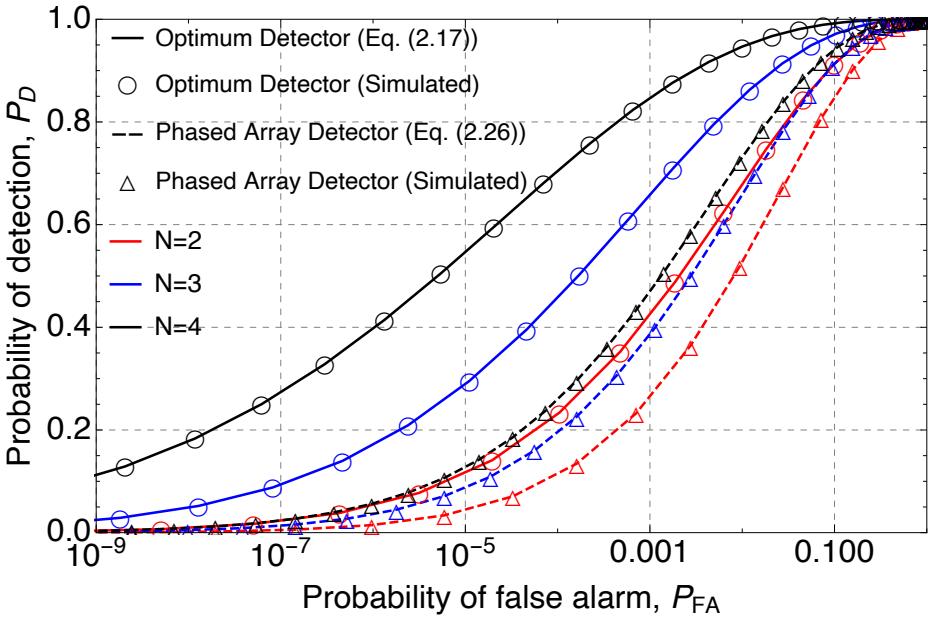

Figure 2.3 – ROC curves for the optimum and phased-array detectors ($\sigma_0^2 = 1$, $\sigma_1^2 = 1.2$, $n = 100$, $\rho_{12} = 0.05$, $\rho_{13} = 0.03$, $\rho_{14} = 0.01$, $\rho_{23} = 0.05$, $\rho_{24} = 0.03$, and $\rho_{34} = 0.05$).

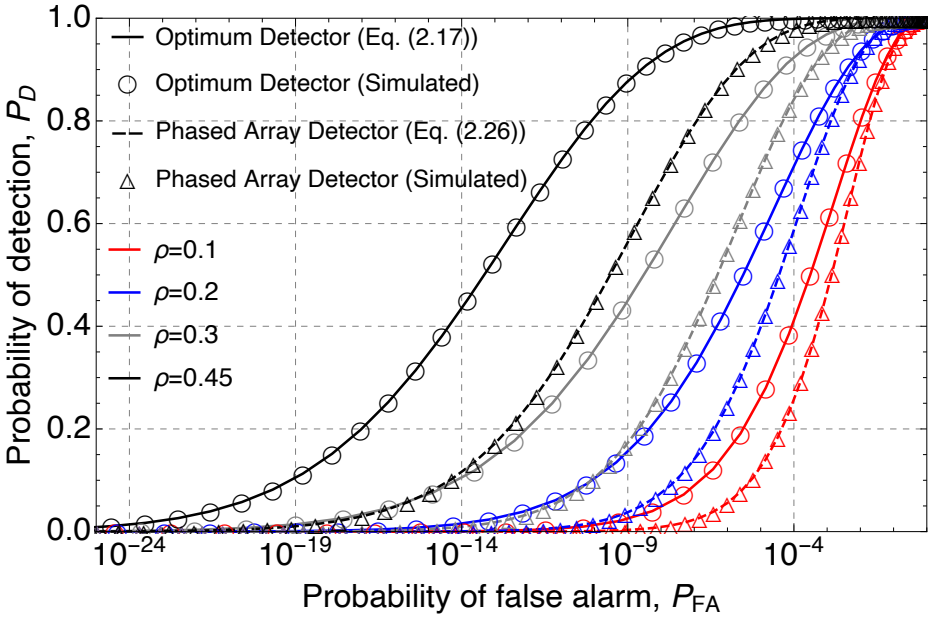

Figure 2.4 – ROC curves for the optimum and phased-array detectors ($n = 100$, $N = 2$, $\sigma_0^2 = 1$, and $\sigma_1^2 = 1.1$).

Finally, Fig. 2.4 shows the ROC curves for the optimum and phased-array detectors with two antennas, $\sigma_0^2 = 1$, $\sigma_1^2 = 1.1$, $n = 100$, and varying $\rho_{12} = \rho$. Note that, as discussed in the Introduction, the performance of each detector improves as the correlation coefficient increases.

2.6 Conclusions

In [8] and [11], an innovative approach for the construction of meteorological radars was introduced, based on two fixed wide-beam antennas. In principle, the new approach is cheaper and faster than the traditional one, which is based on a large rotating narrow-beam antenna. However, the former was observed to require an extremely high number of signal samples in order to operate effectively. In this work, we alleviated the referred drawback of this new meteorological radar paradigm by extending it from two to an arbitrary number of antennas. We not only designed the optimum and phased-array detection algorithms for the extended radar setup, but also analyzed their performances in terms of detection and false-alarm probabilities. Our results indicate that the increase in number of antennas brings a considerable performance gain.

2.7 Bibliography

[1] M. A. Richards, J. Scheer, W. A. Holm, and W. L. Melvin, *Principles of Modern Radar: Basic Principles*, 1st ed. West Perth, WA, Australia: SciTech, 2010.

[2] M. A. Richards, *Fundamentals of Radar Signal Processing*, 2nd ed. Ney York, NY, USA: McGraw-Hill, 2014.

[3] L. V. Blake, *Radar Range-performance Analysis*, 1st ed. Norwood, MA, USA: Artech House, 1986.

[4] M. Wada, J. Horikomi, and F. Mizutani, "Development of solid-state weather radar," in *Proc. IEEE Radar Conference*, CA, California, USA, May 2009, pp. 1–4.

[5] D. S. Zrnic, V. M. Melnikov, R. J. Doviak, and R. Palmer, "Scanning strategy for the multifunction phased-array radar to satisfy aviation and meteorological needs," *IEEE Geosci. Remote Sens. Lett.*, vol. 12, no. 6, pp. 1204–1208, Jun. 2015.

[6] J. Li and P. Stoica, *MIMO Radar Signal Processing*, 1st ed. New Jersey, NJ, USA: John Wiley & Sons, 2009.

[7] G. Zhang and R. J. Doviak, "Spaces-antenna interferometry to detect and locate subvolume inhomogeneities of reflectivity: An analogy with monopulse radar," in *Proc. J. Atmos. Ocean. Technol*, Nov. 2008, pp. 1921–1938.

[8] M. A. M. Miranda, J. C. S. Santos Filho, G. Fraidenraich, M. D. Yacoub, J. R. Moreira Neto, and Y. C. Zúñiga, "Correlation between signals from spaced antennas of stationary meteorological radars," *IEEE Trans. Geosci. Remote Sens.*, vol. 52, no. 6, pp. 3116–3124, Jun. 2014.

[9] G. Zhang, R. J. Doviak, J. Vivekanandan, and T. Yu, "Angular and range interferometry to measure wind," *Radio Sci*, vol. 38, no. 6, pp. 14–1–14–9, Dec. 2003.

[10] A. Ryzhkov, D. Zrnic, J. Hubbert, V. Bringi, J. Vivekanandan, and E. Brandes, "Interpretation of polarimetric radar covariance matrix for meteorological scatterers," in *Proc. Geosci. Remote Sens. Symp.*, vol. 4, 2000, pp. 1584–1586.

[11] M. A. M. Miranda, J. C. S. Santos Filho, G. Fraidenraich, M. D. Yacoub, J. R. Moreira Neto, and Y. C. Zúñiga, "Radar meteorológico com antenas fixas: Projeto e análise de detector ótimo," in *Proc. XXXI Brazilian Symposium of Telecommunications*, Fortaleza, Brazil, 01-04, Sept. 2013.

[12] D. K. Barton, *Radar Equations for Modern Radar*, 1st ed. Massachusetts, MA, USA: Artech House, 2013.

[13] H. Sauvageot, *Radar Meteorology*. Massachusetts, MA, USA: Artech House, 1992.

[14] F. D. A. García, M. A. M. Miranda, and J. C. S. Santos Filho, "Detecção ótima e subótima para um radar meteorológico com três antenas fixas," in *Proc. XXXIII Brazilian Symposium of Telecommunications*, Juiz de Fora, MG, Brazil, Sept. 2015.

[15] F. D. A. García, "Detecção Ótima e subótima para um radar meteorológico com três antenas fixas de feixe largo," Master's thesis, University of Campinas (UNICAMP), Campinas, SP, Brazil, Jan. 2016.

[16] A. Leon-Garcia, *Probability and Random Processes for Electrical Engineering*, 3rd ed. New Jersey, NJ, USA: Pearson Prentice Hall, 1994.

[17] A. Arnold and I. Guessarian, *Math for Computer Science*, 2nd ed. Prentice Hall, 1996.

3 Contribution II

This chapter is a replica of the paper below:

- F. D. A. García, H. R. C. Mora, N. V. O. Garzón and J. C. S. Santos Filho, "Alternative representations for the probability of detection of non-fluctuating targets," *IET Electron. Lett.*, vol. 56, no. 21, pp. 1136-1139, Oct. 2020. DOI:10.1049/el.2020.1810.

Alternative Representations for the Probability of Detection of Non-fluctuating Targets

Fernando Darío Almeida García, Henry Ramiro Carvajal Mora, Nathaly Verónica Orozco Garzón, and José Cândido Silveira Santos Filho

Abstract

We derive a closed-form exact expression and a fast convergent series for the probability of phased-array detection of non-fluctuating targets embedded in complex white Gaussian noise. To be realistic, we assume that the amplitude of the target echoes and the noise power are unknown parameters. Our series representation achieved impressive savings in computational load and computation time when compared to the numerical evaluation of the existing integral-form solution.

3.1 Introduction

A major concern in any radar system is to decide whether or not a target is present in a certain range, angle, and Doppler bin [1]. Different types of interference can hinder the detection process, including thermal noise, ground clutter, sea clutter, and jamming. Moreover, due to the inherent randomness of the interference and target returns, the radar performance must be given in terms of statistical metrics, such as the probability of detection (PD) and the probability of false alarm (PFA).

The optimal decision about the presence or absence of a target is obtained through the *likelihood ratio test* (LRT). This decision is based on the Neyman-Pearson criterion, which maximizes PD for any given PFA [2]. The LRT has been explored in a wide variety of applications. Yet it contains a significant limitation. To provide an optimal decision, the LRT requires full knowledge of the probability density function (PDF) for the interference and target returns. Of course, this is too strong a requirement that most practical radar problems fail to meet. A more realistic strategy emerged to address the cases in which the PDF parameters are unknown: the so-called *generalized likelihood ratio test* (GLRT) [3]. Although there is no optimality associated with the GLRT, in practice it turns out to work quite well. All the unknown PDF parameters are replaced by their maximum-likelihood estimates (MLE). This structure allows the GLRT to work over a much wider range of scenarios than the LRT.

Well-known detectors considering *non-fluctuating* targets along with a single echo sample [3], coherent integration [1], and non-coherent integration [2, 4] have been ana-

lyzed under the LRT framework. On the other hand, detectors considering non-fluctuating targets and the GLRT can be found in [2, 5, 6]. These detectors assumed a partial or complete lack of knowledge about the amplitude of the target echo and the noise power. Also, the rapid increase in the use of phased-array radars has led to the development of more complex GLRT detectors that operate over *fluctuating* targets (cf. [7, 8, 9] for more discussion on this). In any case, due to the mathematical intricacy of the detection statistics, the PD performance of most GLRT detectors have been so far obtained in integral form only, computed through numerical integration, or estimated via Monte-Carlo simulations.

In this work, we address the phased-array detection of weak signals in background noise. Specifically, we consider a non-fluctuating target embedded in complex white Gaussian noise, with both the target amplitude and the noise power being unknown. The open technical literature contains no closed-form solutions or analytically tractable approximations for the associated detection performance. This is because the computation of the PD requires evaluating a cumbersome PDF for the target-plus-noise scenario [10, 11]. Herein we derive an exact closed-form expression and a fast convergent series representation for the aforementioned PD. Our closed-form expression is given in terms of the bivariate Fox H-function, whereas our series representation is obtained by exploiting the orthogonal selection of poles in Cauchy's residue theorem. The series proves efficient and computationally attractive, achieving a high accuracy even for a small number of terms, thereby showing a remarkable reduction in the computational load and in the computation time as compared to the numerical evaluation of the existing integral-form solution.

3.2 System Model

We consider a linear phased-array radar composed of N antennas, each of which receives a collection of M echo samples. The overall received signals can be written in matrix form as

$$\mathbf{X} \triangleq \begin{pmatrix} X_{1,1} & X_{2,1} & \cdots & X_{N,1} \\ X_{1,2} & X_{2,2} & \cdots & X_{N,2} \\ \vdots & \vdots & \ddots & \vdots \\ X_{1,M} & X_{2,M} & \cdots & X_{N,M} \end{pmatrix} \tag{3.1}$$

$$\mathbf{Y} \triangleq \begin{pmatrix} Y_{1,1} & Y_{2,1} & \cdots & Y_{N,1} \\ Y_{1,2} & Y_{2,2} & \cdots & Y_{N,2} \\ \vdots & \vdots & \ddots & \vdots \\ Y_{1,M} & Y_{2,M} & \cdots & Y_{N,M} \end{pmatrix}, \tag{3.2}$$

where $X_{n,m}$ and $Y_{n,m}$ represent the in-phase and quadrature components, respectively, $m \in \{1, 2, \ldots, M\}$ is a discrete-time index, and $n \in \{1, 2, \ldots, N\}$ is a spatial index that identifies each antenna.

Herein, the radar detection relies on a standard binary hypothesis test:

- Hypothesis $\mathcal{H}_0$: target is absent. In this case, due to the noise alone, the components of $\mathbf{X}$ and $\mathbf{Y}$ can be modeled as independent Gaussian random variables (RV) with zero mean and unknown variance σ^2.
- Hypothesis $\mathcal{H}_1$: target is present. In this case, the received signals are composed of noise plus target echoes. Consequently, the in-phase components $X_{1,m}, X_{2,m}$, $\cdots, X_{N,m}$ $(\forall m)$, can be modeled as independent Gaussian RVs with unknown means $\mu_{X_1}, \mu_{X_2}, \cdots, \mu_{X_N}$, respectively, and unknown variance σ^2. Similarly, the quadrature components, $Y_{1,m}, Y_{2,m}, \cdots, Y_{N,m}$ $(\forall m)$ can be modeled as independent Gaussian RVs with unknown means $\mu_{Y_1}, \mu_{Y_2}, \cdots, \mu_{Y_N}$, respectively, and unknown variance σ^2.

Taking into account the above description, the joint PDF of $\mathbf{X}$ and $\mathbf{Y}$ under the hypothesis $\mathcal{H}_0$ is given by

$$f_{\mathbf{XY}}\left(\mathbf{X}, \mathbf{Y}|\mathcal{H}_0; \sigma^2\right) = \frac{\exp\left[-\frac{1}{2\sigma^2}\sum_{m=1}^{M}\left(\mathbf{X}_m^T\mathbf{X}_m + \mathbf{Y}_m^T\mathbf{Y}_m\right)\right]}{\left(2\pi\sigma^2\right)^{MN}}, \tag{3.3}$$

where, for convenience, we define $\mathbf{X}_m \triangleq [X_{1,m}, X_{2,m}, \cdots, X_{N,m}]^T$ and $\mathbf{Y}_m \triangleq [Y_{1,m}, Y_{2,m}, \cdots, Y_{N,m}]^T$. On the other hand, the joint PDF of $\mathbf{X}$ and $\mathbf{Y}$ under the hypothesis $\mathcal{H}_1$ is given by

$$f_{\mathbf{XY}}\left(\mathbf{X}, \mathbf{Y}|\mathcal{H}_1; \boldsymbol{\mu}_X, \boldsymbol{\mu}_Y, \sigma^2\right) = \frac{1}{\left(2\pi\sigma^2\right)^{MN}} \times \exp\left[-\frac{1}{2\sigma^2}\sum_{m=1}^{M}\left(\mathbf{M}_{\mathbf{X},m}^T\mathbf{M}_{\mathbf{X},m} + \mathbf{M}_{\mathbf{Y},m}^T\mathbf{M}_{\mathbf{Y},m}\right)\right], \tag{3.4}$$

where once again we define $\mathbf{M}_{\mathbf{X},m} \triangleq \mathbf{X}_m - \boldsymbol{\mu}_X$ and $\mathbf{M}_{\mathbf{Y},m} \triangleq \mathbf{Y}_m - \boldsymbol{\mu}_Y$, with $\boldsymbol{\mu}_X \triangleq [\mu_{X_1}, \mu_{X_2}, \cdots, \mu_{X_N}]^T$ and $\boldsymbol{\mu}_Y \triangleq [\mu_{Y_1}, \mu_{Y_2}, \cdots, \mu_{Y_N}]^T$.

In such a scenario, the GLRT decision rule can be written as [3]

$$\frac{f_{\mathbf{XY}}\left(\mathbf{X}, \mathbf{Y}|\mathcal{H}_1; \hat{\boldsymbol{\mu}}_X, \hat{\boldsymbol{\mu}}_Y, \hat{\sigma}_1^2\right)}{f_{\mathbf{XY}}\left(\mathbf{X}, \mathbf{Y}|\mathcal{H}_0; \hat{\sigma}_0^2\right)} \underset{\mathcal{H}_0}{\overset{\mathcal{H}_1}{\gtrless}} \Upsilon, \tag{3.5}$$

where Υ is an arbitrary threshold; $\hat{\sigma}_0^2$ is the MLE for σ^2, obtained from (3.3); and $\hat{\sigma}_1^2$, $\hat{\boldsymbol{\mu}}_X$, and $\hat{\boldsymbol{\mu}}_Y$ are the MLEs for σ^2, $\boldsymbol{\mu}_X$, and $\boldsymbol{\mu}_Y$, respectively, obtained from (3.4). An equivalent

decision rule for (3.5) is defined as [3, 11]

$$Z \underset{\mathcal{H}_0}{\overset{\mathcal{H}_1}{\gtrless}} \gamma, \tag{3.6}$$

where Z is a modified detection statistic obtained in terms of $\mathbf{X}$ and $\mathbf{Y}$, and γ is a corresponding new threshold. It has been shown that, conditioned on $\mathcal{H}_0$, Z follows a central F-distribution with PDF given by [3, 1]

$$f_Z\left(z|\mathcal{H}_0\right) = \frac{(M-1)^{(M-1)N} z^{N-1} (M+z-1)^{-MN}}{B(N,(M-1)N)}, \tag{3.7}$$

where $B(\cdot,\cdot)$ is the beta function [12, Eq. (5.12.3)]. Moreover, conditioned on $\mathcal{H}_1$, Z follows a doubly noncentral F-distribution with PDF given by [11, 10]

$$f_Z\left(z|\mathcal{H}_1\right) = \frac{\left(\frac{M-1}{M+z-1}\right)^{MN-N} \left(\frac{z}{M+z-1}\right)^{N} \exp\left(-M\Psi\right) \ {}_1F_1\left(MN; N; \frac{zM\Psi}{M+z-1}\right)}{z\ B(N, MN-N)}, \tag{3.8}$$

where $\Psi \triangleq \sum_{n=1}^{N} \mathrm{SNR}_n$, with $\mathrm{SNR}_n \triangleq (\mu_{X_n}^2 + \mu_{Y_n}^2)/2\sigma^2$ being the signal-to-noise ratio at the n-th antenna and ${}_1F_1\left(\cdot;\cdot;\cdot\right)$ being the Kummer confluent hypergeometric function [12, Eq. (13.1.2)].

3.3 Known Integral-Form Detection Performance

The detection performance of any radar system is governed by its PFA and PD. Using (3.7) and (3.8), these metrics have been calculated as [11]

$$\begin{aligned} P_{\mathrm{FA}} &\triangleq \int_{\gamma}^{\infty} f_Z\left(z|\mathcal{H}_0\right) \mathrm{d}z \\ &= \frac{B_{\frac{1-M}{\gamma}}(MN-N, 1-MN)}{\left(\frac{M-1}{1-M}\right)^{N-MN} B(N, MN-N)} \end{aligned} \tag{3.9}$$

$$\begin{aligned} P_{\mathrm{D}} &\triangleq \int_{\gamma}^{\infty} f_Z\left(z|\mathcal{H}_1\right) \mathrm{d}z \\ &= \frac{(M-1)^{MN-N} \exp\left(-M\Psi\right)}{B(N, MN-N)} \\ &\quad \times \int_{\gamma}^{\infty} z^{N-1} \left(\frac{1}{M+z-1}\right)^{MN} \ {}_1F_1\left(MN; N; \frac{zM\Psi}{M+z-1}\right) \mathrm{d}z, \end{aligned} \tag{3.10}$$

where $B_{(\cdot)}(\cdot,\cdot)$is the incomplete beta function [12, Eq. (8.17.1)]. To our best knowledge, no closed-form solution or analytically tractable approximation is available for (3.10). Next we provide them both.

3.4 Closed-form Detection Performance

In this section, we derive a novel closed-form expression for (3.10), given in terms of the bivariate Fox H-function. We begin by using [13, Eq. (07.20.26.0006.01)] to rewrite (3.10) as

$$P_{\mathrm{D}} = \frac{(M-1)^{MN-N}\exp(-M\Psi)}{\Gamma(MN-N)} \int_{\gamma}^{\infty} z^{N-1} \left(\frac{1}{M+z-1}\right)^{MN} \times G_{1,2}^{1,1}\left[\begin{array}{c|c} 1-MN & \\ 0, 1-N & \dfrac{zM\Psi}{1-z-M} \end{array} \right] \mathrm{d}z, \tag{3.11}$$

where $G_{m,n}^{p,q}[\cdot]$ is the Meijer's G-function [12, Eq. (16.17.1)]. Then, we replace the Meijer's G-function by its contour integral representation [13, Eq. (07.34.02.0001.01)]:

$$P_{\mathrm{D}} = \frac{(M-1)^{MN-N}\exp(-M\Psi)}{\Gamma(MN-N)} \int_{\gamma}^{\infty} z^{N-1} \left(\frac{1}{M+z-1}\right)^{MN} \times \left(\frac{1}{2\pi j}\right) \oint_{\mathcal{L}_{\mathbf{s},1}^{*}} \frac{\Gamma(s_1)\Gamma(MN-s_1)\left(-\frac{zM\Psi}{M+z-1}\right)^{-s_1}}{\Gamma(N-s_1)} \mathrm{d}s_1 \mathrm{d}z, \tag{3.12}$$

where $\mathcal{L}_{\mathbf{s},1}^{*}$ is a closed complex contour that separates the poles of the gamma function $\Gamma(s_1)$ from the poles of $\Gamma(MN-s_1)$. Since $\int_{\gamma}^{\infty} |f_Z(z|\mathcal{H}_1)|\,\mathrm{d}z < \infty$, we can invoke Fubini's theorem to interchange the order of integration:

$$P_{\mathrm{D}} = \frac{(M-1)^{MN-N}\exp(-M\Psi)}{(2\pi j)\Gamma(MN-N)} \oint_{\mathcal{L}_{\mathbf{s},\mathbf{1}}^{*}} \frac{\Gamma(s_1)\Gamma(MN-s_1)(-M\Psi)^{-s_1}}{\Gamma(N-s_1)} \times \int_{\gamma}^{\infty} z^{N-s_1-1}(M+z-1)^{s_1-MN}\mathrm{d}z\ \mathrm{d}s_1. \tag{3.13}$$

Now, solving the inner real integral, we obtain

$$P_{\mathrm{D}} = \frac{\left(\frac{M-1}{1-M}\right)^{MN-N}\exp(-M\Psi)}{\Gamma(MN-N)} \left(\frac{1}{2\pi j}\right) \oint_{\mathcal{L}_{\mathbf{s},\mathbf{1}}^{*}} \frac{(-M\Psi)^{-s_1}\Gamma(s_1)\Gamma(MN-s_1)}{\Gamma(N-s_1)} \times B_{\frac{1-M}{\gamma}}(MN-N, -MN+s_1+1)\ \mathrm{d}s_1. \tag{3.14}$$

Finally, after using the complex integral representation of the incomplete beta function [13, Eq. (06.19.07.0001.01)], we can rewrite (3.14) in closed-form as

$$P_{\mathrm{D}} = \Phi\ H_{1,0:2,0:2,0}^{0,1:0,1:0,1}\left[\begin{array}{c|c} -M\Psi & (A,\alpha):(B,\beta):(D,\delta) \\ -\frac{1-M}{\gamma} & (-):(-):(-) \end{array} \right] \tag{3.15}$$

where $H_{v,w:v_1,w_1:v_2,w_2}^{p,q:p_1,q_1:p_2,q_2}[\cdot]$ is the bivariate Fox H-function defined in [14], $\Phi = \exp(-M\Psi)$ $((M-1)/\gamma)^{MN-N}/\Gamma(MN-N)$, $A = [-MN-1]$, $\alpha = [-1,-1]$, $B = [0,1]$, $\beta = [0,1]$, $D = [0,1]$, and $\delta = [MN-N+1, 1]$. (As stated in [14], an empty vector or matrix, denoted as (–), is interpreted as unity.)

An important remark is in order. Although the Fox H-function is still unavailable as a built-in routine in standard computing software such as MATHEMATICA,

MATLAB, or MAPLE, the technical community has alleviated this drawback by developing Python and MATHEMATICA routines for the Fox H-function with up to four variables (cf. [15, 16] for more discussion on this). Alternatively, in the next section we provide a fast convergent series representation for (3.15) that, as shall be seen, requires only a few dozen terms to achieve an outstanding accuracy.

3.5 Efficient Series Representation

In this section, we derive a series representation for (3.15) by exploiting the orthogonal separation of poles in Cauchy's residue theorem. To this end, we consider two suitable closed contours: (i) $\mathcal{L}_{\mathbf{s,1}}$ is a contour that separates the poles of $\Gamma(s_1)$ from those of $\Gamma(MN-s_1-s_2)$, and (ii) $\mathcal{L}_{\mathbf{s,2}}$ is a contour that separates the poles of $\Gamma(s_2)$ from those of $\Gamma(MN-s_1-s_2)$ and $\Gamma(MN-N-s_2)$. Thus, we can express (3.15) through the sum of residues as [17]

$$P_{\mathrm{D}} = \Phi \sum_{k=0}^{\infty}\sum_{l=0}^{\infty} \mathrm{Res}\left[\Xi\left(s_1,s_2\right); s_1=-k, s_2=-l\right], \tag{3.16}$$

where $\mathrm{Res}\left[\Xi\left(s_1,s_2\right); s_1-k, s_2=-l\right]$ denotes the residue of $\Xi\left(s_1,s_2\right)$ evaluated at the poles $s_1=-k$ and $s_2=-l$, and

$$\Xi\left(s_1,s_2\right) \triangleq \frac{\Gamma(s_1)\Gamma(s_2)\Gamma(MN-N-s_2)\Gamma(MN-s_1-s_2)(-M\Psi)^{-s_1}\left(-\frac{1-M}{\gamma}\right)^{-s_2}}{\Gamma(N-s_1)\Gamma(MN-N-s_2+1)} \tag{3.17}$$

is the integration kernel of (3.15). Now, applying the residue operation in (3.16) and recalling that $\Gamma(s_1)$ and $\Gamma(s_2)$ generate simple poles at all non-positive integers [12, Eq. (5.2.1)], we obtain

$$\begin{aligned} P_{\mathrm{D}} =& \Phi \sum_{k=0}^{\infty}\sum_{l=0}^{\infty} \left\{ \frac{(-1)^{k+l}\Gamma(l+MN-N)\Gamma(k+l+MN)\Gamma(l+MN-N+1)}{k!\; l!\; \Gamma(k+N)} \right. \\ & \left. \times (-M\Psi)^k \left(-\frac{1-M}{\gamma}\right)^l \right\}. \end{aligned} \tag{3.18}$$

Finally, using [12, Eq. (15.2.1)], and after mathematical simplifications, we reduce (3.18) to

$$\begin{aligned} P_{\mathrm{D}} =& \exp(-M\Psi)\left(\frac{M-1}{\gamma}\right)^{MN-N} \sum_{k=0}^{\infty} \left\{ \frac{\Gamma(k+MN)(M\Psi)^k}{k!\;\Gamma(k+N)} \right. \\ & \left. \times\; {}_2\tilde{F}_1\left(k+MN, MN-N; MN-N+1; \frac{1-M}{\gamma}\right) \right\}, \end{aligned} \tag{3.19}$$

where ${}_2\tilde{F}_1(a,b;c;x) = {}_2F_1(a,b;c;x)/\Gamma(c)$ is the regularized Gauss hypergeometric function, with ${}_2F_1(\cdot,\cdot;\cdot;\cdot)$ being the Gauss hypergeometric function [12, Eq. (15.1.1)].

It is worth noting that (3.19) is an original analytical contribution of this work that can be quickly executed on an ordinary desktop computer, using well-known

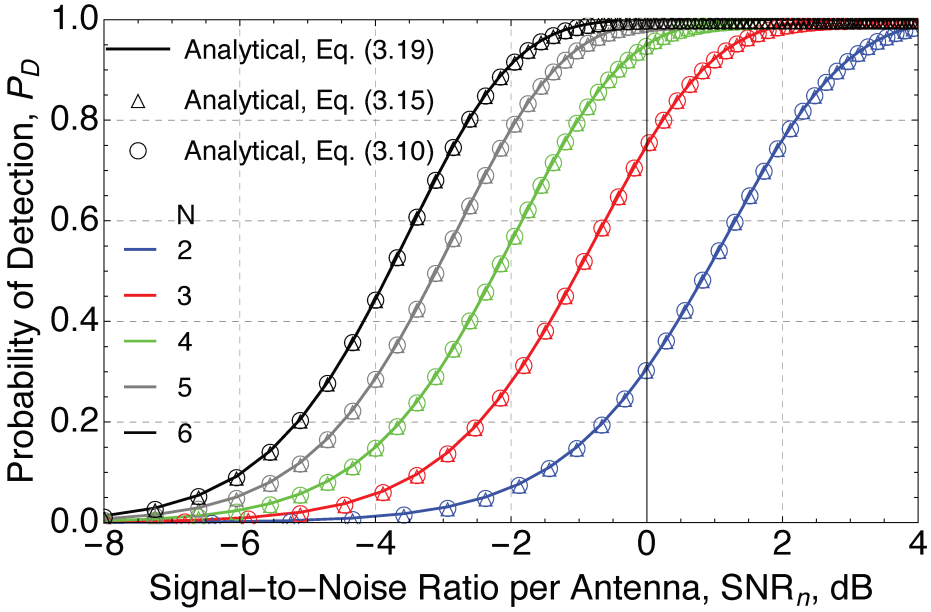

Figure 3.1 – P_{D} vs SNR_n: $M = 10$, $\mathrm{P}_{FA} = 10^{-8}$, and different values of N.

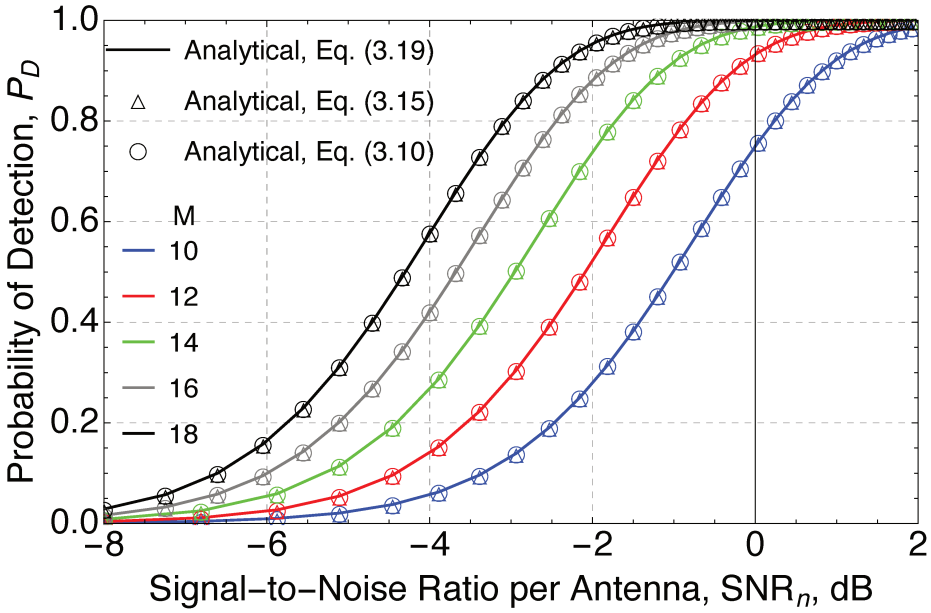

Figure 3.2 – P_{D} vs SNR_n: $N = 4$, $\mathrm{P}_{FA} = 10^{-8}$, and different values of M.

mathematical functions that are readily available for calculation. Importantly, a few dozen terms suffice to attain highly accurate results, as shown next.

3.6 Numerical Results and Discussions

In this section, we validate our analytical contributions and discuss representative sample results. For this purpose, we plot receiver operating characteristic (ROC)

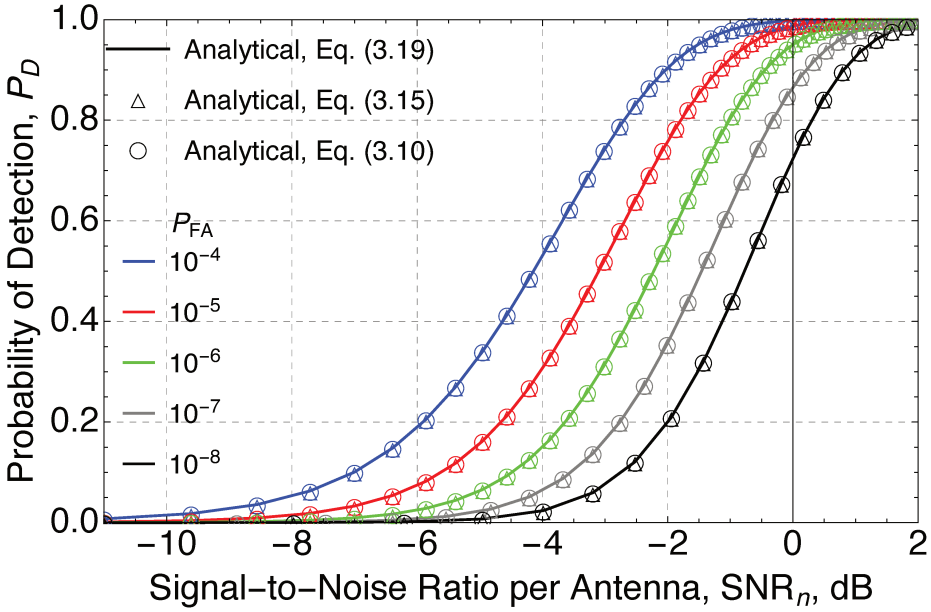

Figure 3.3 – P_{D} vs SNR_n: $M = 10$, $N = 4$, and different values of PFA.

Table 3.1 – Test cases

Case	Parameter settings	P_{D}
1	$M = 10$, $N = 4$, $P_{\mathrm{FA}} = 10^{-4}$, $\mathrm{SNR}_n = -5$ dB	33.26 %
2	$M = 10$, $N = 3$, $P_{\mathrm{FA}} = 10^{-4}$, $\mathrm{SNR}_n = -5$ dB	18.85 %
3	$M = 15$, $N = 4$, $P_{\mathrm{FA}} = 10^{-4}$, $\mathrm{SNR}_n = -5$ dB	76.29 %
4	$M = 20$, $N = 4$, $P_{\mathrm{FA}} = 10^{-4}$, $\mathrm{SNR}_n = -5$ dB	95.32 %
5	$M = 8$, $N = 4$, $P_{\mathrm{FA}} = 10^{-5}$, $\mathrm{SNR}_n = -5$ dB	5.954 %
6	$M = 8$, $N = 4$, $P_{\mathrm{FA}} = 10^{-6}$, $\mathrm{SNR}_n = -5$ dB	1.845 %
7	$M = 12$, $N = 5$, $P_{\mathrm{FA}} = 10^{-5}$, $\mathrm{SNR}_n = -3$ dB	90.40 %
8	$M = 12$, $N = 5$, $P_{\mathrm{FA}} = 10^{-5}$, $\mathrm{SNR}_n = -2$ dB	98.31 %

curves. Moreover, we assess the efficiency of (3.19) as compared to numerically integrating (3.10). Herein, (3.10) and (3.15) are evaluated by using the fastest MATHEMATICA's numerical integration method, "`GlobalAdaptive`", with an accuracy goal of 10^{-10}.

As mentioned previously, we make use of the ROC curves, P_{D} vs SNR_n, to corroborate our novel expressions. More specifically, we vary the number of antennas, the number of samples, and the PFA, as shown in Figs. 3.1–3.3. In (3.19), the number of terms was set to 50. For illustration purposes, we consider an homogeneous scenario in which the value of SNR_n is the same $\forall n \in \{1, 2, \ldots, N\}$. Observe that (3.9) is a transcendental equation for γ. Therefore, it has to be solved numerically for any given value of P_{FA}. Observe the perfect agreement between our analytical results, (3.15) and (3.19), and those in (3.10).

Now, to evaluate the efficiency of (3.19) we define 8 test cases, each with a

Table 3.2 – Efficiency of (3.19) as compared to (3.10)

Case	ϵ	Terms	Computation Time for (3.10)	Computation Time for (3.19)	Time Saving
1	6.90×10^{-10}	39	61.85 $[\mu s]$	4.01 $[\mu s]$	93.51 %
2	5.84×10^{-10}	33	40.43 $[\mu s]$	3.24 $[\mu s]$	91.97 %
3	8.90×10^{-10}	50	129.70 $[\mu s]$	5.88 $[\mu s]$	95.46 %
4	5.33×10^{-10}	61	205.30 $[\mu s]$	8.58 $[\mu s]$	95.82 %
5	7.92×10^{-10}	33	42.48 $[\mu s]$	3.25 $[\mu s]$	92.34 %
6	7.11×10^{-10}	34	47.09 $[\mu s]$	3.23 $[\mu s]$	93.13 %
7	8.70×10^{-10}	68	130.19 $[\mu s]$	9.24 $[\mu s]$	92.89 %
8	7.75×10^{-10}	80	129.24 $[\mu s]$	11.64 $[\mu s]$	90.99 %

specific parameter setting and its corresponding P_{D}, as shown in Table 3.1. With this at hand, Table 3.2 illustrates the efficiency of (3.19) by showing the truncation error, the required number of terms, and the associated time saving to achieve the same accuracy goal imposed to (3.10), i.e., around 10^{-10}. The truncation error is expressed as $\epsilon = |P_{\mathrm{D}} - \overline{P_{\mathrm{D}}}|$, where $\overline{P_{\mathrm{D}}}$ is the probability of detection obtained via the numerical integration of (3.10). Observe that across all cases no more than 80 terms were required. Moreover, the computation time dropped dramatically, above 90%. Such an impressive reduction can lead to major savings in computational load if one wants to evaluate the detection performance over an entire area or volume covered by the radar system.

3.7 Conclusions

We derived a closed-form exact expression and a fast convergent series for the detection probability of non-fluctuating targets embedded in Gaussian noise. No knowledge was assumed about the target amplitude and noise power, as it turns out to be the case for most applications in practice. Numerical results corroborated the validity and accuracy of our analytical expressions. Our series representation proved particularly attractive, as it allows for remarkable savings in computational load and computation time.

3.8 Bibliography

[1] M. A. Richards, J. Scheer, W. A. Holm, and W. L. Melvin, *Principles of Modern Radar: Basic Principles*, 1st ed. West Perth, WA, Australia: SciTech, 2010.

[2] S. M. Kay, *Fundamentals of Statistical Signal Processing: Estimation Theory*, 1st ed. New Jersey, NJ, USA: Prentice Hall PTR, 1993.

[3] ——, *Fundamentals of Statistical Signal Processing: Detection Theory*, 2nd ed. New Jersey, NJ, USA: Prentice Hall PTR, 1998.

[4] F. D. A. García, M. A. M. Miranda, and J. C. S. Santos Filho, "Optimum detection for a class of stationary meteorological radars," in *Proc. 26th European Signal Processing Conference (EUSIPCO)*, Rome, Italy, Sept. 2018, pp. 2258–2262.

[5] E. Conte, A. D. Maio, and C. Galdi, "Signal detection in compound-gaussian noise: Neyman-Pearson and CFAR detectors," *IEEE Trans. Signal Process.*, vol. 48, no. 2, pp. 419–428, Feb. 2000.

[6] S. M. Kendall and A. Stuart, *The Advanced Theory of Statistics*, 2nd ed. New York, NY, USA: Macmillan, 1979.

[7] S. Bidon, O. Besson, and J. Tourneret, "The adaptive coherence estimator is the Generalized Likelihood Ratio Test for a class of heterogeneous environments," *IEEE Signal Process. Lett.*, vol. 15, pp. 281–284, 2008.

[8] E. J. Kelly, "An adaptive detection algorithm," *IEEE Trans. Aerosp. Electron. Syst.*, vol. AES-22, no. 2, pp. 115–127, Mar. 1986.

[9] S. Bose and A. O. Steinhardt, "Optimum array detector for a weak signal in unknown noise," *IEEE Trans. Aerosp. Electron. Syst.*, vol. 32, no. 3, pp. 911–922, Jul. 1996.

[10] W. G. Bulgren, "On representations of the doubly non-central F distribution," *J. Amer. Statist.*, vol. 66, no. 333, pp. 184–186, Mar. 1971.

[11] S. S. Haykin and A. O. Steinhardt, *Adaptive Radar Detection and Estimation*, 1st ed. New Jersey, NJ, USA: J. Wiley, 1992.

[12] F. W. J. Olver, D. W. Lozier, R. F. Boisvert, and C. W. Clark, *NIST Handbook of Mathematical Functions*, 1st ed. Washington, DC: US Dept. of Commerce: National Institute of Standards and Technology (NIST), 2010.

[13] Wolfram Research, Inc. (2018), *Wolfram Research*, Accessed: Sept. 19, 2020. [Online]. Available: http://functions.wolfram.com

[14] A. M. Mathai, R. K. Saxena, and H. J. Haubold, *The H-function: Theory and Applications*. New York, NY, USA: Springer, 2009.

[15] F. D. G. Almeida, A. C. F. Rodriguez, G. Fraidenraich, and J. C. S. S. Filho, "CA-CFAR detection performance in homogeneous Weibull clutter," *IEEE Geosci. Remote Sens. Lett.*, vol. 16, no. 6, pp. 887–891, Jun. 2019.

[16] H. R. Alhennawi, M. M. H. E. Ayadi, M. H. Ismail, and H. A. M. Mourad, "Closed-form exact and asymptotic expressions for the symbol error rate and capacity of the H-function fading channel," *IEEE Trans. Veh. Technol.*, vol. 65, no. 4, pp. 1957–1974, Apr. 2016.

[17] E. Kreyszig, *Advanced Engineering Mathematics*, 10th ed. New Jersey, NJ, USA: John Wiley & Sons, 2010.

4 Contribution III

This chapter is a replica of the paper below:

- F. D. A. García, M. A. M. Miranda, J. C. S. Santos Filho, "New findings on GLRT radar detection of non-fluctuating targets via phased arrays," *IEEE Access*, under review, 2021.

New Findings on GLRT Radar Detection of non-fluctuating Targets via Phased Arrays

Fernando Darío Almeida García, Marco Antonio Miguel Miranda,
and José Cândido Silveira Santos Filho

Abstract

This paper addresses the standard *generalized likelihood ratio test* (GLRT) detection problem of weak signals in background noise. In so doing, we consider a *non-fluctuating* target embedded in complex white Gaussian noise (CWGN), in which the amplitude of the target echo and the noise power are assumed to be unknown. Important works have analyzed the performance for the referred scenario and proposed GLRT-based detectors. Such detectors are projected at an early stage (i.e., prior to the formation of a post-beamforming scalar waveform), thereby imposing high demands on hardware, processing, and data storage. From a hardware perspective, most radar systems fail to meet these strong requirements. In fact, due to hardware and computational constraints, most radars use a combination of analog and digital beamformers (sums) before any estimation or further pre-processing. The rationale behind this study is to derive a GLRT detector that meets the hardware and system requirements. In this work, we design and analyze a more practical and easy-to-implement GLRT detector, which is projected after the analog beamforming. The performance of the proposed detector is analyzed and the probabilities of detection (PD) and false alarm (PFA) are derived in *closed form*. An alternative fast convergent series for the PD is also derived. This series proves to be very efficient and computationally tractable, saving both computation time and computational load. Moreover, we show that in the low signal-to-noise ratio (SNR) regime, the post-beamforming GLRT detector performs better than both the classic pre-beamforming GLRT detector and the square-law detector. This finding suggests that if the signals are weak, instead of processing the signals separately, we first must to reinforce the overall signal and then assembling the system's *detection statistic*. We also showed that the PFA is independent of the number of antennas. This property allows us to maintain a certain PFA for an arbitrary number of antennas. At last, the SNR losses of all detectors are quantified.

4.1 Introduction

Before performing any task (i.e., searching, tracking or imaging), the radar must decide whether the target of interest is present or absent in a certain range, angle or

Doppler bin [1]. Unfortunately, the presence of unwanted signals such as thermal noise, clutter, and jamming, ubiquitous in practice, often render this decision very complicated. The optimal decision is achieved by applying the *likelihood ratio test* (LRT) [2]. This decision is based on the Neyman-Pearson (NP) criterion, which maximizes the probability of detection (PD) for a given probability of false alarm (PFA) [3]. The LRT provides an optimal decision if the probability density functions (PDFs) of the received samples are fully known. Of course, this requirement does not fit most practical problems. In view of this, a more general decision rule arose to deal with these types of scenarios, the so-called *generalized likelihood ratio test* (GLRT) [4]. In the GLRT, all unknown PDF parameters are replaced by their maximum likelihood estimates (MLEs). This structure allows the GLRT to work over a wide range of scenarios. Although, there is no optimality associated with the GLRT, in practice, it appears to work quite well.

Important GLRT-based detectors were derived considering phased array radars, *non-fluctuating* targets and, complex white Gaussian noise (CWGN) have been rigorously analyzed in the literature (cf. [5, 6, 7, 8, 9] for more discussion on this). These works assumed a partial or a complete lack of knowledge about the target and noise statistics. More complex detectors that rely on the use of secondary data can be found in [9, 10, 11, 12, 13, 14, 15]. In these works, secondary data was assumed to be signal-free from the target components. That is, only noise is present. In particular, in [10], it was derived the so-called Kelly's detector, which considered that the primary and secondary data vectors share the same unknown noise covariance matrix. In [13], the authors extended the analysis by considering that the target amplitude follows a Gaussian distribution.

All referred works formulate the detection problem at an early stage (i.e., prior to the formation of a post-beamforming scalar waveform), thereby imposing high demands on hardware, processing and data storage. In fact, due to hardware and computational constraints, most radars and mobile applications use a combination of analog and digital beamformers (sums) before any estimation or further pre-processing [16, 17, 18, 19]. Furthermore, since the use of GLRT involves a high degree of mathematical complexity, theoretical performance analysis can be hampered in most situations. Indeed, this was the case for the aforementioned studies in which their performance metrics – probability of detection (PD) and probability of false alarm (PFA) – were computed through numerical integration, estimated via Monte-Carlo simulations, expressed in integral-form, or require iterative solutions. In this context, we also dedicate our efforts to easy the computation of the performance metrics.

Scanning the technical literature, we realize that no study has been devoted to the development of GLRT radar detectors using a post-beamforming approach. In this paper, we design and evaluate a new GLRT-based detector which is projected after the

analog beamforming operation. Moreover, we provide the analytical tools to properly determine the performance of this detector. Specifically, we derive the PD and PFA in *closed form*. An alternative fast convergent series for the PD is also derived. For the analysis, we consider a *non-fluctuating* target embedded in CWGN, in which the amplitude of the target echo and the noise power are assumed to be unknown. The use of secondary data is not considered. From a mathematical point of view, one could envisage that our detector will somehow provide poorer performance since we are reducing the detection problem dimensionality by means of a sum operation (beamformer). In this paper, we claim that this is not always the case if the signals are weak. In fact, we show that in the low-SNR regime, the post-beamforming GLRT detector performs better than the classic GLRT detector (called here as pre-beamforming GLRT detector) [7, Eq. (6.20)] and than the square-law detector [20, Eq. (15.57)], widely used in non-coherent radars [21, 22, 23]. This assertion suggest that, instead of processing the signals separately, it is better to adding them up before building the system's *detection statistic*. Other attractive features about our detector will be discussed throughout this work.

The key contributions of this work may now be summarized as follows:

1. Firstly, we design and evaluate a new GLRT detector projected after the analog beamforming operation. From the practical point of view, this detector meets the hardware and systems requirements of most radar systems.

2. Secondly, we obtain *closed-form* expressions for the corresponding PD and PFA. In particular, the PD is given in terms of the bivariate Fox H-function, for which we also provide a portable and efficient MATHEMATICA routine.

3. Thirdly, we derive an alternative series representation for the PD, obtained by exploring the orthogonal selection of poles in the Cauchy's residue theorem. This series enjoys a low computational burden and can be quickly executed in any ordinary desktop computer.[1]

4. Finally, we provide some insightful and concluding remarks on the GLRT-based detection for *non-fluctuating* targets. To do so, we compare the performance of our derived detector with the pre-beamforming GLRT detector.

In what follows, $f_{(\cdot)}(\cdot)$ denotes PDF; $(\cdot)^T$, transposition; $|\cdot|$, modulus; $\mathbf{Re}\left[\cdot\right]$, real argument; $\mathbf{Im}\left[\cdot\right]$, imaginary argument; $\|\cdot\|$, Euclidean norm; $\mathbb{E}\left[\cdot\right]$, expectation; $\mathbb{COV}\left[\cdot\right]$, covariance; rank$(\cdot)$, rank of a matrix; and $(\cdot)^{-1}$, matrix inversion.

[1] Section 4.6 illustrates the efficiency of this series and compares it with MATHEMATICA's built-in numerical integration.

4.2 Receiver's Front–End: Phased Array

In this work, we consider a linear phased array radar composed of N antennas equally separated in the azimuth direction, as shown in Fig. 4.1. The transmission and reception processes are carried out as follows. A single antenna transmits a linear frequency-modulated pulse, whereas all antennas receive the echo signals. Furthermore, an amplification block and a phased shifter are installed after each antenna element, and all outputs are added together (i.e., the analog beamforming operation is applied).

Thus, the in-phase and quadrature signals can be written in matrix form, respectively, as

$$\mathbf{X} \triangleq \begin{pmatrix} X_{1,1} & X_{2,1} & \cdots & X_{N,1} \\ X_{1,2} & X_{2,2} & \cdots & X_{N,2} \\ \vdots & \vdots & \ddots & \vdots \\ X_{1,M} & X_{2,M} & \cdots & X_{N,M} \end{pmatrix} \tag{4.1}$$

$$\mathbf{Y} \triangleq \begin{pmatrix} Y_{1,1} & Y_{2,1} & \cdots & Y_{N,1} \\ Y_{1,2} & Y_{2,2} & \cdots & Y_{N,2} \\ \vdots & \vdots & \ddots & \vdots \\ Y_{1,M} & Y_{2,M} & \cdots & Y_{N,M} \end{pmatrix}, \tag{4.2}$$

where $X_{n,m}$ and $Y_{n,m}$ represent the in-phase and quadrature received signals, respectively. In addition, $m \in \{1, 2, \ldots, M\}$ is a discrete-time index, and $n \in \{1, 2, \ldots, N\}$ is a spacial index that denotes the association to the n-th antenna.

For simplicity and without loss of generality, we assume a unity gain and a null phase shift for all antenna elements. In addition, we consider a collection of M signal samples for each of the N antennas. Then, the overall received signal can be written, in vector form, as

$$\underline{R} = [R_1, R_2, \cdots, R_M]^T, \tag{4.3}$$

where

$$R_m = \sum_{n=1}^{N} (X_{n,m} + jY_{n,m}). \tag{4.4}$$

Note that $\underline{R}$ is a complex-valued random vector, in which each component is formed by the sum of the received signals coming from all the antennas at a certain time.

As will be shown in Section 4.3, the fact of adding the target echoes will drastically change the hardware design, *detection statistic*, and performance of the post-beamforming GLRT detector compared to previous detectors (cf. [7, 9, 10, 12, 13]). Since our detector is projected after the analog beamforming operation, one could argue that its performance would be somehow suboptimum, as compared to the pre-beamforming

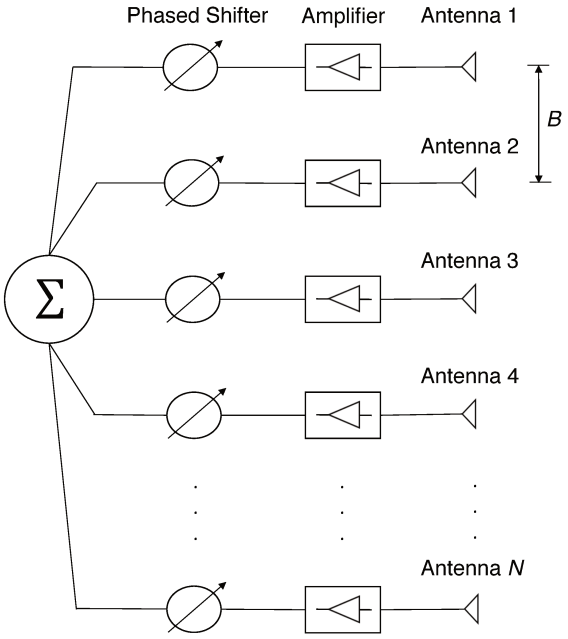

Figure 4.1 – Top view of the phased array radar

GLRT detector. In this work, we show that this conclusion not always holds. Indeed, for some cases the post-beamforming GLRT detector overcomes the pre-beamforming GLRT detector. This assertion heavily relies on the SNR of the incoming signals.

4.3 Detection Design Via Post–Beamforming GLRT

In this section, we present the detection scheme for the post-beamforming GLRT detector.

Herein, the presence of absence of the target is posed over the following *binary hypothesis test*.[2]

4.3.1 Hypothesis Test

- Hypothesis $\mathcal{H}_0$: target is absent. In this case, from the radar model described in the previous section, each $X_{n,m}$ and $Y_{n,m}$ are formed by mutually independent Gaussian components with zero mean and unknown variance σ^2. (Due to the presence of CWGN alone.)

- Hypothesis $\mathcal{H}_1$: target is present. In this case, each $X_{n,m}$ and $Y_{n,m}$ are formed by mutually independent Gaussian components with unknown non-zero means and unknown variance σ^2. (Due to the *non-fluctuating* target and noise.)

[2] A *binary hypothesis test* refers to the choice that a radar makes between two hypotheses: signal plus interference or only interference. This choice is made throughout all resolution cells [24].

According to the stochastic model described in Section 4.2, the PDFs of $\underline{R}$ under $\mathcal{H}_0$ and $\mathcal{H}_1$ are given, respectively, by

$$f_{\underline{R}}\left(\underline{r}|\sigma^2;\mathcal{H}_0\right) = \frac{1}{\left(2\pi\sigma^2 N\right)^M}\exp\left[-\frac{\sum_{m=1}^{M}|r_m|^2}{2\sigma^2 N}\right] \tag{4.5}$$

$$f_{\underline{R}}\left(\underline{r}|\sigma^2;\mu_X;\mu_Y;\mathcal{H}_1\right) = \frac{1}{\left(2\pi\sigma^2 N\right)^M}\exp\left[-\frac{\sum_{m=1}^{M}\left\{\left(\mathbf{Re}\left[r_m\right]-\mu_X\right)^2+\left(\mathbf{Im}\left[r_m\right]-\mu_Y\right)^2\right\}}{2\sigma^2 N}\right] \tag{4.6}$$

where $\mu_X = \sum_{n=1}^{N}\mu_{X,n}$ and $\mu_Y = \sum_{n=1}^{N}\mu_{Y,n}$ represent the total sum of target echoes for the in-phase and quadrature components, respectively. Note that after the analog beamforming operation, we no longer have access to the specific value of target echo received by a particular antenna, which is what actually occurs in practice.

4.3.2 Detection Rule

The system's *detection statistic* can be defined through GLRT as [7]

$$\frac{f_{\underline{R}}\left(\underline{r}|\hat{\sigma}_1^2;\hat{\mu}_X;\hat{\mu}_Y;\mathcal{H}_1\right)}{f_{\underline{R}}\left(\underline{r}|\hat{\sigma}_0^2;\mathcal{H}_0\right)} \underset{\mathcal{H}_0}{\overset{\mathcal{H}_1}{\gtrless}} T, \tag{4.7}$$

where T is an arbitrary threshold and the ratio on the left-hand side of (4.7) is called the generalized likelihood ratio. In addition, $\hat{\sigma}_0^2$ is the MLE for σ^2, to be obtained from (4.5), and $\hat{\sigma}_1^2$, $\hat{\mu}_X$ and $\hat{\mu}_Y$ are the MLEs for σ^2, μ_X and μ_Y, respectively, to be obtained from (4.6). Eq.(4.7) implies that the system will decide for $\mathcal{H}_1$ whenever the generalized likelihood ratio exceeds the threshold T, and will decide for $\mathcal{H}_0$ otherwise. Since the logarithmic function is a monotonically increasing function, we can rewrite the GLRT as

$$\ln\left[\frac{f_{\underline{R}}\left(\underline{r}|\hat{\sigma}_1^2;\hat{\mu}_X;\hat{\mu}_Y;\mathcal{H}_1\right)}{f_{\underline{R}}\left(\underline{r}|\hat{\sigma}_0^2;\mathcal{H}_0\right)}\right] \underset{\mathcal{H}_0}{\overset{\mathcal{H}_1}{\gtrless}} \ln\left[T\right]. \tag{4.8}$$

Note in (4.5) and (4.6) that all unknown parameters (σ^2, μ_X and μ_Y) are scalars quantities. Hence, the corresponding MLEs can be obtained easily. For example, $\hat{\sigma}_0^2$ can be found by taking the natural logarithm of (4.5), and then taking the derivative with respect to σ^2, i.e.,

$$\frac{\partial \ln\left[f_{\underline{R}}\left(\underline{r}|\sigma^2;\mathcal{H}_0\right)\right]}{\partial\sigma^2} = -\frac{M}{\sigma^2}+\frac{1}{2N\sigma^4}\sum_{m=1}^{M}|r_m|^2. \tag{4.9}$$

Then, we set (4.9) equal to zero and solve the equation for σ^2, which yields to

$$\hat{\sigma_0}^2 = \frac{1}{2MN}\sum_{m=1}^{M}|r_m|^2. \tag{4.10}$$

Using (4.6) and following the same approach as in (4.10), the MLEs for μ_X and μ_Y can be calculated, respectively, as

$$\hat{\mu}_X = \frac{1}{M} \sum_{m=1}^{M} \mathbf{Re}\left[r_m\right] \tag{4.11}$$

$$\hat{\mu}_Y = \frac{1}{M} \sum_{m=1}^{M} \mathbf{Im}\left[r_m\right], \tag{4.12}$$

whereas the MLE for σ^2 can be computed as follows:

$$\hat{\sigma_1}^2 = \frac{1}{2NM} \sum_{m=1}^{M} \left\{ \left(\mathbf{Re}\left[r_m\right] - \hat{\mu}_X\right)^2 + \left(\mathbf{Im}\left[r_m\right] - \hat{\mu}_Y\right)^2 \right\}. \tag{4.13}$$

(For brevity, we have omitted the derivation steps.)

Substituting (4.10)–(4.13) in (4.8) and after simple simplifications, we have

$$M \ln\left[\left(\frac{\hat{\sigma_0}^2}{\hat{\sigma_1}^2}\right)\right] \underset{\mathcal{H}_0}{\overset{\mathcal{H}_1}{\gtrless}} \ln\left[T\right]. \tag{4.14}$$

Expanding (4.13) and after performing some minor manipulations, we can rewrite $\hat{\sigma_1}^2$ as

$$\begin{aligned}
\hat{\sigma_1}^2 &= \frac{1}{2MN} \sum_{m=1}^{M} \left\{ \hat{\mu}_X^2 + \hat{\mu}_Y^2 \right\} \\
&\quad + \underbrace{\frac{1}{2MN} \sum_{m=1}^{M} \left\{ \left(\mathbf{Re}\left[r_m\right]\right)^2 + \left(\mathbf{Im}\left[r_m\right]\right)^2 \right\}}_{\hat{\sigma_0}^2} \\
&\quad + \left(\frac{\hat{\mu}_X}{N}\right) \underbrace{\frac{1}{M} \sum_{m=1}^{M} \mathbf{Re}\left[r_m\right]}_{\hat{\mu}_X} + \left(\frac{\hat{\mu}_Y}{N}\right) \underbrace{\frac{1}{M} \sum_{m=1}^{M} \mathbf{Im}\left[r_m\right]}_{\hat{\mu}_Y} \\
&\overset{(a)}{=} \hat{\sigma_0}^2 - \frac{1}{2N} \left(\hat{\mu}_X^2 + \hat{\mu}_Y^2 \right),
\end{aligned} \tag{4.15}$$

where in step (a) we have used (4.10), (4.11), and (4.12), along with some simplifications.

Isolating $\hat{\sigma}_0^2$ from (4.15), we obtain

$$\hat{\sigma}_0^2 = \hat{\sigma}_1^2 + \frac{1}{2N} \left(\hat{\mu}_X^2 + \hat{\mu}_Y^2 \right). \tag{4.16}$$

Replacing (4.16) in (4.14), yields

$$M \ln\left[1 + \frac{(\hat{\mu}_X^2 + \hat{\mu}_Y^2)}{2N\hat{\sigma_1}^2}\right] \underset{\mathcal{H}_0}{\overset{\mathcal{H}_1}{\gtrless}} \ln\left[T\right]. \tag{4.17}$$

Now, since M and N are a positive numbers, we obtain the same decision as in (4.17) by simply comparing $\left(\hat{\mu}_X^2 + \hat{\mu}_Y^2\right)/\hat{\sigma}_1^2$ with a modified threshold, γ', that is,

$$\frac{\hat{\mu}_X^2 + \hat{\mu}_Y^2}{\hat{\sigma_1}^2} \underset{\mathcal{H}_0}{\overset{\mathcal{H}_1}{\gtrless}} \gamma'. \tag{4.18}$$

For convenience and without loss of generality, we define an equivalent decision rule as[3]

$$Z \triangleq \Psi\left(\frac{\hat{\mu}_X^2 + \hat{\mu}_Y^2}{\hat{\sigma_1}^2}\right) \underset{\mathcal{H}_0}{\overset{\mathcal{H}_1}{\gtrless}} \gamma, \tag{4.19}$$

where Z is the system's *detection statistic*, $\Psi = (M-1)/2N$ is a positive constant, and γ is a new modified threshold.

Fig. 4.2 illustrates how the pre-beamforming GLRT, the post-beamforming GLRT, and the square-law detectors are constructed. More specifically, Fig. 4.2-(a) depicts the pre-beamforming GLRT detector architecture. In this case, all received signals are processed separately to form the system's *detection statistic* [7]. Certainly, this type of processing is more difficult to implement due to hardware constraints.

Fig. 4.2-(b) illustrates the post-beamforming GLRT detector architecture. This detector provides a less restrictive hardware implementation, as well as a simpler *detection statistic* that results from adding the received signals. Finally, Fig. 4.2-(c) illustrates the square-law detector architecture. Here, after the analog beamforming, the square magnitude of the signal samples is taken and then they are added up together. It is important to emphasize that in order to analytically calculate the performance metrics of the square law detector, we do need the information about the noise power. That is, for a given PFA, the detection threshold is given as a function of the noise power [20].

4.4 Detection Performance

In this section, we characterize and analyze the performance of the post-beamforming GLRT detector. To do so, we start finding the PDFs of Z under $\mathcal{H}_0$ and $\mathcal{H}_1$.

[3] The constant Ψ was introduced in the decision rule because it allow us to model Z as a random variable with known PDF, as will become apparent soon.

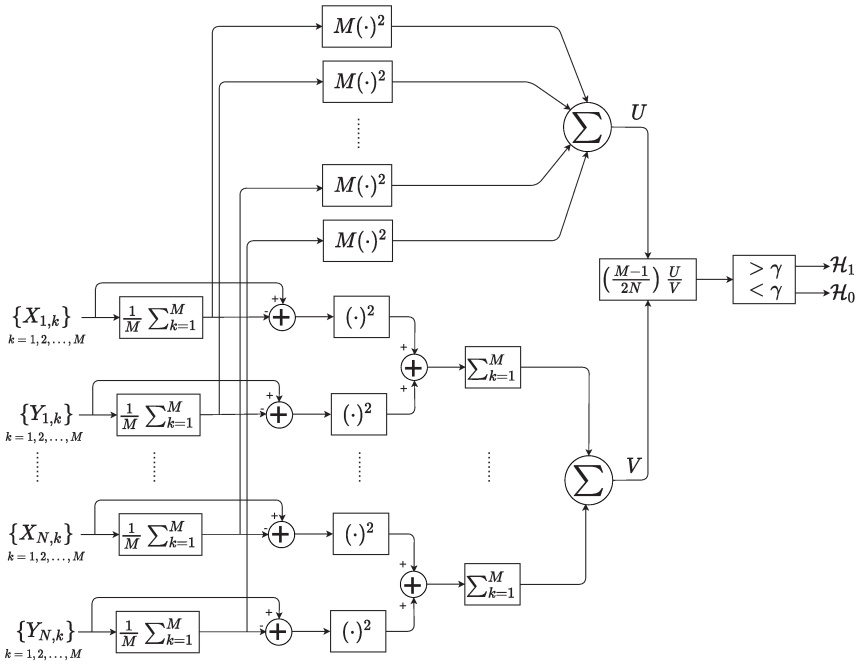

(a) Pre-beamforming GLRT detector [7].

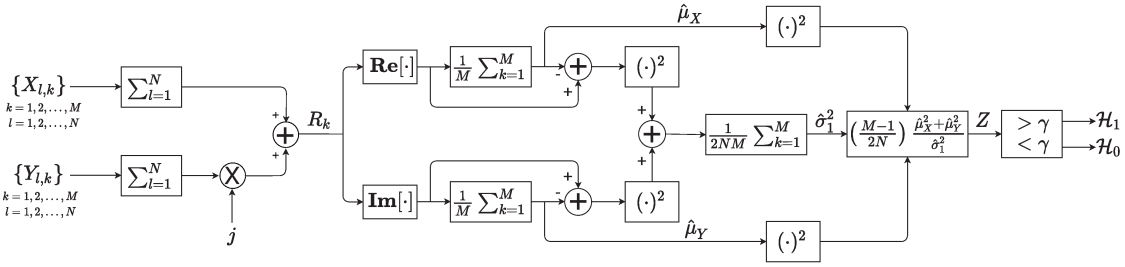

(b) Post-beamforming GLRT detector.

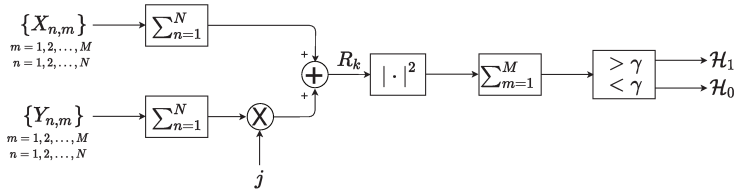

(c) Square-law detector [20].

Figure 4.2 – Detection Schemes.

4.4.1 Detection Statistics

First, we rewrite (4.19) as follows:

$$Z = \frac{(M-1)\left(\hat{\mu}_X^2 + \hat{\mu}_Y^2\right)}{2N{\hat{\sigma}_1}^2} \overset{(a)}{=} (M-1)\frac{\overbrace{\left(\hat{\mu}_X^2 + \hat{\mu}_Y^2\right) M/N\sigma^2}^{\triangleq\, \mathcal{I}_1}}{\underbrace{2{\hat{\sigma}_1}^2 M/\sigma^2}_{\triangleq\, \mathcal{I}_2}}, \tag{4.20}$$

where in step (a), without affecting the detection performance, we have multiplied the left-hand side of Z by $M\sigma^2/M\sigma^2$.

Note that, to fully characterize Z, it is imperative to find the PDFs of $\mathcal{I}_1$ and $\mathcal{I}_2$ under $\mathcal{H}_0$ and $\mathcal{H}_1$.

Substituting (4.11) and (4.12) in $\mathcal{I}_1$, yields to

$$\mathcal{I}_1 = \underbrace{\left(\frac{1}{\sqrt{MN}\sigma}\sum_{k=1}^{M}\mathbf{Re}\left[r_k\right]\right)^2}_{\triangleq\, U} + \underbrace{\left(\frac{1}{\sqrt{MN}\sigma}\sum_{k=1}^{M}\mathbf{Im}\left[r_k\right]\right)^2}_{\triangleq\, V}. \tag{4.21}$$

Observe that U is the square of a Gaussian random variable (RV) with mean $\sqrt{M}\mathbb{E}\left[X_{l,k}\right]/\sigma\sqrt{N}$ and unit variance. In a similar way, V is the square of a Gaussian RV with mean $\sqrt{M}\mathbb{E}\left[Y_{l,k}\right]/\sigma\sqrt{N}$ and unit variance. Therefore, depending on the hypothesis, $\mathcal{I}_1$ can match one of the following conditions:

1. Given $\mathcal{H}_0$: $\mathcal{I}_1$ follows a central chi-squared (CCS) distribution [25] with $\nu_1 = 2$ degrees of freedom.

2. Given $\mathcal{H}_1$: $\mathcal{I}_1$ follows a noncentral chi-squared (NCCS) distribution [26] with non-central parameter $\lambda_1 = M\left(\mu_X^2 + \mu_Y^2\right)/N\sigma^2$ and $\alpha_1 = 2$ degrees of freedom.

Inserting (4.13) in $\mathcal{I}_2$, we obtain

$$\mathcal{I}_2 = \frac{1}{N\sigma^2}\sum_{m=1}^{M}\left\{\left(\mathbf{Re}\left[r_m\right] - \hat{\mu}_X\right)^2 + \left(\mathbf{Im}\left[r_m\right] - \hat{\mu}_Y\right)^2\right\} \tag{4.22}$$

Here, the analysis is a bit more cumbersome; therefore, we establish the following two lemmas:

Lemma 1: $\mathcal{I}_2$ matches the following conditions:

1. Given $\mathcal{H}_0$: $\mathcal{I}_2$ follows a CCS distribution with $\nu_2 = 2(M-1)$ degrees of freedom.

2. Given $\mathcal{H}_1$: $\mathcal{I}_2$ also follows a CCS distribution with $2(M-1)$ degrees of freedom. In this case, for convenience, we model $\mathcal{I}_2$ by a NCCS distribution with noncentral parameter $\lambda_2 = 0$ and $\alpha_2 = 2(M-1)$ degrees of freedom.

Proof: See Appendix B.1. ■

Lemma 2: $\mathcal{I}_1$ and $\mathcal{I}_2$ are mutually independent RVs.

Proof: See Appendix B.2. ■

Then, using Lemmas 1 and 2, we can define $\mathcal{I}_1/\mathcal{I}_2$ as the ratio of either two independent CCS RVs or two independent NCCS RVs, depending on the hypothesis. The factor $(M-1)$ in (4.20) allows us to model Z by a RV with known PDF.

Given $\mathcal{H}_0$, it can be shown that Z follows a central F-distribution [27] with PDF given by

$$f_Z\left(z|\mathcal{H}_0\right) = \frac{(M-1)^{M-1}(M+z-1)^{-M}}{B(1,M-1)}, \tag{4.23}$$

where $B(\cdot,\cdot)$ is the Beta function [28, Eq. (5.12.3)]. Using [28, Eq. (5.12.1)], we can rewrite (4.23) in compact form as

$$f_Z\left(z|\mathcal{H}_0\right) = \left(\frac{M-1}{M+z-1}\right)^M. \tag{4.24}$$

For the case of $\mathcal{H}_1$, Z can be modeled by a doubly noncentral F-distribution [29], with PDF given by

$$f_Z\left(z|\mathcal{H}_1\right) = \exp\left[-\Upsilon\ M\right]\left(\frac{M-1}{M+z-1}\right)^M\ {}_1F_1\left(M;1;\frac{\Upsilon\ z\ M}{M+z-1}\right), \tag{4.25}$$

where $\Upsilon = (\mu_X^2+\mu_Y^2)/2N\sigma^2$, and ${}_1F_1\left(\cdot;\cdot;\cdot\right)$ is the Kummer confluent hypergeometric function [28, Eq. (13.1.2)]. The equality $\Upsilon = N\ \mathrm{SNR}_n$ holds if $\mathrm{SNR}_n = \mathrm{SNR}_p\ \forall\ (n,p)$, with $\mathrm{SNR}_n = \left(\mu_{X,n}^2+\mu_{Y,n}^2\right)/2\sigma^2$ being the signal-to-noise ratio present at the n-th antenna. The derivation of (4.25) is shown in Appendix B.3.

4.4.2 False Alarm and Detection Probabilities

It is well known that the performance of any radar system is governed by the PFA and PD. These probabilities can be computed, respectively, as [24]

$$P_{\mathrm{FA}} \triangleq \int_\gamma^\infty f_Z\left(z|\mathcal{H}_0\right)\,\mathrm{d}z \tag{4.26}$$

$$P_{\mathrm{D}} \triangleq \int_\gamma^\infty f_Z\left(z|\mathcal{H}_1\right)\,\mathrm{d}z. \tag{4.27}$$

Replacing (4.24) in (4.26), yields

$$P_{\mathrm{FA}} = \left(\frac{M-1}{\gamma + M - 1}\right)^{M-1}. \tag{4.28}$$

Now, isolating γ from (4.28) we can find a threshold so as to meet a desired PFA, i.e.,

$$\gamma = 1 - M + (M-1)\, {P_{\mathrm{FA}}}^{1/(1-M)}. \tag{4.29}$$

It can be noticed in (4.29) that we do not need the knowledge of the noise power nor the number of antennas to set the detection threshold. That is, the detection threshold γ is independent of both σ^2 and N. This important feature will allow us to maintain a certain PFA for an arbitrary number of antennas. More precisely, with objective of increasing the PD, we can increase N without worrying about the increase in the PFA.

On the other hand, after substituting (4.25) in (4.27), the PD can be obtained in single-integral form as

$$P_{\mathrm{D}} = \exp\left[-\Upsilon\ M\right] \int_{\gamma}^{\infty} \left(\frac{M-1}{M+z-1}\right)^{M} {}_1F_1\left(M; 1; \frac{\Upsilon\ z\ M}{M+z-1}\right) \mathrm{d}z. \tag{4.30}$$

Certainly, (4.30) can be evaluated by means of numerical integration. Nonetheless, to further facilitate the computation of the PD, we provide alternative, faster, and more tractable solutions. This is attained in the next section.

4.5 Alternative Expressions for the Probability of Detection

In this section, we provide both a closed-form solution and a fast convergent series for the PD, To this end, we make use complex analysis and a thorough calculus of residues.

4.5.1 Fox's H-Function-Based Representation

Here, we obtain an alternative closed-form solution for (4.30), expressed in terms of the Fox H-function.

To do so, we first perform some mathematical manipulations in (4.30), resulting in

$$P_{\mathrm{D}} = \frac{\exp\left[-\Upsilon\ M\right](M-1)^{M}}{\Gamma(M)} \int_{\gamma}^{\infty} \left(\frac{1}{M+z-1}\right)^{M} G_{1,2}^{1,1}\left[\begin{array}{c|c} 1-M & \\ 0,0 & -\dfrac{\Upsilon\ z\ M}{M+z-1} \end{array}\right] \mathrm{d}z, \tag{4.31}$$

where $G_{m,n}^{p,q}\left[\cdot\right]$ is the Meijer's G-function [30, Eq. (8.2.1.1)].

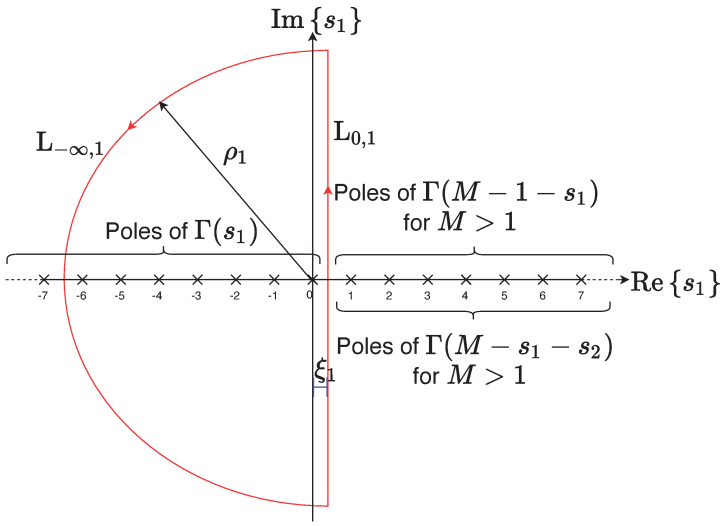

Figure 4.3 – Integration path for $\mathcal{L}_{\mathbf{s},1}$.

Now, using the contour integral representation of the Meijer's G-function, we can express (4.31) as follows:

$$P_{\mathrm{D}} = \frac{\exp\left[-\Upsilon\ M\right](M-1)^{M}}{\Gamma(M)} \int_{\gamma}^{\infty} \left(\frac{1}{M+z-1}\right)^{M} \left(\frac{1}{2\pi j}\right) \oint_{\mathcal{L}^{**}_{\mathbf{s},1}} \frac{\Gamma(s_1)\Gamma(M-s_1)}{\Gamma(1-s_1)} \times \left(-\frac{\Upsilon\ z\ M}{M+z-1}\right)^{-s_1} \mathrm{d}s_1\ \mathrm{d}z, \tag{4.32}$$

in which $\mathcal{L}^{**}_{\mathbf{s},1}$ is a closed complex contour that separates the poles of the gamma function $\Gamma(s_1)$ from the poles of $\Gamma(M-s_1)$. Since $\int_{\gamma}^{\infty} |f_Z(z|\mathcal{H}_1)|\,\mathrm{d}z < \infty$, we can interchange the order of integration[31], i.e.,

$$P_{\mathrm{D}} = \frac{\exp\left[-\Upsilon\ M\right](M-1)^{M}}{\Gamma(M)} \left(\frac{1}{2\pi j}\right) \oint_{\mathcal{L}^{**}_{\mathbf{s},1}} \frac{\Gamma(s_1)\Gamma(M-s_1)\left(-\Upsilon\ M\right)^{-s_1}}{\Gamma(1-s_1)} \times \int_{\gamma}^{\infty} \left(\frac{1}{M+z-1}\right)^{M} \left(\frac{z}{M+z-1}\right)^{-s_1} \mathrm{d}z\ \mathrm{d}s_1. \tag{4.33}$$

Developing the inner real integral, we obtain

$$P_{\mathrm{D}} = \frac{\exp\left[-\Upsilon\ M\right](M-1)^{M}\Gamma(M-1)}{\Gamma(M)\ \gamma^{M-1}} \left(\frac{1}{2\pi j}\right) \oint_{\mathcal{L}^{*}_{\mathbf{s},1}} \frac{\Gamma(s_1)\Gamma(M-s_1)\left(-\Upsilon\ M\right)^{-s_1}}{\Gamma(1-s_1)} \times\ {}_2\tilde{F}_1\left(M-1, M-s_1; M; \frac{1-M}{\gamma}\right) \mathrm{d}s_1, \tag{4.34}$$

where ${}_2\tilde{F}_1(a,b;c;x) = {}_2F_1(a,b;c;x)/\Gamma(c)$ is the regularized Gauss hypergeometric function, and ${}_2F_1(\cdot,\cdot;\cdot;\cdot)$ is the Gauss hypergeometric function [28, Eq. (15.1.1)]. Note that we have used a new complex contour, $\mathcal{L}^{*}_{\mathbf{s},1}$. This is because the inner integration changed the integration path in the complex plane. Here, $\mathcal{L}^{*}_{\mathbf{s},1}$ is a closed contour that separates the poles of $\Gamma(s_1)$ from those of $\Gamma(M-s_1)$.

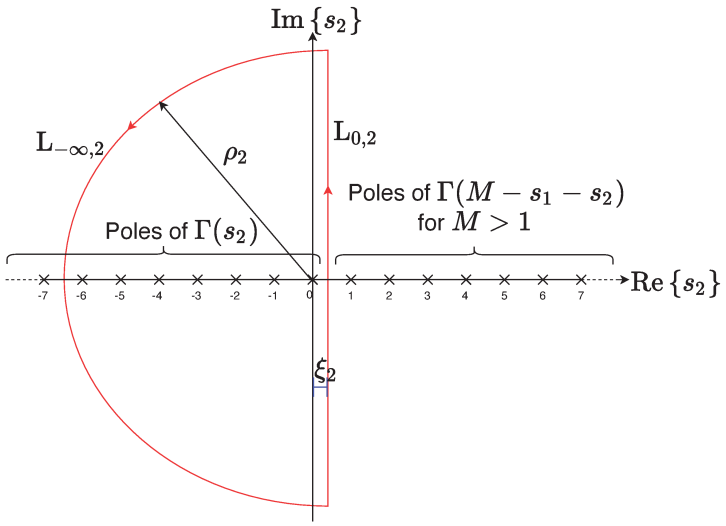

Figure 4.4 – Integration path for $\mathcal{L}_{\mathbf{s},2}$.

Finally, replacing (4.29) in (4.34) and after using the complex integral representation of the regularized Gauss hypergeometric function [32, Eq. (07.24.26.0004.01)], we can express PD in closed form as

$$P_{\mathrm{D}} = \Phi\ \mathbf{H}\left[[\Omega, -\Upsilon\ M]\,; [0, 0, M-1, M]\,, \begin{pmatrix} 1 & 0 & -1 & -1 \\ 0 & 1 & 0 & -1 \end{pmatrix}^{T}; [M, 1]\,, \begin{pmatrix} -1 & 0 \\ 0 & -1 \end{pmatrix}; \mathcal{L}_{\mathbf{s}}\right] \tag{4.35}$$

where $\mathcal{L}_{\mathbf{s}} = \mathcal{L}_{\mathbf{s}_1} \times \mathcal{L}_{\mathbf{s}_2}$, and

$$\Phi = \frac{\Omega^{M-1} \exp\left[-\Upsilon\ M\right]}{\Gamma(M-1)} \tag{4.36}$$

$$\Omega = \frac{M-1}{1 - M + (M-1)\, {P_{\mathrm{FA}}}^{1/(1-M)}}. \tag{4.37}$$

Observe that (4.35) has two new closed contours, $\mathcal{L}_{\mathbf{s},1}$ and $\mathcal{L}_{\mathbf{s},2}$. $\mathcal{L}_{\mathbf{s},1}$ is an adjusted contour that appears due to the presence of the new gamma functions, whereas $\mathcal{L}_{\mathbf{s},2}$ is the contour corresponding to the complex representation of the regularized Gauss hypergeometric function. The integration paths for $\mathcal{L}_{\mathbf{s},1}$ and $\mathcal{L}_{\mathbf{s},2}$ are described in Section 4.6.

A general implementation for the multivariate Fox H-function is not yet available in mathematical packages such as MATHEMATICA, MATLAB, or MAPLE. Some works have been done to alleviate this problem [33, 34, 35]. Specifically in [33], the Fox H-function was implemented from one up to four variables. In this work, we provide an accurate and portable implementation in MATHEMATICA for the bivariate Fox H-function. The code used to compute (4.35) is presented in Appendix C.1. It is important to mention that such implementation is specific for our system model. Moreover, an equivalent series representation for (4.35) is also provided to facilitate the use of our results. This series representation is presented in the subsequent subsection.

4.5.2 Infinite-Series Representation

Here, we provide a series representation for (4.35). To achieve this, we exploit the orthogonal selection of poles in Cauchy's residue theorem.

First, let us consider the following suitable closed contours for (4.35): (i) $\mathcal{L}_{\mathbf{s},1} = \mathrm{L}_{0,1} + \mathrm{L}_{-\infty,1}$, and (ii) $\mathcal{L}_{\mathbf{s},2} = \mathrm{L}_{0,2} + \mathrm{L}_{-\infty,2}$. Both contours are shown in Figs. 4.3 and 4.4, where $\xi_1 \in \mathbb{R}^+$ must be chosen so that all the poles of $\Gamma(s_1)$ are separated from those of $\Gamma(M-1-s_1)$ and $\Gamma(M-s_1-s_2)$, and $\xi_2 \in \mathbb{R}^+$ must be chosen so that all the poles of $\Gamma(s_2)$ are separated from those of $\Gamma(M-s_1-s_2)$. Additionally, ρ_1 and ρ_2 are the radius of the arcs $\mathrm{L}_{-\infty,1}$ and $\mathrm{L}_{-\infty,2}$, respectively.

It is easy to prove that any complex integration along the paths $\mathrm{L}_{-\infty,1}$ and $\mathrm{L}_{-\infty,2}$ will be zero as ρ_1 and ρ_2 go to infinity, respectively. (ρ_1 and ρ_2 tend to infinity since the gamma functions $\Gamma(s_1)$ and $\Gamma(s_2)$ generate simple poles at all non-positive integers [28, Eq. (5.2.1)].) Therefore, the final integration path for $\mathcal{L}_{\mathbf{s},1}$ starts at $\xi_1 - j\infty$ and goes to $\xi_1 + j\infty$, whereas the final integration path for $\mathcal{L}_{\mathbf{s},2}$ starts at $\xi_2 - j\infty$ and goes to $\xi_2 + j\infty$.

Now, we can rewrite (4.35) through the sum of residues as [36]

$$P_{\mathrm{D}} = \Phi \sum_{k=0}^{\infty} \sum_{l=0}^{\infty} \mathrm{Res}\left[\Xi\left(s_1, s_2\right); s_1 = -k, s_2 = -l\right], \tag{4.38}$$

where $\mathrm{Res}\left[\Xi\left(s_1, s_2\right); s_1 - k, s_2 = -l\right]$ represents the residue of $\Xi\left(s_1, s_2\right)$ at the poles $s_1 = -k$, $s_2 = -l$, and

$$\Xi\left(s_1, s_2\right) = \frac{\Gamma(s_1)\Gamma(s_2)\Gamma(M-s_1-1)\Gamma(-s_1+M-s_2)\Omega^{-s_1}\left(-\Upsilon\ M\right)^{-s_2}}{\Gamma(1-s_2)\Gamma(-(s_1-M))}. \tag{4.39}$$

is the integration kernel of (4.35).

Accordingly, after applying the residue operation [36, Eq. (16.3.5)], (4.38) reduces to

$$P_{\mathrm{D}} = \Phi \sum_{k=0}^{\infty} \sum_{l=0}^{\infty} \frac{\Gamma(k+M-1)\Gamma(k+l+M)\left(-\Omega\right)^{k}\left(\Upsilon\ M\right)^{l}}{k!\Gamma(l+1)^2\Gamma(k+M)}. \tag{4.40}$$

Finally, with the aid of [28, Eq. (15.2.1)] and after some mathematical manipulations, we obtain

$$P_{\mathrm{D}} = \exp\left[-\Upsilon\ M\right]\Omega^{M-1} \sum_{k=0}^{\infty} \frac{\Gamma(k+M)\left(\Upsilon\ M\right)^{k}\ {}_2\tilde{F}_1\left(M-1, k+M; M; -\Omega\right)}{\Gamma(k+1)^2}. \tag{4.41}$$

It is worth mentioning that (4.41) is also an original contribution of this work, proving to be very efficient and computationally tractable, as will be shown in the next section.

Generally, when radar designers need to compute the PD over a certain volume (i.e., range, azimuth and elevation), the calculation of the PD has to be performed for all

Table 4.1 – Test cases.

Case	P_{D} Parameters	P_{D} Value
1	$M = 50$, $P_{FA} = 10^{-8}$, $\Upsilon = -10$ dB	0.106 %
2	$M = 80$, $P_{FA} = 10^{-8}$, $\Upsilon = -10$ dB	1.416 %
3	$M = 100$, $P_{FA} = 10^{-8}$, $\Upsilon = -10$ dB	4.423 %
4	$M = 50$, $P_{FA} = 10^{-8}$, $\Upsilon = -5$ dB	19.224 %
5	$M = 50$, $P_{FA} = 10^{-6}$, $\Upsilon = -5$ dB	52.886 %
6	$M = 50$, $P_{FA} = 10^{-4}$, $\Upsilon = -5$ dB	87.958 %
7	$M = 50$, $P_{FA} = 10^{-6}$, $\Upsilon = -3$ dB	92.089 %
8	$M = 50$, $P_{FA} = 10^{-6}$, $\Upsilon = -2$ dB	98.621 %
9	$M = 50$, $P_{FA} = 10^{-6}$, $\Upsilon = -1$ dB	99.902 %

the point scatterers within the entire coverage volume, thus increasing the computational load and simulation time. Eq. (4.41) can be executed quickly on an ordinary desktop computer, serving as a useful tool for radar designers.

Moreover, if $\mathcal{T}_0 - 1$ terms are used in (4.41), we can define the truncation error as

$$\mathcal{T} = \frac{1}{\Gamma(M)} \sum_{k=T_0}^{\infty} \frac{\Omega^{M-1} \exp\left[-M\Upsilon\right] (M\Upsilon)^k \Gamma(k+M)\, {}_2F_1(M-1, k+M; M; \Omega)}{\Gamma(k+1)^2}. \tag{4.42}$$

Since the Gauss hypergeometric function in (19) is monotonically decreasing with respect to k, $\mathcal{T}$ can be bounded as

$$\mathcal{T} \leq {}_2F_1\left(M-1, M+T_0; M; \Omega\right) \sum_{k=T_0}^{\infty} \frac{\Omega^{M-1} \exp\left[-M\Upsilon\right] (M\Upsilon)^k \Gamma(k+M)}{\Gamma(k+1)^2 \Gamma(M)}. \tag{4.43}$$

Since we add up strictly positive terms, we have

$$\begin{aligned} \sum_{k=T_0}^{\infty} \frac{\Omega^{M-1} \exp\left[-M\Upsilon\right] (M\Upsilon)^k \Gamma(k+M)}{\Gamma(k+1)^2 \Gamma(M)} &\leq \sum_{k=0}^{\infty} \frac{\Omega^{M-1} \exp\left[-M\Upsilon\right] (M\Upsilon)^k \Gamma(k+M)}{\Gamma(k+1)^2 \Gamma(M)} \\ &\overset{(a)}{=} \Omega^{M-1} L_{M-1}(-M\Upsilon), \end{aligned} \tag{4.44}$$

where in step (a), we have used [32, Eq. (05.02.02.0001.01)] and some minor simplifications. Then, from (4.43) and (4.44), (4.42) can be bounded as

$$\mathcal{T} \leq \frac{L_{M-1}(-M\Upsilon)\, {}_2F_1\left(M-1, M+T_0; M; -\Omega\right)}{\Omega^{1-M}}, \tag{4.45}$$

where $L_{(\cdot)}(\cdot)$ is the Laguerre polynomial [32, Eq. (05.02.02.0001.01)].

4.6 Numerical Results and Discussions

In this section, we validate our derived expressions and discuss the representative results. To do so, we make use of the *receiver operating characteristic* (ROC) curves

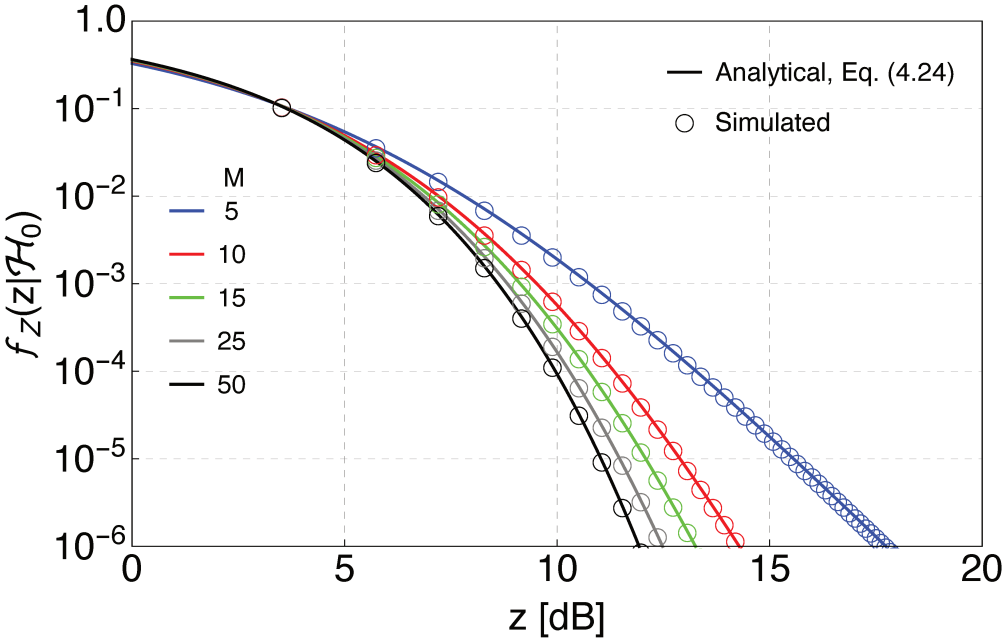

Figure 4.5 – PDF of Z under $\mathcal{H}_0$ for different values of M.

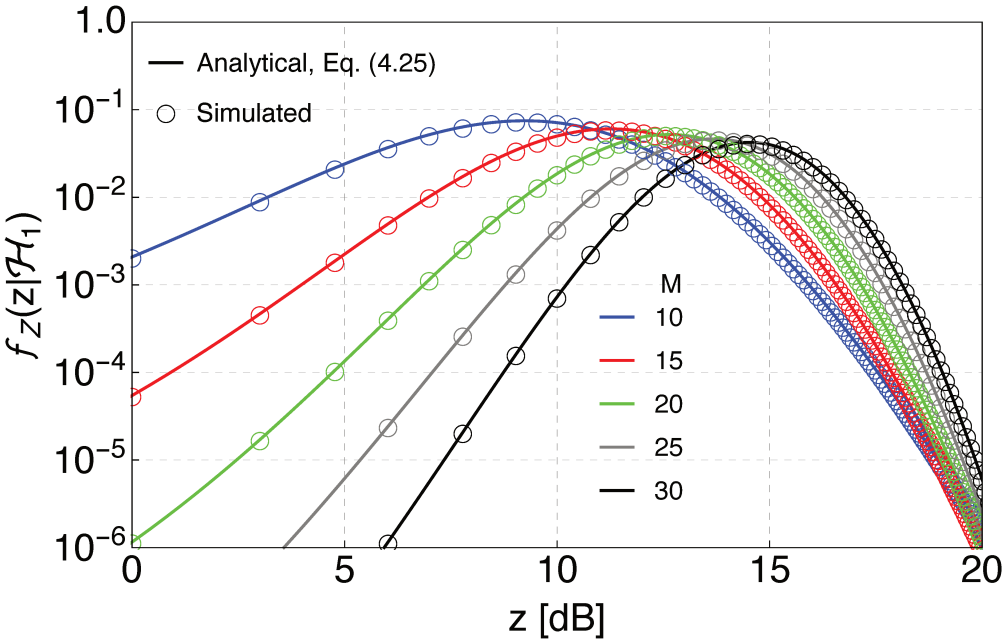

Figure 4.6 – PDF of Z under $\mathcal{H}_1$ for different values of M.

and Monte-Carlo simulations.[4] For comparison purposes, besides the pre-beamforming GLRT and square-law detectors, we also include the (optimum) LRT detector [7] so as to quantify the SNR losses.[5]

Figs. 4.5 and 4.6 show the PDF of Z (analytical and simulated) given the

[4] The number of realizations was set to 1×10^7.

[5] Herein, the SNR loss is defined as extra SNR required to achieved the same performance as the LRT detector [7, Eq. (4.3)], for a given PD.

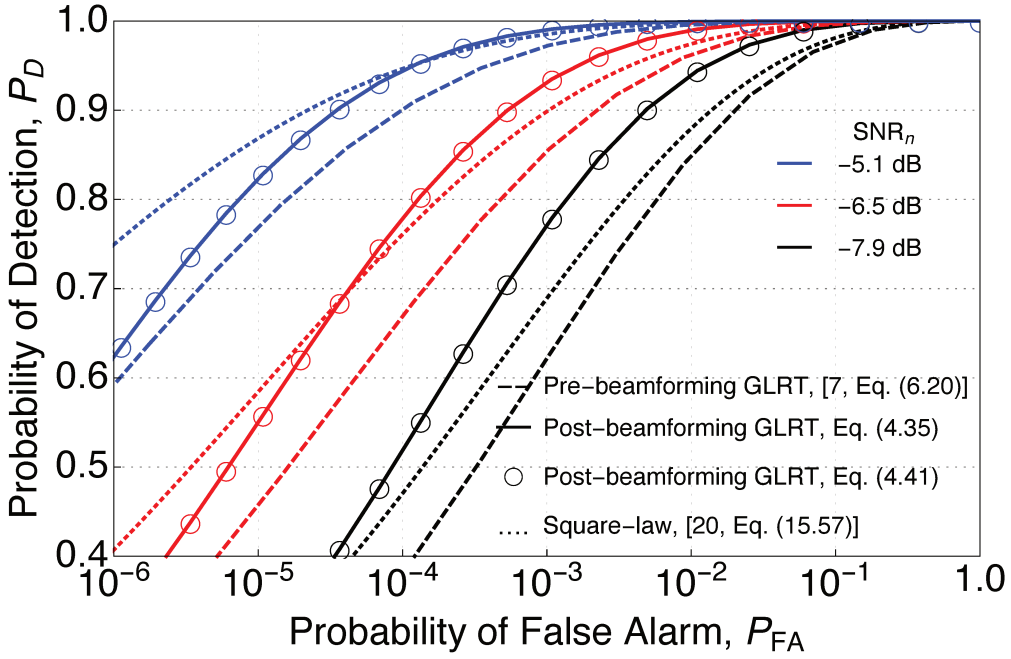

Figure 4.7 – P_{D} vs P_{FA} with $M = 22$, $N = 3$, and different values of SNR_n

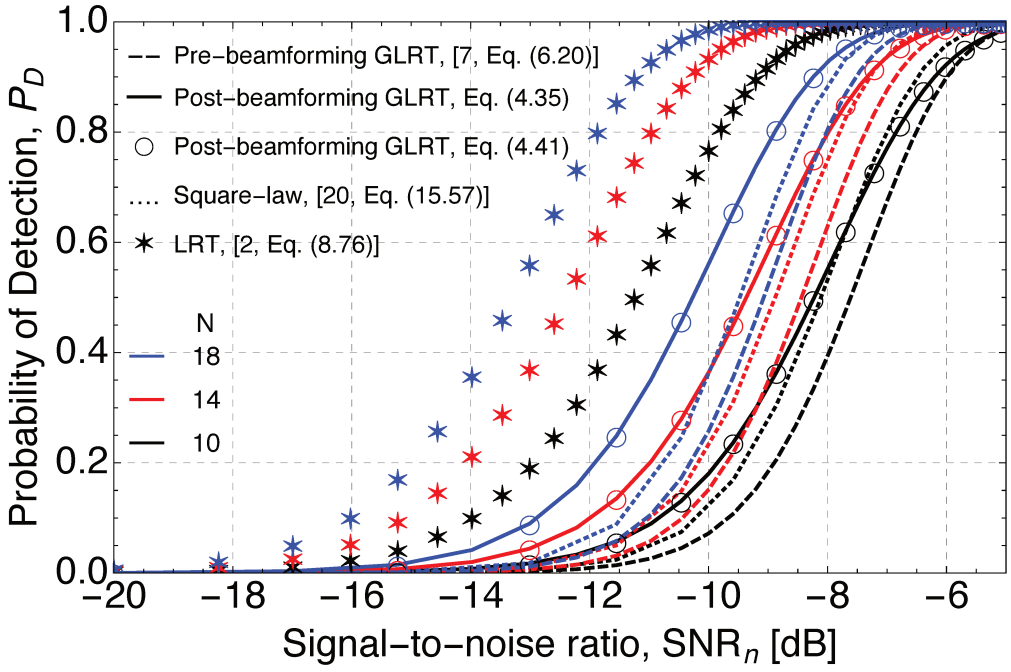

Figure 4.8 – P_{D} vs SNR_n with $M = 15$, $P_{\mathrm{FA}} = 10^{-6}$ and different values of N.

hypotheses $\mathcal{H}_0$ and $\mathcal{H}_1$, respectively. The distribution parameters have been selected to show the broad range of shapes that the PDFs can exhibit. Observe the perfect match between Monte-Carlo simulations and our derived expressions [refer to (4.24) and (4.25)].

Fig. 4.7 shows P_{D} as a function of P_{FA} (analytical and simulated) for different values of SNR_n. Observe that for low SNR_n, the post-beamforming GLRT detector is superior to both the pre-beamforming GLRT detector and the square-law detector. That is,

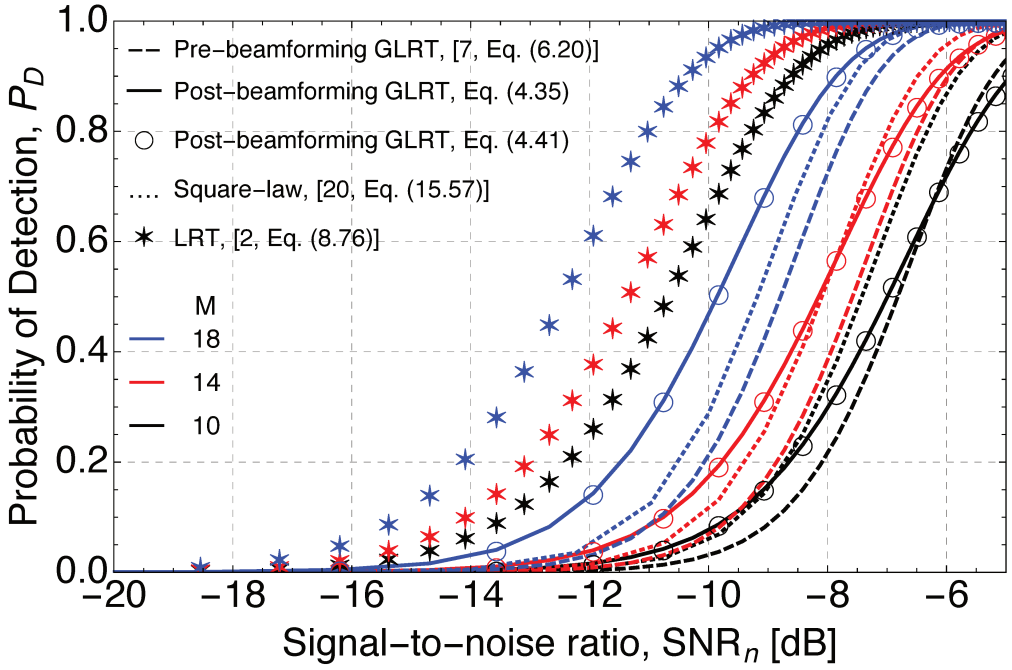

Figure 4.9 – P_{D} vs SNR_n with $N = 11$, $P_{\mathrm{FA}} = 10^{-6}$ and different values of M.

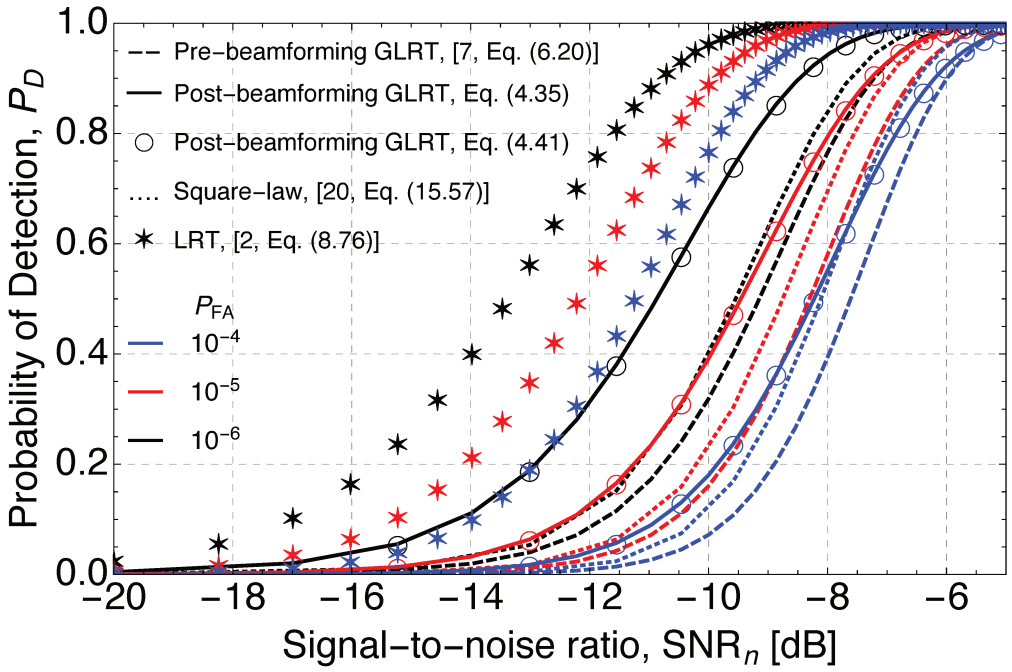

Figure 4.10 – P_{D} vs SNR_n with $M = 10$, $N = 15$ and different values of P_{FA}.

the weaker the signals, the better the performance of our proposed detector. For example, given $P_{\mathrm{FA}} = 10^{-4}$, the post-beamforming GLRT detector, the pre-beamforming GLRT detector, and the square-law detector provide, respectively, the following probabilities of detection: 0.53, 0.38 and 0.47 for $\mathrm{SNR}_n = -7.9$ dB; 0.78, 0.66 and 0.75 for $\mathrm{SNR}_n = -6.5$ dB; and finally, 0.94, 0.90 and 0.95 for $\mathrm{SNR}_n = -5.1$ dB. The following figures illustrate the impact on the PD as the SNR is reduced.

Table 4.2 – Efficiency of (4.41) as compared to (4.30).

Case	Absolute Error, ϵ	Number of terms	Computation Time for Eq. (4.30)	Computation Time for Eq. (4.41)	Reduction Time
1	5.471×10^{-10}	23	92.725×10^{-3} (s)	1.923×10^{-3} (s)	97.92 %
2	5.248×10^{-10}	30	197.044×10^{-3} (s)	2.464×10^{-3} (s)	98.74 %
3	6.032×10^{-10}	34	294.950×10^{-3} (s)	3.415×10^{-3} (s)	98.84 %
4	5.261×10^{-10}	45	96.370×10^{-3} (s)	4.625×10^{-3} (s)	95.20 %
5	5.341×10^{-10}	45	95.769×10^{-3} (s)	4.663×10^{-3} (s)	95.13 %
6	5.361×10^{-10}	45	92.911×10^{-3} (s)	4.54×10^{-3} (s)	95.11 %
7	9.339×10^{-10}	60	99.896×10^{-3} (s)	7.043×10^{-3} (s)	92.94 %
8	4.790×10^{-10}	71	95.124×10^{-3} (s)	9.238×10^{-3} (s)	90.28 %
9	6.522×10^{-10}	83	98.728×10^{-3} (s)	11.418×10^{-3} (s)	88.43 %

Fig. 4.8 shows P_{D} as a function of SNR_n (analytical and simulated) for different values of N. Note that all detectors improve as the number of antennas increases, requiring a lower SNR for a certain PD. Also, note how the post-beamforming GLRT detector overcomes the pre-beamforming GLRT detector and the square-law detector as the SNR decreases. For example, given $\mathrm{SNR}_n = -8$ dB, the post-beamforming GLRT detector, the pre-beamforming GLRT detector, and the square-law detector provide, respectively, the following probabilities of detection: 0.55, 0.40 and 0.54 for $N = 10$; 0.79, 0.64 and 0.75 for $N = 14$; and finally, 0.94, 0.80 and 0.86 for $N = 18$. Additionally, observe how the SNR loss is reduced as N increases. In particular, for a fixed $P_{\mathrm{D}} = 0.8$, the post-beamforming GLRT detector is superior to both the pre-beamforming GLRT detector and the square-law detector deliver, respectively, the following SNR losses: 3.8 dB, 4.2 dB and 2.8 dB for $N = 10$; 2.9 dB, 3.6 dB and 3.1 dB for $N = 14$; and finally, 2.8 dB, 3.9 dB and 3.5 dB for $N = 18$.

Fig. 4.9 shows P_{D} as a function of SNR_n (analytical and simulated) for different values of M. Observe that all detectors improve as the number of samples increases. This occurs because we "average down" the noise power by increasing M. Once again, the post-beamforming GLRT detector performs better than the pre-beamforming GLRT detector and the square-law detector in the low-SNR regime. More specifically, given $\mathrm{SNR}_n = -8$ dB, the post-beamforming GLRT detector, the pre-beamforming GLRT detector and the square-law detector provide, respectively, the following probabilities of detection: 0.30, 0.21 and 0.35 for $M = 10$; 0.53, 0.40 and 0.53 for $M = 14$; and finally, 0.87, 0.73 and 0.82 for $M = 18$. Moreover, observe how the SNR loss is reduced as N increases. In particular, for a fixed $P_{\mathrm{D}} = 0.8$, the post-beamforming GLRT detector, the pre-beamforming GLRT detector and the square-law detector deliver, respectively, the following SNR losses: 3.6 dB, 3.4 dB and 3.2 dB for $M = 10$; 3.4 dB, 3.5 dB and 3.1 dB for $M = 14$; and finally,

2.8 dB, 3.6 dB and 3.1 dB for $M = 18$.

Fig. 4.10 shows P_{D} as a function of SNR_n (analytical and simulated) for different values of P_{FA}. Note that all detectors improve as P_{FA} is increased. This fundamental trade-off means that if the PFA is reduced, the PD decreases as well. Observe that for low SNR, the superiority of our detector still remains. For example, given $\mathrm{SNR}_n = -8$ dB, the post-beamforming GLRT detector, the pre-beamforming GLRT detector and the square-law detector provide, respectively, the following probabilities of detection: 0.93, 0.76 and 0.84 for $P_{\mathrm{FA}} = 10^{-6}$; 0.80, 0.57 and 0.70 for $P_{\mathrm{FA}} = 10^{-5}$; and finally, 0.55, 0.40 and 0.54 for $P_{\mathrm{FA}} = 10^{-4}$. Additionally, observe how the SNR loss is reduced as N increases. In particular, for a fixed $P_{\mathrm{D}} = 0.8$, the post-beamforming GLRT detector, the pre-beamforming GLRT detector and the square-law detector deliver, respectively, the following SNR losses: 2.4 dB, 3.6 dB and 3.2 dB for $P_{\mathrm{FA}} = 10^{-6}$; 2.6 dB, 3.4 dB and 3.0 dB for $P_{\mathrm{FA}} = 10^{-5}$; and finally, 2.9 dB, 3.2 dB and 2.8 dB for $P_{\mathrm{FA}} = 10^{-4}$.

An important remark is in order. The results presented herein show that if the the received signals are weak, instead of processing the received signals separately, as described in [7, Eq. (6.20)], it is better to sum up the signals and then construct the system's *detection statistic*. Intuitively, this means that if the signal received by each antenna is defectively estimated (due to low target power or strong interference), then the system will also deliver a faulty final estimate. Therefore, it is better to reinforce (i.e., applying the beamforming operation) the overall signal before any further pre-processing. Moreover, the way we create the system's *detection statistic* enables us to improve radar detection as we increase the number of antennas while maintaining a fixed PFA.

Now, to evaluate the efficiency of (4.41) we define 9 test cases, each with a specific parameter setting and its corresponding PD, as shown in Table 4.1. With this at hand, Table 4.2 illustrates the efficiency of (4.41) by showing the absolute error, computation time, required number of terms to guarantee a certain accuracy, and reduction time [compared to (4.30)]. The absolute error can be expressed as

$$\epsilon = |P_{\mathrm{D}} - \overline{P_{\mathrm{D}}}|, \tag{4.46}$$

where $\overline{P_{\mathrm{D}}}$ is the probability of detection obtained via MATHEMATICA's built-in numerical integration.[6] Observe that for 9 different parameter settings, (4.41) converges rapidly requiring between 23 and 83 terms to guarantee an accuracy of 10^{-10}. Moreover, the computation time dropped dramatically, thereby providing reduction times above 88%. This impressive reduction can lead to major savings in computational load if one wants to evaluate the detection performance over an entire area or volume covered by the radar system.

[6] Eq. (4.30) was evaluated by using the fastest MATHEMATICA's integration method, "`GlobalAdaptive`", with an accuracy goal of 10^{-10}.

4.7 Conclusions

This paper proposed and analyzed a new GLRT phased array detector, which is projected after the analog beamforming operation. For the analysis, a *non-fluctuating* target embedded in CWGN was considered. From the practical point of view, this detector fulfils the hardware and computational constraints of most radar systems. The performance metrics – PD and PFA – were derived in *closed form* assuming a total lack of knowledge about the target echo and noise statistics. Moreover, a novel fast convergent series for the PD was also derived. This series representation proved to be very efficient and computationally tractable, showing an outstanding accuracy and impressive reductions in both computational load and computation time, compared to MATHEMATICA's built-in numerical integration. Numerical results showed that when the incoming signals are weak, it is best to combine (sum) them before any estimation or further processing. Indeed, this paper is conclusive in indicating that for low SNR, the post-beamforming GLRT detector shows superior to the pre-beamforming GLRT detector and square-law detectors. Another interesting feature about the post-beamforming GLRT detector demonstrates that for a fixed PFA, the detection threshold is independent of the number of antennas, which will allow us to maintain a certain PFA for an arbitrary number of antennas. The SNR losses for the post-beamforming GLRT detector, the pre-beamforming GLRT detector, and the square-law detector were also quantified.

4.8 Bibliography

[1] L. V. Blake, *Radar Range-performance Analysis*, 1st ed. Norwood, MA, USA: Artech House, 1986.

[2] A. Leon-Garcia, *Probability and Random Processes for Electrical Engineering*, 3rd ed. New Jersey, NJ, USA: Pearson Prentice Hall, 1994.

[3] H. Chernoff, "On the distribution of likelihood ratio," *Ann. Math. Statist.*, vol. 25, no. 3, pp. 573–578, Sept. 1954.

[4] S. M. Kay, *Fundamentals of Statistical Signal Processing: Estimation Theory*, 1st ed. New Jersey, NJ, USA: Prentice Hall PTR, 1993.

[5] S. M. Kendall and A. Stuart, *The Advanced Theory of Statistics*, 2nd ed. New York, NY, USA: Macmillan, 1979.

[6] E. Conte, A. D. Maio, and C. Galdi, "Signal detection in compound-gaussian noise: Neyman-Pearson and CFAR detectors," *IEEE Trans. Signal Process.*, vol. 48, no. 2, pp. 419–428, Feb. 2000.

[7] S. M. Kay, *Fundamentals of Statistical Signal Processing: Detection Theory*, 2nd ed. New Jersey, NJ, USA: Prentice Hall PTR, 1998.

[8] F. D. A. García, H. R. C. Mora, and N. V. O. Garzón, "GLRT detection of nonfluctuating targets in background noise using phased arrays," in *Proc. 15th International Conference on Wireless and Mobile Computing, Networking and Communications (WIMOB)*, Barcelona, Spain, Oct. 2019, pp. 1–8.

[9] S. S. Haykin and A. O. Steinhardt, *Adaptive Radar Detection and Estimation*, 1st ed. New Jersey, NJ, USA: J. Wiley, 1992.

[10] E. J. Kelly, "An adaptive detection algorithm," *IEEE Trans. Aerosp. Electron. Syst.*, vol. AES-22, no. 2, pp. 115–127, Mar. 1986.

[11] I. S. Reed, J. D. Mallett, and L. E. Brennan, "Rapid convergence rate in adaptive arrays," *IEEE Trans. Aerosp. Electron. Syst.*, vol. AES-10, no. 6, pp. 853–863, Nov. 1974.

[12] S. Bose and A. O. Steinhardt, "Optimum array detector for a weak signal in unknown noise," *IEEE Trans. Aerosp. Electron. Syst.*, vol. 32, no. 3, pp. 911–922, Jul. 1996.

[13] O. Besson, A. Coluccia, E. Chaumette, G. Ricci, and F. Vincent, "Generalized likelihood ratio test for detection of gaussian rank-one signals in gaussian noise with unknown statistics," *IEEE Trans. Signal Process.*, vol. 65, no. 4, pp. 1082–1092, Feb. 2017.

[14] N. B. Pulsone and C. M. Rader, "Adaptive beamformer orthogonal rejection test," *IEEE Trans. Signal Process.*, vol. 49, no. 3, pp. 521–529, Mar. 2001.

[15] F. C. Robey, D. R. Fuhrmann, E. J. Kelly, and R. Nitzberg, "A CFAR adaptive matched filter detector," *IEEE Trans. Aerosp. Electron. Syst.*, vol. 28, no. 1, pp. 208–216, Jan. 1992.

[16] S. Zhang, C. Guo, T. Wang, and W. Zhang, "ON–OFF analog beamforming for massive MIMO," *IEEE Trans. Veh. Technol.*, vol. 67, no. 5, pp. 4113–4123, Jan. 2018.

[17] S. Huber, M. Younis, A. Patyuchenko, G. Krieger, and A. Moreira, "Spaceborne reflector SAR systems with digital beamforming," *IEEE Trans. Aerosp. Electron. Syst.*, vol. 48, no. 4, pp. 3473–3493, Oct. 2012.

[18] S. R. J. Axelsson, "Noise radar for range/doppler processing and digital beamforming using low-bit ADC," *IEEE Trans. Geosci. Remote Sens.*, vol. 41, no. 12, pp. 2703–2720, Dec. 2003.

[19] D. Zhu, B. Li, and P. Liang, "A novel hybrid beamforming algorithm with unified analog beamforming by subspace construction based on partial CSI for massive MIMO-OFDM systems," *IEEE Trans. Commun.*, vol. 65, no. 2, pp. 594–607, Nov. 2017.

[20] M. A. Richards, J. Scheer, W. A. Holm, and W. L. Melvin, *Principles of Modern Radar: Basic Principles*, 1st ed. West Perth, WA, Australia: SciTech, 2010.

[21] G. V. Weinberg, "Noncoherent radar detection in correlated Pareto distributed clutter," *IEEE Trans. Aerosp. Electron. Syst.*, vol. 53, no. 5, pp. 2628–2636, Oct. 2017.

[22] G. V. Weinberg and C. Tran, "Noncoherent detector threshold determination in correlated Pareto distributed clutter," *IEEE Geosci. Remote Sens. Lett.*, vol. 16, no. 3, pp. 372–376, Mar. 2019.

[23] G. V. Weinberg, "Minimum-based sliding window detectors in correlated Pareto distributed clutter," *IEEE Geosci. Remote Sens. Lett.*, vol. 14, no. 11, pp. 1958–1962, Nov. 2017.

[24] M. I. Skolnik, *Introduction to Radar Systems*, 3rd ed. Ney York, NY, USA: McGraw-Hill, 2001.

[25] A. Papoulis, *Probability, Random Variables, and Stochastic Processes*, 4th ed. Ney York, NY, USA: McGraw-Hill, 2002.

[26] P. B. Patnaik, "The non-central χ^2 and F-distributions and their applications," *Biometrika*, vol. 36, no. 1, pp. 202–232, Jun. 1949.

[27] P. C. B. Phillips, "The true characteristic function of the F distribution," *Biometrika*, vol. 69, no. 1, p. 261–264, Apr. 1982.

[28] F. W. J. Olver, D. W. Lozier, R. F. Boisvert, and C. W. Clark, *NIST Handbook of Mathematical Functions*, 1st ed. Washington, DC: US Dept. of Commerce: National Institute of Standards and Technology (NIST), 2010.

[29] W. G. Bulgren, "On representations of the doubly non-central F distribution," *J. Amer. Statist.*, vol. 66, no. 333, pp. 184–186, Mar. 1971.

[30] A. P. Prudnikov, Y. A. Bryčkov, and O. I. Maričev, *Integral and Series: Vol. 3*, 2nd ed., Fizmatlit, Ed. Moscow, Russia: Fizmatlit, 2003.

[31] G. Fubini, "Sugli integrali multipli." *Rom. Acc. L. Rend. (5)*, vol. 16, no. 1, pp. 608–614, 1907.

[32] Wolfram Research, Inc. (2018), *Wolfram Research*, Accessed: Sept. 19, 2020. [Online]. Available: http://functions.wolfram.com

[33] H. R. Alhennawi, M. M. H. E. Ayadi, M. H. Ismail, and H. A. M. Mourad, "Closed-form exact and asymptotic expressions for the symbol error rate and capacity of the H-function fading channel," *IEEE Trans. Veh. Technol.*, vol. 65, no. 4, pp. 1957–1974, Apr. 2016.

[34] F. Yilmaz and M. S. Alouini, "Product of the powers of generalized nakagami-m variates and performance of cascaded fading channels," in *Proc. IEEE Global Telecommun. Conf. (GLOBECOM)*, Abu Dhabi, UAE, Nov. 2009, pp. 1–8.

[35] F. D. A. García, H. R. C. Mora, G. Fraidenraich, and J. C. S. S. Filho, "Square-law detection of exponential targets in Weibull-distributed ground clutter," *IEEE Geosci. Remote Sens. Lett.*, to be published, doi: 10.1109/LGRS.2020.3009304.

[36] E. Kreyszig, *Advanced Engineering Mathematics*, 10th ed. New Jersey, NJ, USA: John Wiley & Sons, 2010.

5 Contribution IV

This chapter is a replica of the paper below:

- F. D. A. García, A. C. F. Rodriguez, G. Fraidenraich and J. C. S. Santos Filho, "CA-CFAR Detection performance in homogeneous Weibull clutter," *IEEE Geosci. Remote Sens. Lett.*, vol. 16, no. 6, pp. 887-891, Jun. 2019. DOI:10.1109/LGRS.2018.2885451.

CA-CFAR Detection Performance in Homogeneous Weibull Clutter

Fernando Darío Almeida García Darío, Andrea Carolina Flores Rodriguez,
Gustavo Fraidenraich, and José Cândido Silveira Santo Filho

Abstract

This work presents a novel and exact formulation for the probability of detection of a cell-averaging, constant false-alarm rate (CA-CFAR) radar system operating in an homogeneous Weibull clutter environment. We consider a realistic scenario with both target returns and clutter residues within the cell under test by the radar processing. In passing, we derive novel closed-form expressions for the probability density function and the cumulative distribution function of the sum of an exponentially fluctuating target embedded in Weibull clutter. The derived exact expressions are given in terms of both (i) the bivariate Fox H-function, for which we provide a portable and efficient MATHEMATICA code, and (ii) easily computable series representations. The validity of all expressions is confirmed via Monte-Carlo simulation. The derived results are compared with the idealized Neyman-Pearson detector so as to quantify the CFAR losses, and they indicate that even a small change in the shape parameter of the clutter distribution can significantly affect the radar detection performance.

5.1 Introduction

It is well known that the performance of any radar system is governed by its probabilities of detection (PD) and false alarm (PFA). A desirable property of a detector is to maintain a constant PFA in the presence of homogeneous or heterogeneous environments. A detector that possesses this property is called a constant false-alarm rate (CFAR) detector. The CFAR detectors estimate the statistics of the interference from radar measurements and adjust the decision threshold to maintain a constant false-alarm rate [1]. Numerous detection techniques have been developed to work over different types of environments, such as cell averaging CFAR (CA-CFAR), the smallest of CFAR [2], the greatest of CFAR [3], order statistics CFAR (OS-CFAR) [4], generalized OS-CFAR [5], variability index CFAR [6], and ordered data variability CFAR [7].

In this work, we focus on the homogeneous Weibull environment. Homogeneous conditions exist when either of the following is true: (i) the interference in the leading and lagging windows and also in the cell under test (CUT) is i.i.d.; (ii) the leading and lagging

windows do not contain returns from other targets that bias the threshold. Rigorous performance analyses of CFAR detectors operating in Weibull backgrounds have been carried out in [8, 9, 10]. Recently, in [11], closed-form expressions were derived for the PD and PFA of a CFAR detector operating over homogeneous and heterogeneous environments, in which the clutter was modeled by a Weibull random variable, whereas the target was assumed to be fluctuating and was modeled by an exponential random variable [1]. Despite these contributions, none of the aforementioned works has considered the presence of clutter residues within the CUT, yet this is most likely in practice.

The effect of clutter interference within the CUT and throughout the entire data window proves indeed significant and thus should not be ignored, specially when it comes to Weibull clutter. This has been observed in practice through experimental data [8, 9]. Therefore, realistic scenarios must consider such effect for an appropriate radar design. On the other hand, due to the mathematical complexity that surrounds the use of the statistical models for this type of scenario, closed-form expressions for the corresponding PD are not available in the literature. Moreover, to calculate this new PD it is necessary to know the sum statistics of the Weibull clutter and the exponential target. Some works have analyzed the PD for exponential targets embedded in Weibull backgrounds without applying the CFAR detection (cf. [12, 13, 14] for more discussion). In these works, all calculations were performed by computational methods and, therefore, no closed-form expressions were obtained. To the best of the authors' knowledge, no closed-form solutions exist for the probability density function (PDF) and cumulative distribution function (CDF) of the sum of Weibull and exponential random variables. Therefore, the PD of a CFAR detector for the referred type of homogeneous scenario remains unknown.

Herein, motivated by the need to design more realistic CA-CFAR detectors operating in more plausible homogeneous environments, we present a closed-form solution for the PD of a CA-CFAR detector assuming the presence of both target returns and clutter residues within the CUT. The main contributions of this work are listed below:

a) Exact and novel formulations for the PD of the aforementioned CA-CFAR detector, as well as for the PDF and CDF of the sum of an Exponential target embedded in Weibull-distributed clutter. To this end, we provide an original use for the Fox H-function [15] in the field of radar systems.

b) A portable implementation in MATHEMATICA for the bivariate Fox H-function corresponding to our system model. The code is efficient and provides very accurate results.

c) Finally, we provide fast-convergence series for all the results presented here. It is worth noting that these series are also new in the literature.

In what follows, $f_{(\cdot)}(\cdot)$ denotes probability density function; $F_{(\cdot)}(\cdot)$, cumulative distribution function; $\mathbb{E}[\cdot]$, expectation; $\Pr[\cdot]$, probability; and $(\cdot)^T$, transposition.

5.2 System Model

We consider a Weibull-distributed clutter interference X with a probability density function (PDF) given by

$$f_X(x) = \begin{cases} \frac{\mu}{\lambda}\left(\frac{x}{\lambda}\right)^{\mu-1}\exp\left[-\left(\frac{x}{\lambda}\right)^{\mu}\right], & x \geq 0 \\ 0, & \text{otherwise,} \end{cases} \tag{5.1}$$

where $\mu > 0$ is the shape parameter and $\lambda > 0$ is the scale parameter. Also, we consider a fluctuating target echo Y that follows an exponential PDF, given by

$$f_Y(y) = \begin{cases} \alpha\exp\left[-\alpha y\right], & y \geq 0 \\ 0, & \text{otherwise,} \end{cases} \tag{5.2}$$

in which $\alpha > 0$ represents the rate parameter. In order to assess the performance of the CA-CFAR detector, we must consider the CUT both in presence and in absence of a target. Let Z denote the received signal. Then, $Z = X$ if no target is present, and $Z = X + Y$ otherwise. In other words, the radar detection problem can be posed as the following binary hypothesis test:

$$\mathcal{H}_0 \text{ (target absent)}: \quad Z = X, \qquad z \geq 0 \tag{5.3}$$

$$\mathcal{H}_1 \text{ (target existent)}: \quad Z = X + Y, \quad z \geq 0. \tag{5.4}$$

Following a setup that is rather common in practice, we consider that $Z \geq 0$ is provided as the output of a *square-law* rectifier [1][1]. In addition, we consider that each decision is made based on a single received pulse, i.e., no pulse integration is applied. To the best of the authors' knowledge, no closed-form solution exists for the sum statistics presented in (5.4). In this work, we solve this problem by deriving exact and closed-form expressions for the PDF and CDF of (5.4). This is attained in the next section.

[1] In practice, clutter and target echoes add to one another at the level of in-phase and quadrature components. So the addition at the level of power, assumed in (5.4), is indeed an approximation, being largely adopted in the literature [1]. More importantly, this approximation proves highly accurate in scenarios when exponentially distributed targets (our case) are embedded in strong clutter.

5.3 Sum Statistics

5.3.1 Probability Density Function

Since the target and clutter are independent random processes, we can express the sum statistics defined in (5.4) as a convolution problem, so that [16]

$$f_Z\left(z|\mathcal{H}_1\right) = \int_0^z f_X\left(\tau\right) f_Y\left(z-\tau\right) \mathrm{d}\tau. \tag{5.5}$$

Now, substituting (5.1) and (5.2) in (5.5), and after some manipulations, we obtain

$$f_Z\left(z|\mathcal{H}_1\right) = \frac{\mu\alpha}{\lambda} \int_0^z G_{0,1}^{1,0}\left[\begin{array}{c|c} - & \left(\frac{z-\tau}{\lambda}\right)^{\mu} \\ 0 & \end{array} \right] G_{0,1}^{1,0}\left[\begin{array}{c|c} - & \alpha\tau \\ 0 & \end{array} \right] \left(\frac{z-\tau}{\lambda}\right)^{-1+\mu} \mathrm{d}\tau, \tag{5.6}$$

where $G_{m,n}^{p,q}\left[\cdot\right]$ is the Meijer's G-function [17, Eq. (8.2.1.1)].

Finally, by making use of [18, Eq. (6.2.8)] and after several algebraic manipulations, a closed-form solution for (5.5) is obtained as

$$f_Z\left(z|\mathcal{H}_1\right) = C_{f_Z} \mathbf{H}\left[\mathbf{x}; \left(\delta, \mathbf{D}\right); \left(\beta_{f_Z}, \mathbf{B}\right); \mathcal{L}_{\mathbf{s}}\right], \tag{5.7}$$

where $C_{f_Z} \triangleq \mu\alpha \left(\frac{z}{\lambda}\right)^{\mu}$, $\mathbf{x} = \left[\left(\frac{z}{\lambda}\right)^{\mu}, \alpha z\right]$, $\delta = [0, 0, \mu, 1]$, $\beta_{f_Z} = [1+\mu]$, $\mathcal{L}_{\mathbf{s}} = \mathcal{L}_{\mathbf{s}_1} \times \mathcal{L}_{\mathbf{s}_2}$, and

$$\mathbf{D} = \begin{pmatrix} 1 & 0 & -\mu & 0 \\ 0 & 1 & 0 & -1 \end{pmatrix}^T, \quad \mathbf{B} = \begin{pmatrix} -\mu & -1 \end{pmatrix}. \tag{5.8}$$

5.3.2 Cumulative Distribution Function

Using (5.6), and after changing the order of integration, we obtain a closed-form expression for the CDF of (5.4) as

$$\begin{aligned} F_Z\left(z|\mathcal{H}_1\right) \triangleq & \Pr\left[Z \leq z|\mathcal{H}_1\right] \\ = & \int_0^z f_Z\left(\nu|\mathcal{H}_1\right) \mathrm{d}\nu \\ = & C_{F_Z} \mathbf{H}\left[\mathbf{x}; \left(\delta, \mathbf{D}\right); \left(\beta_{F_Z}, \mathbf{B}\right); \mathcal{L}_{\mathbf{s}}\right], \end{aligned} \tag{5.9}$$

where $C_{F_Z} \triangleq \mu\alpha z \left(\frac{z}{\lambda}\right)^{\mu}$, $\beta_{F_Z} = [2+\mu]$, and the remaining parameters are the same as in (5.7).

5.4 CA-CFAR Detection

Following the system model described in section 5.2, we now execute a thorough performance analysis of the CA-CFAR detector, by deriving exact and novel solutions for the PD. This is examined in detail in the following subsections.

5.4.1 CA-CFAR Algorithm

The basic architecture of the CFAR algorithm is shown in Fig. 5.1. Observe that the samples at the output of the rectifier are stored in a computer memory as a one-dimensional vector. This vector is commonly referred to as the data window and is composed of several thousand cells (also called *range bins*) [1]. However, this number can vary significantly depending on the radar operation mode. The number of cells within the data window depends strongly on the range resolution[2] of the radar. The CFAR window resides within the data window and is composed of leading and lagging reference windows, guard cells (Gs), and the CUT [1]. It is worth noting that the leading and lagging reference windows possess the same number of cells (cf. Fig. 5.1).

The CA-CFAR algorithm runs as follows:

1. First, the CA-CFAR estimates the unknown interference power from a collection of samples, assumed to be i.i.d. To do so, the maximum likelihood estimation (MLE) is applied over the leading and lagging reference windows.

2. Then, a CA-CFAR threshold T is defined, formed by the product of the estimated interference power and the CA-CFAR constant ξ— to be determined from Steps 3 and 4 as a function of n, μ, and the average PFA.

3. Next, the algorithm computes the conditional probabilities of detection, $\dot{P}_D$, and false alarm, $\dot{P}_{FA}$, in terms of the estimated interference power. This is performed by comparing the statistics of the CUT under both hypotheses ($\mathcal{H}_0$ and $\mathcal{H}_1$) with the CA-CFAR threshold T.

4. Finally, the average probabilities of detection, $\overline{P}_D$, and false alarm, $\overline{P}_{FA}$, are found by removing the dependence of the interference statistics.

All these steps will be clarified in the next subsection.

5.4.2 CA-CFAR Performance Analysis

Let $\underline{X} = \{X_1, X_2, \cdots, X_n\}$ be a sequence of i.i.d. Weibull random variables, where n is the total number of cells within the leading and lagging reference windows.

[2] The range resolution is defined as the minimum distance in which a radar can resolve two targets over a given range [1]. The smaller the distance, the better the resolution.

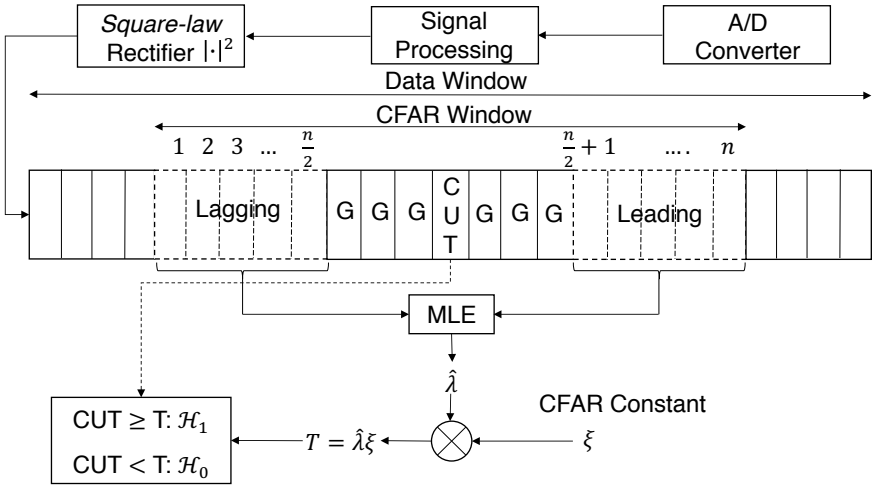

Figure 5.1 – CFAR architecture.

Then, the joint PDF of $\underline{X}$ is given by the product of the marginal PDFs, reducing to

$$\begin{aligned} f_{\underline{X}}\left(\underline{X}\right) &\triangleq \prod_{i=1}^{n} f_{X_i}\left(x_i\right) \\ &= \left(\frac{\mu}{\lambda}\right)^n \exp\left[-\sum_{i=1}^{n}\left(\frac{x_i}{\lambda}\right)^{\mu}\right] \prod_{i=1}^{n}\left(\frac{x_i}{\lambda}\right)^{\mu-1}. \end{aligned} \tag{5.10}$$

The MLE for the unknown parameter λ given in (5.10) can be computed as [19]

$$\hat{\lambda}^{\hat{\mu}} = \frac{1}{n}\sum_{i=1}^{n} X_i^{\hat{\mu}}, \tag{5.11}$$

where $\hat{\mu}$ is the MLE for μ, which can be found by solving the following equation [20]:

$$\frac{\sum_{i=1}^{n} X_i^{\hat{\mu}} \ln\left(X_i\right)}{\sum_{i=1}^{n} X_i^{\hat{\mu}}} - \frac{1}{\hat{\mu}} - \frac{1}{n}\sum_{i=1}^{n} \ln\left(X_i\right) = 0. \tag{5.12}$$

Note that (5.12) is transcendental and, as such, must be solved by numerical means. Alternatively, a common, yet somewhat arbitrary practice in CA-CFAR design is to adopt $\hat{\mu} = 1$, specially when a large radar resolution cell[3] is at play (e.g., in low-resolution imaging radars). Following this practice, herein we adopt $\hat{\mu} = 1$. Note that this is but an approximate receiver-design criterion, with the true shape parameter μ of the Weibull clutter being still considered to be arbitrary in the performance analysis that follows. Under this scenario, (5.11) becomes the normalized sum of independent exponential random variables, each with the same rate parameter $1/\lambda$. Hence, the PDF of $\hat{\lambda}$ can be written as [16]

$$f_{\hat{\lambda}}(\hat{\lambda}) = \frac{n\lambda^{-n}\left(\hat{\lambda}n\right)^{n-1}}{\Gamma(n)} \exp\left[-\frac{\hat{\lambda}n}{\lambda}\right]. \tag{5.13}$$

[3] The ability of a radar system to resolve two targets over range, azimuth, and elevation defines its resolution cell [1].

For our purposes, it is convenient to express X in terms of two independent normal variables I_X and Q_X, that is [21]

$$X = \left(I_X^2 + Q_X^2\right)^{1/\mu}, \tag{5.14}$$

in which I_X and Q_X are identically distributed according to $\mathcal{N}(0, \sigma_X^2)$.[4] The scale parameter of the Weibull distribution is related to σ_X^2 by $\lambda = (2\sigma_X^2)^{1/\mu}$. Therefore, the interference power before the *square-law* rectifier can be written as [1]

$$\mathbb{E}\left[|I_X + jQ_X|^2\right] = 2\sigma_X^2 = \lambda^\mu. \tag{5.15}$$

Following the same approach as in (5.14), we can write Y as

$$Y = I_Y^2 + Q_Y^2, \tag{5.16}$$

where I_Y and Q_Y are identically distributed according to $\mathcal{N}(0, \sigma_Y^2)$, and consequently, the target power before detection can be computed as

$$\mathbb{E}\left[|I_Y + jQ_Y|^2\right] = 2\sigma_Y^2 = \alpha^{-1}. \tag{5.17}$$

Now, we can define the signal-to-clutter ratio (SCR) as

$$\begin{aligned} \text{SCR} &\triangleq \frac{\mathbb{E}\left[|I_Y + jQ_Y|^2\right]}{\mathbb{E}\left[|I_X + jQ_X|^2\right]} \\ &= (\alpha\lambda^\mu)^{-1}. \end{aligned} \tag{5.18}$$

Using (5.15) and the design criterion $\hat{\mu} = 1$, we can express T as follows:

$$T = \hat{\lambda}\xi. \tag{5.19}$$

Conditioned on $\hat{\lambda}$, $\dot{P}_{FA}$ and $\dot{P}_D$ can be computed by integrating (5.1) and (5.7) from T to infinity [1], respectively. Hence, $\dot{P}_{FA}$ can be written as

$$\begin{aligned} \dot{P}_{FA} &\triangleq \int_{\hat{\lambda}\xi}^{\infty} f_Z\left(z|\mathcal{H}_0\right) \mathrm{d}z \\ &= \exp\left[-\left(\frac{\hat{\lambda}\xi}{\lambda}\right)^\mu\right], \end{aligned} \tag{5.20}$$

and $\dot{P}_D$ can be easily obtained by subtracting (5.9) from unity, with $z = \hat{\lambda}\xi$, i.e.,

$$\dot{P}_D = 1 - C_{P_D}\mathbf{H}\left[\mathbf{x}_{P_D}; (\delta, \mathbf{D}); (\beta_{F_Z}, \mathbf{B}); \mathcal{L}_\mathbf{s}\right], \tag{5.21}$$

where $C_{P_D} \triangleq \mu\alpha\hat{\lambda}\xi\left(\frac{\hat{\lambda}\xi}{\lambda}\right)^\mu$ and $\mathbf{x}_{P_D} = \left[\left(\frac{\hat{\lambda}\xi}{\lambda}\right)^\mu, \alpha\hat{\lambda}\xi\right]$. It remains to find $\overline{P}_{FA}$ and $\overline{P}_D$. This is achieved by averaging (5.20) and (5.21) over all possible values of the estimated

[4] $\mathcal{N}(a, b)$ denotes a normal (Gaussian) distribution with mean a and variance b.

parameter $\hat{\lambda}$. Using (5.13) and (5.20), and after some algebraic manipulations, $\overline{P}_{FA}$ can be calculated as

$$\begin{aligned}\overline{P}_{FA} &\triangleq \int_0^\infty \dot{P}_{FA}\, f_{\hat{\lambda}}(\hat{\lambda})\, \mathrm{d}z \\ &= \left(\left(\frac{\xi}{n}\right)^{\mu} + 1\right)^{-n}. \end{aligned} \tag{5.22}$$

By isolating ξ in (5.22), we obtain

$$\xi = n\left({\overline{P}_{FA}}^{-1/n} - 1\right)^{1/\mu}. \tag{5.23}$$

Finally, using (5.13), (5.21), and (5.23), and after lengthy algebraic manipulations, $\overline{P}_D$ can be computed in closed-form as

$$\begin{aligned}\overline{P}_D &\triangleq \int_0^\infty \dot{P}_D\, f_{\hat{\lambda}}(\hat{\lambda})\, \mathrm{d}z \\ &= 1 - C_{\overline{P}_D}\mathbf{H}\left[\mathbf{x}_{\overline{P}_D}; \left(\delta_{\overline{P}_D}, \mathbf{D}_{\overline{P}_D}\right); (\beta_{F_Z}, \mathbf{B}); \mathcal{L}_{\mathbf{s}}\right], \end{aligned} \tag{5.24}$$

where $\mathbf{x}_{\overline{P}_D} = \left[{\overline{P}_{FA}}^{-1/n} - 1, \alpha\lambda\left({\overline{P}_{FA}}^{-1/n} - 1\right)^{1/\mu}\right]$, $\delta_{\overline{P}_D} = [0, 0, \mu, 1, \mu + n + 1]$, and

$$C_{\overline{P}_D} = \frac{\left(\alpha\lambda\mu\left({\overline{P}_{FA}}^{-1/n} - 1\right)^{1/\mu+1}\right)}{\Gamma(n)}, \qquad \mathbf{D}_{\overline{P}_D} = \begin{pmatrix} 1 & 0 & -\mu & 0 & -\mu \\ 0 & 1 & 0 & -1 & -1 \end{pmatrix}^T.$$

Eq. (5.24) is the main analytical contribution of this work.

5.5 Series Representations

The multivariate Fox H-function is not yet available in mathematical packages such as MATHEMATICA, MATLAB, or MAPLE. Some works have been done to alleviate this problem [22, 23]. Specifically, in [22] a Python implementation for the Fox H-function was carried out, ranging from one up to four branches. Unfortunately, there is no general implementation for the multivariate Fox H-function so far.

In this work, we provide an accurate and easy implementation in MATHEMATICA for the bivariate Fox H-function that fits our systemic model. The code used to compute (5.7), (5.9), and (5.24) is presented in Appendix C.1. In addition, equivalent series representations are also provided next, in order to facilitate the use of our results. To do so, an exhaustive calculus of residues was used to evaluate the derived Fox H-functions. Once applied the sum of residues [24], and after several algebraic manipulations, (5.7), (5.9), and (5.24) can be written, alternatively, as

$$f_Z\left(z|\mathcal{H}_1\right) = \frac{\mu\alpha\exp\left[-\alpha z\right]}{(-\alpha\lambda)^{\mu}} \sum_{i=0}^{\infty} \frac{\left(-(-\alpha\lambda)^{\mu}\right)^{-i}\Gamma(\mu + i\mu, 0, -z\alpha)}{i!} \tag{5.25}$$

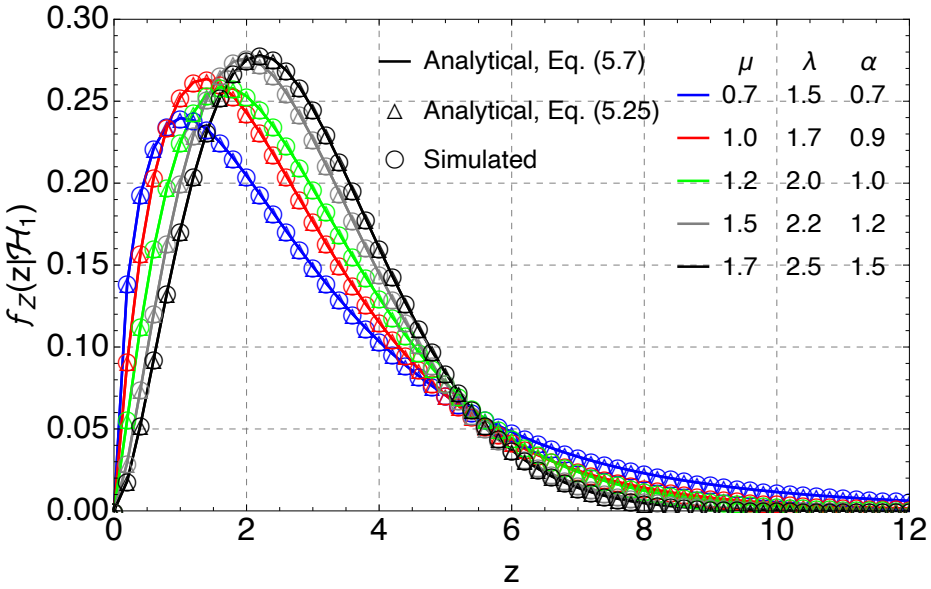

Figure 5.2 – Simulated and analytical PDF of Z under hypothesis $\mathcal{H}_1$ for different values of μ, λ, and α.

$$F_Z\left(z|\mathcal{H}_1\right) = \frac{-\exp\left[-\alpha z\right]}{(-\alpha\lambda)^{\mu}} \sum_{i=0}^{\infty} \frac{\left(-(-\alpha\lambda)^{\mu}\right)^{-i} \Gamma(i\mu+\mu+1, 0, -z\alpha)}{\Gamma(i+2)} \tag{5.26}$$

$$\overline{P}_D = 1 - \frac{\alpha\lambda\mu\left(\overline{P}_{FA}{}^{-\frac{1}{n}} - 1\right)^{\frac{1}{\mu}+1}}{\Gamma(n)} \sum_{i=0}^{\infty} \left\{ \frac{\left(-\left(\overline{P}_{FA}{}^{-\frac{1}{n}} - 1\right)\right)^{i} \Gamma(i\mu+\mu)\ \Gamma(n+i\mu+\mu+1)}{i!\ \Gamma(i\mu+\mu+2)} \right.$$
$$\left. \times\ {}_2F_1\left(1, n+i\mu+\mu+1; i\mu+\mu+2; -\alpha\lambda\left(\overline{P}_{FA}{}^{-\frac{1}{n}} - 1\right)^{\frac{1}{\mu}}\right)\right\}, \tag{5.27}$$

where $\Gamma(\cdot,\cdot,\cdot)$ denotes the generalized incomplete gamma function [25, Eq. (8.2.3)], and ${}_2F_1\left(\cdot,\cdot,\cdot,\cdot\right)$ is the Gauss hypergeometric function [25, Eq. (15.1.1)]. Eqs. (5.25), (5.26), and (5.27) are original contributions of this work.

5.6 Numerical Results

Figs. 5.2 and 5.3 show the analytical (refer to (5.7), (5.9), (5.25) and (5.26)) and simulated (via Monte-Carlo simulation) PDF and CDF of Z given the hypothesis $\mathcal{H}_1$. The distribution parameters have been selected to show the broad range of shapes that the PDF and CDF can exhibit. The series presented in (5.25)–(5.27) prove to be very efficient, converging rapidly to attain an excellent accuracy. For example, the observed number of terms needed to guarantee a precision of 10^{-12} in all the curves presented in Figs. 5.2 and 5.3 varies between 20 and 55. For practical purposes, such a small number of terms leads to a considerable reduction in computational time.

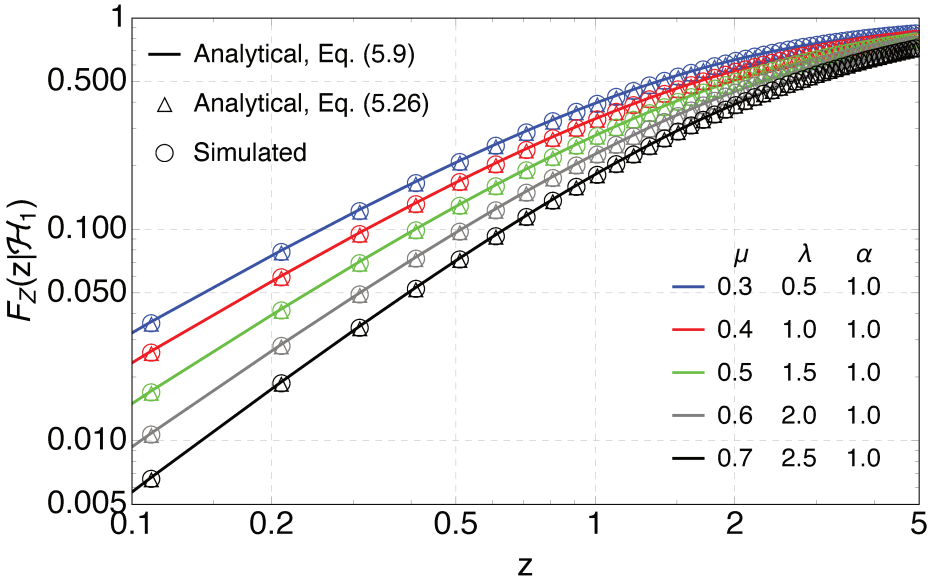

Figure 5.3 – Simulated and analytical CDF of Z under hypothesis $\mathcal{H}_1$ for different values of μ, λ, and α.

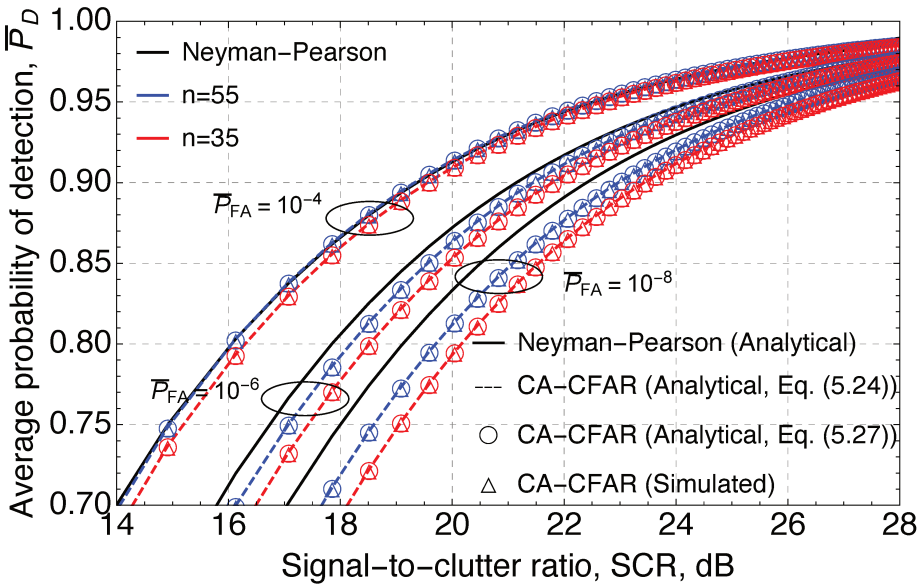

Figure 5.4 – ROC curves for the Neyman-Pearson and the investigated CA-CFAR detectors, with $\mu = 1$ and different values of $\overline{P}_{FA}$ and n.

Fig. 5.4 shows the analytical (refer to (5.24) and (5.27)) and simulated *receiver operating characteristic* (ROC) curves for the investigated CA-CFAR detector. As a term of comparison, the (idealized) Neyman-Pearson detector is also shown. Observe how the required SCR increases as $\overline{P}_{FA}$ decreases, for any given values of n and $\overline{P}_D$, as expected. The increase in n has also a positive effect on the performance of the CA-CFAR detector. This occurs because the variance of the estimated interference power decreases with increasing n. Fig. 5.4 also allows us to quantify the CFAR losses. More specifically, for fixed values of $\overline{P}_D = 80\%$ and $n = 35$, the CFAR losses under a $\overline{P}_{FA}$ of 10^{-4}, 10^{-6}, and 10^{-8}

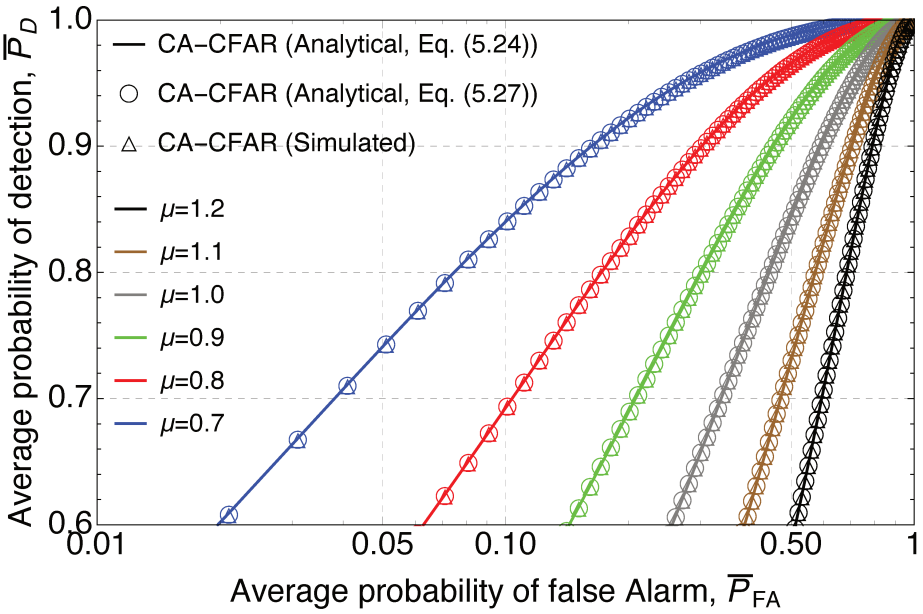

Figure 5.5 – $\overline{P}_D$ versus $\overline{P}_{FA}$ for $\lambda = 10$, $\alpha = 0.1$, $n = 55$, and varying μ.

are approximately 0.4, 0.7, and 1.1 dB, respectively; and for fixed values of $\overline{P}_D = 80\%$ and $n = 55$, the CFAR losses under a $\overline{P}_{FA}$ of 10^{-4}, 10^{-6}, and 10^{-8} are approximately nil, 0.5, and 0.6 dB, respectively. Note that as $n \to \infty$ the CA-CFAR detector approaches the performance of the Neyman-Pearson detector, as shown in Fig. 5.4 for $\overline{P}_{FA} = 10^{-4}$ and $n = 55$.

Finally, Fig. 5.5 illustrates $\overline{P}_D$ vs. $\overline{P}_{FA}$ for different values of μ. Note how the radar performance deteriorates as μ increases, i.e., the higher the value of μ, the smaller the value of $\overline{P}_D$ achieved under a given target value of $\overline{P}_{FA}$.

5.7 Conclusions

This paper offers novel exact formulations for the probability of detection of a CA-CFAR detector as well as closed-form expressions for the PDF and CDF of the sum of an exponentially fluctuating target embedded in Weibull clutter. All the expressions are given in terms of the Fox H-function and can be used for the theoretical study of CA-CFAR detectors operating in homogeneous Weibull clutter. Series representations for all the results presented here are also provided. It is important to emphasize that the series given in (5.25)–(5.27) arise naturally from the sum of residues and are not unique, i.e., other series expansions are possible.

5.8 Bibliography

[1] M. A. Richards, J. Scheer, W. A. Holm, and W. L. Melvin, *Principles of Modern Radar: Basic Principles*, 1st ed. West Perth, WA, Australia: SciTech, 2010.

[2] G. V. Trunk, "Range resolution of targets using automatic detectors," *IEEE Trans. Aerosp. Electron. Syst.*, vol. AES-14, no. 5, pp. 750–755, Sept. 1978.

[3] V. G. Hansen and J. H. Sawyers, "Detectability loss due to 'greatest of' selection in a cell-averaging CFAR," *IEEE Trans. Aerosp. Electron. Syst.*, vol. AES-16, no. 1, pp. 115–118, Jan. 1980.

[4] H. Rohling, "Radar CFAR thresholding in clutter and multiple target situations," *IEEE Trans. Aerosp. Electron. Syst.*, vol. AES-19, no. 4, pp. 608–621, Jul. 1983.

[5] C. J. Kim, D. S. Han, and H. S. Lee, "Generalized OS CFAR detector with noncoherent integration," *Signal Process.*, vol. 31, no. 1, pp. 43–56, 1993.

[6] M. E. Smith and P. K. Varshney, "Intelligent CFAR processor based on data variability," *IEEE Trans. Aerosp. Electron. Syst.*, vol. 36, no. 3, pp. 837–847, Jul. 2000.

[7] A. Farrouki and M. Barkat, "Automatic censoring CFAR detector based on ordered data variability for nonhomogeneous environments," *Proc. Inst. Elect. Eng.—Radar, Sonar Navig*, vol. 152, no. 1, pp. 43–51, Feb. 2005.

[8] T. Bucciarelli, "CFAR problems in Weibull clutter," *Electron. Lett.*, vol. 21, no. 8, pp. 286–304, Apr. 1985.

[9] D. C. Schleher, "Radar detection in Weibull clutter," *IEEE Trans. Aerosp. Electron. Syst.*, vol. AES-12, no. 6, pp. 736–743, Nov. 1976.

[10] M. Baadeche and F. Soltani, "Performance analysis of mean level constant false alarm rate detectors with binary integration in Weibull background," *IET Radar Sonar Navig.*, vol. 9, no. 3, pp. 233–240, Mar. 2015.

[11] A. Abbadi, H. Bouhedjeur, A. Bellabas, T. Menni, and F. Soltani, "Generalized closed-form expressions for CFAR detection in heterogeneous environment," *IEEE Geosci. Remote Sens. Lett.*, vol. 15, no. 7, pp. 1011–1015, Jul. 2018.

[12] R. L. Mitchell and J. F. Walker, "Recursive methods for computing detection probabilities," *IEEE Trans. Aerosp. Electron. Syst.*, vol. AES-7, no. 4, pp. 671–676, Jul. 1971.

[13] D. A. Shnidman, "Radar detection probabilities and their calculation," *IEEE Trans. Aerosp. Electron. Syst.*, vol. 31, no. 3, pp. 928–950, Jul. 1995.

[14] A. Ephrath, Z. Eshcoli, and F. Berkowitz, "Probability of detection for $\mathcal{X}^2$ radar target in Weibull clutter," in *Proc. IEEE International Conference on Microwaves, Communications, Antennas and Electronic Systems (COMCAS)*, Tel Aviv, Israel, Nov 2011, pp. 1–5.

[15] N. T. Hai and H. M. Srivastava, "The convergence problem of certain multiple Mellin-Barnes contour integrals representing H-functions in several variables," *Computers & Mathematics with Applications*, vol. 29, no. 6, pp. 17–25, 1995.

[16] A. Papoulis, *Probability, Random Variables, and Stochastic Processes*, 4th ed. Ney York, NY, USA: McGraw-Hill, 2002.

[17] A. P. Prudnikov, Y. A. Bryčkov, and O. I. Maričev, *Integral and Series: Vol. 3*, 2nd ed., Fizmatlit, Ed. Moscow, Russia: Fizmatlit, 2003.

[18] M. D. Springer, *The Algebra of Random Variables*. New York, NY, USA: Wiley, 1979.

[19] S. M. Kay, *Fundamentals of Statistical Signal Processing: Estimation Theory*, 1st ed. New Jersey, NJ, USA: Prentice Hall PTR, 1993.

[20] ——, *Fundamentals of Statistical Signal Processing: Detection Theory*, 2nd ed. New Jersey, NJ, USA: Prentice Hall PTR, 1998.

[21] W. J. Szajnowski, "The generation of correlated Weibull clutter for signal detection problems," *IEEE Trans. Aerosp. Electron. Syst.*, vol. AES-13, no. 5, pp. 536–540, Sept. 1977.

[22] H. R. Alhennawi, M. M. H. E. Ayadi, M. H. Ismail, and H. A. M. Mourad, "Closed-form exact and asymptotic expressions for the symbol error rate and capacity of the H-function fading channel," *IEEE Trans. Veh. Technol.*, vol. 65, no. 4, pp. 1957–1974, Apr. 2016.

[23] F. Yilmaz and M. S. Alouini, "Product of the powers of generalized nakagami-m variates and performance of cascaded fading channels," in *Proc. IEEE Global Telecommun. Conf. (GLOBECOM)*, Abu Dhabi, UAE, Nov. 2009, pp. 1–8.

[24] E. Kreyszig, *Advanced Engineering Mathematics*, 10th ed. New Jersey, NJ, USA: John Wiley & Sons, 2010.

[25] M. Abramowitz and I. A. Stegun, *Handbook of Mathematical Functions with Formulas, Graphs, and Mathematical Tables*, 10th ed. Washington, DC: US Dept. of Commerce: National Bureau of Standards, 1972.

6 Contribution V

This chapter is a replica of the paper below:

- F. D. A. García, H. R. C. Mora, G. Fraidenraich and J. C. S. Santos Filho, "Square-Law Detection of Exponential Targets in Weibull-Distributed Ground Clutter," to appear in *IEEE Geosci. Remote Sens. Lett.*, DOI:10.1109/LGRS.2020.3009304.

Square-Law Detection of Exponential Targets in Weibull-Distributed Ground Clutter

Fernando Darío Almeida García, Henry Ramiro Carvajal Mora, Gustavo Fraidenraich, and José Cândido Silveira Santos Filho

Abstract

Modern radar systems use square-law detectors to search and track fluctuating targets embedded in Weibull-distributed ground clutter. However, the theoretical performance analysis of square-law detectors in the presence of Weibull clutter leads to cumbersome mathematical formulations. Some studies have circumvented this problem by using approximations or mathematical artifacts to simplify calculations. In this work, we derive a *closed-form* and *exact* expression for the probability of detection of a square-law detector in the presence of exponential targets and Weibull-distributed ground clutter, given in terms of the Fox H-function. Unlike previous studies, no approximations nor simplifying assumptions are made throughout our analysis. Furthermore, we derive a fast convergent series for the referred probability of detection by exploiting the orthogonal selection of poles in Cauchy's residue theorem. In passing, we also obtain closed-form solutions and series representations for the probability density function and the cumulative distribution function of the sum statistics that govern the output of a square-law detector. Numerical results and Monte-Carlo simulations corroborate the validity of our expressions.

6.1 Introduction

The detection performance of any radar system appears as a trade-off between its probability of detection (PD) and its probability of false alarm (PFA). Many modern radar systems use square-law detectors to build decision-variable statistics, which ultimately govern PD and PFA [1]. Therefore, it is of great interest to analyze the resulting statistics for that type of detector. Unfortunately, the presence of unwanted signals such as thermal noise, clutter, and jamming, ubiquitous in practice, often render the referred analysis very complicated.

The radar performance can be significantly degraded in the presence of ground clutter. Through experimental data, it has been observed that the ground-clutter statistics are well modeled by the Weibull distribution [2, 3]. As a result, the Weibull distribution has been widely used to assess the radar performance in the presence of ground clutter. Regarding square-law detectors, approximations and simplifying assumptions have been

used to alleviate the mathematical complexity of an exact analysis [4, 5, 6, 7, 8]. In [4, 5, 6], for example, the authors considered the presence of exponential[1] targets and Weibull clutter. In those works, it was assumed that, since the clutter and target echoes add to one another at the level of in-phase and quadrature components, the output of a square-law detector can be approximated as a power sum of the clutter and target echoes. Such approximation is accurate when the interference power is higher than the target power, which holds true for most practical scenarios. Moreover, in [7, 8], the authors simplified the performance analysis by assuming a particular value for the shape parameter of the Weibull distribution. Those works also considered exponential targets.

To mitigate or partially remove the harmful effects of ground clutter, modern radars use adaptive techniques to dynamically set the detection threshold above the interference level. Such techniques seek to maintain a constant false-alarm rate (CFAR) by estimating the interference power over a data window, also called CFAR window [1]. Some works have analyzed the radar performance using square-law detectors, CFAR techniques, exponential targets, and Weibull backgrounds [10, 11, 6]. In those analyses, the clutter was assumed to be present only in the CFAR window but not within the cell under test (CUT) [1]. Furthermore, the value of the Weibull shape parameter was fixed to unity, which reduces to the exponential distribution. Of course, this is too strong a constraint that most practical scenarios fail to meet [12].

Recently, the presence of clutter residues within the CUT was considered in [13], for a cell-averaging CFAR radar system with Weibull interference and exponential targets. In fact, as far as we know, [13] contains the only published such analysis for clutter residues within the CUT. Closed-form expressions for PD and PFA were obtained therein. As in [4, 5, 6], the analysis capitalized on a highly accurate approximation for the output statistics of a square-law detector, as a power sum of the target echoes and the clutter interference. Furthermore, and unlike previous works, in [13] the shape parameter of the Weibull interference was allowed to have arbitrary values, thereby providing more realistic detection estimates when dealing with ground-clutter environments.

To the best of the authors' knowledge, no radar performance analysis has been published so far using the exact statistics of a square-law detector when subject to exponential targets and Weibull clutter interference. This lack is mainly due to the high degree of mathematical complexity that surrounds the detection statistics under this type of scenario. In this work, we derive a *closed-form exact* expression for PD (versus PFA) in the referred scenario, written in terms of the Fox H-function. In addition, we derive a fast convergent series for PD. In passing, we obtain closed-form solutions and series

[1] An exponential target refers to a class of fluctuating targets introduced by Swerling [9]. In this case, the target's radar cross-section after an envelope detector follows an exponential distribution.

representations for the probability density function (PDF) and the cumulative distribution function (CDF) of the sum statistics that govern the output of a square-law detector. No approximations nor simplifying assumptions are made throughout our analysis.

It is worth mentioning that the results presented herein can be readily used to analyze the performance of any CFAR scheme operating over exponential targets and Weibull clutter within the CUT. This can be done by comparing our derived statistics against the adaptive threshold that results from estimating the interference power along the CFAR window.

In what follows, $f_{(\cdot)}(\cdot)$ denotes PDF; $F_{(\cdot)}(\cdot)$, CDF; $\mathbb{E}[\cdot]$, expectation; $\Pr[\cdot]$, probability; $|\cdot|$, absolute value; $\lfloor\cdot\rfloor$, floor operation; and $(\cdot)^T$, transposition.

6.2 Problem Statement

In this work, we handle the radar detection problem in terms of the following binary hypothesis test:

- Hypothesis $\mathcal{H}_0$: Weibull clutter alone.
- Hypothesis $\mathcal{H}_1$: exponential target plus Weibull clutter.

Depending on the hypothesis at hand, the output of a square-law detector can be written as [11, 12, 14, 15]

$$\mathcal{H}_0: \quad Z = W^2 \tag{6.1}$$

$$\mathcal{H}_1: \quad Z = (X+W)^2 + Y^2, \tag{6.2}$$

where W is the Weibull-distributed ground clutter, with PDF given by

$$f_W(w) = \left(\frac{\mu}{\lambda}\right)\left(\frac{w}{\lambda}\right)^{\mu-1} \exp\left[-\left(\frac{w}{\lambda}\right)^{\mu}\right], \quad w \geq 0 \tag{6.3}$$

in which $\mu > 0$ is the shape parameter and $\lambda > 0$ is the scale parameter. Additionally, X and Y are the in-phase and quadrature components of the target signal, with zero-mean Gaussian PDFs

$$f_X(x) = \frac{\exp\left(-\frac{x^2}{2\sigma^2}\right)}{\sqrt{2\pi}\sigma}, \quad -\infty \leq x \leq \infty \tag{6.4}$$

$$f_Y(y) = \frac{\exp\left(-\frac{y^2}{2\sigma^2}\right)}{\sqrt{2\pi}\sigma}, \quad -\infty \leq y \leq \infty \tag{6.5}$$

in which σ^2 is the target power per component. Note in (6.2) that, should there be no clutter interference, the PDF of the decision variable Z would follow an exponential distribution.

To the best of the authors' knowledge, no closed-form solutions exist for the statistics of Z as presented in (6.2). Herein, we solve this problem by deriving closed-form exact expressions for the PDF and CDF of Z. This is attained in the next section. Afterwards, as our primary aim, we obtain the corresponding PD for the investigated hypothesis test. Finally, we derive fast convergent series for the PDF, CDF, and PD, which alleviate computations.

6.3 Decision-Variable Statistics

We start by deriving the PDF and CDF of Z as in (6.2).

6.3.1 Probability Density Function

Let us define the following auxiliary random variables:

$$R \triangleq X + W \tag{6.6}$$

$$U \triangleq R^2 \tag{6.7}$$

$$V \triangleq Y^2. \tag{6.8}$$

Since the target signal and the clutter interference are independent random processes, we can express the sum statistics defined in (6.6) as a convolution [16], i.e.,

$$f_R(r) \triangleq \int_0^\infty f_X(r-\tau)\, f_W(\tau)\, \mathrm{d}\tau. \tag{6.9}$$

Substituting (6.3) and (6.4) in (6.9), and after some algebraic manipulations, we obtain

$$f_R(r) = \frac{\mu \exp\left(-\frac{r^2}{2\sigma^2}\right)}{\sqrt{2\pi}\sigma^2\lambda^\mu} \int_0^\infty \exp\left(-\frac{\tau^2}{2\sigma^2}\right) G_{0,1}^{1,0}\left[\begin{array}{c|c} - & \\ 0 & \end{array} - \frac{\tau r}{\sigma^2}\right] G_{0,1}^{1,0}\left[\begin{array}{c|c} - & \\ 0 & \end{array} \left(\frac{\tau}{\lambda}\right)^\mu\right] \mathrm{d}\tau, \tag{6.10}$$

where $G_{m,n}^{p,q}[\cdot]$ is the Meijer's G-function [17, Eq. (8.2.1.1)]. After making use of [18, Eq. (6.2.8)] and [19, Eq. (2.3)], followed by lengthy mathematical manipulations, a closed-form solution for (6.9) is obtained as

$$f_R(r) = \Psi_{f_R}\, \mathbf{H}\left[\mathbf{x}; (\delta, \mathbf{D}); (\beta, \mathbf{B}); \mathcal{L}_\mathbf{r}\right], \tag{6.11}$$

where $\Psi_{f_R} = \frac{\mu}{2\sigma^2}\left(\frac{\sqrt{2}\sigma}{\lambda}\right)^\mu \exp\left(-\frac{r^2}{2\sigma^2}\right)$, $\mathbf{x} = \left[-\frac{\sqrt{2}r}{\sigma}, \left(\frac{\sqrt{2}\sigma}{\lambda}\right)^\mu\right]$, $\delta = [0, 0, \frac{\mu}{2}]$, β is an empty vector, $\mathbf{B}$ is an empty matrix, $\mathcal{L}_\mathbf{r}$ is an appropriate contour on the complex plane (see Table 6.1), and $\mathbf{D} = \begin{pmatrix} 1 & 0 & -1/2 \\ 0 & 1 & -\mu/2 \end{pmatrix}^T$.

Table 6.1 – Integration paths for $\mathcal{L}_{\mathbf{r}}$, $\mathcal{L}_{\mathbf{u}}$ and $\mathcal{L}_{\mathbf{z}}$.

Contour	Integration Paths
$\mathcal{L}_{\mathbf{r}} = \mathcal{L}_{\mathbf{r,1}} \times \mathcal{L}_{\mathbf{r,2}}$	$\mathcal{L}_{\mathbf{r,1}}$ is a contour that separates the poles of $\Gamma(s_1)$ from those of $\Gamma\left(\frac{\mu-\mu s_2-s_1}{2}\right)$. $\mathcal{L}_{\mathbf{r,2}}$ is a contour that separates the poles of $\Gamma(s_2)$ from those of $\Gamma\left(\frac{\mu-\mu s_2-s_1}{2}\right)$.
$\mathcal{L}_{\mathbf{u}} = \mathcal{L}_{\mathbf{u,1}} \times \mathcal{L}_{\mathbf{u,2}}$	$\mathcal{L}_{\mathbf{u,1}}$ is a contour that separates the poles of $\Gamma(s_1)$ from those of $\Gamma\left(\frac{\mu-\mu s_2-s_1}{2}\right)$ and $\Gamma\left(\frac{1-s_1}{2}\right)$. $\mathcal{L}_{\mathbf{u,2}}$ is a contour that separates the poles of $\Gamma(s_2)$ from those of $\Gamma\left(\frac{\mu-\mu s_2-s_1}{2}\right)$.
$\mathcal{L}_{\mathbf{z}} = \mathcal{L}_{\mathbf{z,1}} \times \mathcal{L}_{\mathbf{z,2}} \times \mathcal{L}_{\mathbf{z,3}}$	$\mathcal{L}_{\mathbf{z,1}}$ is a contour that separates the poles of $\Gamma(s_1)$ from those of $\Gamma\left(\frac{\mu-\mu s_2-s_1}{2}\right)$, $\Gamma\left(\frac{1-s_1}{2}\right)$, and $\Gamma\left(\frac{-s_1+2s_3+2}{2}\right)$. $\mathcal{L}_{\mathbf{z,2}}$ is a contour that separates the poles of $\Gamma(s_2)$ from those of $\Gamma\left(\frac{\mu-\mu s_2-s_1}{2}\right)$. $\mathcal{L}_{\mathbf{z,3}}$ is a contour that separates the poles of $\Gamma(s_3)$ from those of $\Gamma\left(\frac{-s_1+2s_3+2}{2}\right)$.

Now, using (6.11) and [20, Eq. (1.112)], and after simplifications, we can compute the PDF of (6.7) through a transformation of variables as [16]

$$\begin{aligned} f_U(u) \triangleq & \left|\frac{\partial r^2}{\partial r}\right|^{-1} f_R(r)\Big|_{r=+\sqrt{u}} + \left|\frac{\partial r^2}{\partial r}\right|^{-1} f_R(r)\Big|_{r=-\sqrt{u}} \\ =& \Psi_{f_U}\left(\mathbf{H}\left[\mathbf{x}_{f_U}^{+};(\delta,\mathbf{D});(\beta,\mathbf{B});\mathcal{L}_{\mathbf{u}}\right] + \mathbf{H}\left[\mathbf{x}_{f_U}^{-};(\delta,\mathbf{D});(\beta,\mathbf{B});\mathcal{L}_{\mathbf{u}}\right]\right), \end{aligned} \tag{6.12}$$

where $\Psi_{f_U} = \frac{1}{4\sigma}\sqrt{\frac{\mu}{2\pi}}\left(\frac{\sqrt{2}\sigma}{\lambda}\right)^{\mu}\exp\left(-\frac{u}{2\sigma^2}\right)$, $\mathbf{x}_{f_U}^{+} = \left[\frac{\sqrt{2u}}{\sigma}, \left(\frac{\sqrt{2}\sigma}{\lambda}\right)^{\mu}\right]$, $\mathbf{x}_{f_U}^{-} = \left[\frac{-\sqrt{2u}}{\sigma}, \left(\frac{\sqrt{2}\sigma}{\lambda}\right)^{\mu}\right]$, and $\mathcal{L}_{\mathbf{u}}$ is an appropriate contour on the complex plane (see Table 6.1).

In a similar way, using (6.5) and after a simple transformation of variables, the PDF of (6.8) can be written as

$$f_V(v) = \frac{\exp\left(-\frac{v}{2\sigma^2}\right)}{\sqrt{2\pi v}\sigma}. \tag{6.13}$$

Finally, using (6.11), (6.12), (6.13), and [20, Eq. (1.86)], and taking into account that U and V are independent random variables, the PDF of (6.2) can be calculated in closed form as

$$\begin{aligned} f_Z(z|\mathcal{H}_1) \triangleq & \int_0^z f_U(z-\tau) f_V(\tau)\,\mathrm{d}\tau \\ =& \Psi_{f_Z}\left(\mathbf{H}\left[\mathbf{x}_{f_Z}^{+};(\delta_{f_Z},\mathbf{D}_{f_Z});(\beta_{f_Z},\mathbf{B}_{f_Z});\mathcal{L}_{\mathbf{u}}\right] + \mathbf{H}\left[\mathbf{x}_{f_Z}^{-};(\delta_{f_Z},\mathbf{D}_{f_Z});(\beta_{f_Z},\mathbf{B}_{f_Z});\mathcal{L}_{\mathbf{u}}\right]\right), \end{aligned} \tag{6.14}$$

where $\mathbf{x}_{f_Z}^{-} = \left[\frac{-\sqrt{2z}}{\sigma}, \left(\frac{\sqrt{2}\sigma}{\lambda}\right)^{\mu}\right]$, $\mathbf{x}_{f_Z}^{+} = \left[\frac{\sqrt{2z}}{\sigma}, \left(\frac{\sqrt{2}\sigma}{\lambda}\right)^{\mu}\right]$, $\Psi_{f_Z} = \frac{\mu}{8\sigma^2\sqrt{\pi}}\left(\frac{\sqrt{2}\sigma}{\lambda}\right)^{\mu}\exp\left(-\frac{z}{2\sigma^2}\right)$, $\delta_{f_Z} = \left[0,0,\frac{\mu}{2},\frac{1}{2}\right]$, $\beta_{f_Z} = [1]$, $\mathbf{B}_{f_Z} = \begin{pmatrix} -1 & 0 \end{pmatrix}$, and $\mathbf{D}_{f_Z} = \begin{pmatrix} 1 & 0 & -1/2 & -1/2 \\ 0 & 1 & -\mu/2 & 0 \end{pmatrix}^T$.

6.3.2 Cumulative Distribution Function

Using (6.14), [20, Eq. (1.62)], and [20, Eq. (1.86)], and after several mathematical manipulations, we obtain a closed-form expression for the corresponding CDF

of (6.2) as

$$\begin{aligned} F_Z\left(z|\mathcal{H}_1\right) \triangleq & \int_0^z f_Z\left(\nu|\mathcal{H}_1\right) \mathrm{d}\nu \\ =& \Phi_{F_Z}\left(\mathbf{H}\left[\mathbf{x}_{F_{Z,1}}^{+};\left(\delta_{f_Z},\mathbf{D}_{f_Z}\right);\left(\beta_{F_Z}^{+},\mathbf{B}_{F_Z}^{+}\right);\mathcal{L}_{\mathbf{u}}\right]+\mathbf{H}\left[\mathbf{x}_{F_{Z,1}}^{-};\left(\delta_{f_Z},\mathbf{D}_{f_Z}\right);\left(\beta_{F_Z}^{+},\mathbf{B}_{F_Z}^{+}\right);\mathcal{L}_{\mathbf{u}}\right]\right. \\ & \left.-\mathbf{H}\left[\mathbf{x}_{F_{Z,2}}^{+};\left(\delta_{F_Z},\mathbf{D}_{F_Z}\right);\left(\beta_{F_Z}^{-},\mathbf{B}_{F_Z}^{-}\right);\mathcal{L}_{\mathbf{z}}\right]-\mathbf{H}\left[\mathbf{x}_{F_{Z,2}}^{-};\left(\delta_{F_Z},\mathbf{D}_{F_Z}\right);\left(\beta_{F_Z}^{-},\mathbf{B}_{F_Z}^{-}\right);\mathcal{L}_{\mathbf{z}}\right]\right), \end{aligned} \tag{6.15}$$

where $\Phi_{F_Z}=\frac{\mu}{4\sqrt{\pi}}\left(\frac{\sqrt{2}\sigma}{\lambda}\right)^{\mu}$, $\mathbf{x}_{F_{Z,1}}^{+}=\left[2,\left(\frac{\sqrt{2}\sigma}{\lambda}\right)^{\mu}\right]$, $\mathbf{x}_{F_{Z,1}}^{-}=\left[-2,\left(\frac{\sqrt{2}\sigma}{\lambda}\right)^{\mu}\right]$, $\mathbf{x}_{F_{Z,2}}^{+}=\left[2,\left(\frac{\sqrt{2}\sigma}{\lambda}\right)^{\mu},\frac{z}{2\sigma^2}\right]$, $\mathbf{x}_{F_{Z,2}}^{-}=\left[-2,\left(\frac{\sqrt{2}\sigma}{\lambda}\right)^{\mu},\frac{z}{2\sigma^2}\right]$, $\delta_{F_Z}=\left[0,0,\frac{\mu}{2},\frac{1}{2},1,0\right]$, $\beta_{F_Z}^{+}$ is an empty vector, $\mathbf{B}_{F_Z}^{+}$is an empty matrix, $\beta_{F_Z}^{-}=[1,1]$, $\mathcal{L}_{\mathbf{z}}$ is an appropriate contour on the complex plane (see Table 6.1), $\mathbf{B}_{F_Z}^{-}=\begin{pmatrix}-1/2 & 0 & 0\\ 0 & 0 & 1\end{pmatrix}$, and $\mathbf{D}_{F_Z}=\begin{pmatrix}1 & 0 & -1/2 & -1/2 & -1/2 & 0\\ 0 & 1 & -\mu/2 & 0 & 0 & 0\\ 0 & 0 & 0 & 0 & 1 & 1\end{pmatrix}^{T}$.

6.4 Probability of Detection

The PFA and PD can be computed as the probability that the decision variable Z, defined respectively as in (6.1) and (6.2), falls above the decision threshold, say γ, i.e.,

$$P_{\mathrm{FA}} \triangleq \int_{\gamma}^{\infty} f_Z\left(z|\mathcal{H}_0\right)\,\mathrm{d}z \tag{6.16}$$

$$P_{\mathrm{D}} \triangleq \int_{\gamma}^{\infty} f_Z\left(z|\mathcal{H}_1\right)\,\mathrm{d}z. \tag{6.17}$$

After a simple transformation of variables, the PDF of (6.1) can be obtained from (6.3) as

$$f_Z\left(z|\mathcal{H}_0\right)=\frac{\mu}{2z}\left(\frac{\sqrt{z}}{\lambda}\right)^{\mu}\exp\left[-\left(\frac{\sqrt{z}}{\lambda}\right)^{\mu}\right], \tag{6.18}$$

which, when replaced into (6.16), leads to

$$P_{\mathrm{FA}}=\exp\left(-\gamma^{\mu/2}\lambda^{-\mu}\right). \tag{6.19}$$

As we are looking for a trade-off expression between PD and PFA, we now isolate γ in (6.19), yielding

$$\gamma=\left[-\lambda^{\mu}\ln(P_{\mathrm{FA}})\right]^{2/\mu}. \tag{6.20}$$

Finally, using (6.15), (6.17), (6.20), [18, Eq. (6.2.8)], and [17, Eq. (8.2.1.1)], followed by lengthy algebraic manipulations, we obtain PD in an exact closed form as

$$\begin{aligned} P_{\mathrm{D}}=1-\Phi_{F_Z}&\left(\mathbf{H}\left[\mathbf{x}_{F_{Z,1}}^{+};\left(\delta_{f_Z},\mathbf{D}_{f_Z}\right);\left(\beta_{F_Z}^{+},\mathbf{B}_{F_Z}^{+}\right);\mathcal{L}_{\mathbf{u}}\right]+\mathbf{H}\left[\mathbf{x}_{F_{Z,1}}^{-};\left(\delta_{f_Z},\mathbf{D}_{f_Z}\right);\left(\beta_{F_Z}^{+},\mathbf{B}_{F_Z}^{+}\right);\mathcal{L}_{\mathbf{u}}\right]\right. \\ &\left.-\mathbf{H}\left[\mathbf{x}_{P_{\mathrm{D}}}^{+};\left(\delta_{F_Z},\mathbf{D}_{F_Z}\right);\left(\beta_{F_Z}^{-},\mathbf{B}_{F_Z}^{-}\right);\mathcal{L}_{\mathbf{z}}\right]-\mathbf{H}\left[\mathbf{x}_{P_{\mathrm{D}}}^{-};\left(\delta_{F_Z},\mathbf{D}_{F_Z}\right);\left(\beta_{F_Z}^{-},\mathbf{B}_{F_Z}^{-}\right);\mathcal{L}_{\mathbf{z}}\right]\right), \end{aligned} \tag{6.21}$$

where $\mathbf{x}_{P_{\mathrm{D}}}^{+}=\left[2,\left(\frac{\sqrt{2}\sigma}{\lambda}\right)^{\mu},\frac{[-\lambda^{\mu}\ln(P_{\mathrm{FA}})]^{2/\mu}}{2\sigma^2}\right]$, and $\mathbf{x}_{P_{\mathrm{D}}}^{-}=\left[-2,\left(\frac{\sqrt{2}\sigma}{\lambda}\right)^{\mu},\frac{[-\lambda^{\mu}\ln(P_{\mathrm{FA}})]^{2/\mu}}{2\sigma^2}\right]$.

6.5 Alternative Series Representations

In order to ease the computation of our results, we now derive series representations for (6.14), (6.15), and (6.21). To do so, we exploit the orthogonal selection of poles in Cauchy's residue theorem [21]. Using the integration paths given in Table 6.1 and after an exhaustive analysis of residues, we concluded that the convergence of the series depends only on the shape parameter μ of the Weibull distribution, defined in (6.3). More specifically, the derived series representations will be split into the following scenarios: $\mu < 2$ and $\mu \geq 2$.

6.5.1 Probability Density Function

The series representation for (6.14) when $\mu < 2$ and $\mu \geq 2$ can be respectively expressed as

$$f_Z\left(z|\mathcal{H}_1;\mu<2\right) = \frac{\sqrt{\pi}\exp\left(-\frac{z}{2\sigma^2}\right)\ \Psi_{f_Z}}{\sigma^2}\sum_{l=0}^{\infty}\frac{(-1)^l\left(\frac{\sqrt{2}\sigma}{\lambda}\right)^{l\mu}\Gamma\left(\frac{l\mu}{2}+\frac{\mu}{2}\right)\ {}_1F_1\left(\frac{l\mu}{2}+\frac{\mu}{2};1;\frac{z}{2\sigma^2}\right)}{l!} \tag{6.22}$$

$$\begin{aligned} f_Z\left(z|\mathcal{H}_1;\mu\geq 2\right) =& \frac{\exp\left(-\frac{z}{2\sigma^2}\right)}{4\sigma^2}\sum_{k=0}^{\infty}\left\{\frac{\left[(-1)^k+1\right]\left(-\frac{2\sigma^2}{z}\right)^{\left\lfloor\frac{k}{2}\right\rfloor}\left(-\frac{2\sigma^2}{\lambda\sqrt{z}}\right)^{-k}}{\Gamma\left(\left\lfloor\frac{k}{2}\right\rfloor+1\right)}\right. \\ &\left.\times\,\Gamma\left(\frac{k}{\mu}+1\right)\ {}_2\tilde{F}_2\left(1,1-\left\lfloor\frac{k}{2}\right\rfloor;-\left\lfloor\frac{k}{2}\right\rfloor+\frac{k}{2},1-\left\lfloor\frac{k}{2}\right\rfloor+\frac{k}{2};\frac{z}{2\sigma^2}\right)\right\}, \end{aligned} \tag{6.23}$$

where ${}_1F_1\left(\cdot;\cdot;\cdot\right)$ is the Kummer confluent hypergeometric function [22, Eq. (13.1.2)] and ${}_2\tilde{F}_1(a,b;c,d;x) = {}_2F_1(a,b;c,d;x)/\Gamma(c)$ is the regularized Gauss hypergeometric function [22, Eq. (15.1.1)].

6.5.2 Cumulative Distribution Function

The series representation for (6.15) when $\mu < 2$ and $\mu \geq 2$ can be respectively expressed as

$$F_Z\left(z|\mathcal{H}_1;\mu<2\right) = \frac{\sqrt{\pi}z\Phi_{F_Z}}{\sigma^2}\sum_{l=0}^{\infty}\frac{(-1)^{-l}\left(\frac{\sqrt{2}\sigma}{\lambda}\right)^{l\mu}\Gamma\left(\frac{l\mu}{2}+\frac{\mu}{2}\right)\ {}_1F_1\left(-\frac{l\mu}{2}-\frac{\mu}{2}+1;2;-\frac{z}{2\sigma^2}\right)}{l!} \tag{6.24}$$

$$\begin{aligned} F_Z\left(z|\mathcal{H}_1;\mu\geq 2\right) =& \frac{2\sqrt{\pi}\ \Phi_{F_Z}}{\mu\left(\frac{\sqrt{2}\sigma}{\lambda}\right)^{\mu}}\sum_{k=0}^{\infty}\sum_{l=0}^{\infty}\left\{\frac{\left[(-1)^k+1\right](-1)^{k+l}\left(\frac{\sqrt{2}\sigma}{\lambda}\right)^{-k-2l}\Gamma\left(\frac{k}{\mu}+\frac{2l}{\mu}+1\right)}{l!\ \left[\Gamma\left(\frac{k}{2}+1\right)\right]^2}\right. \\ &\left.\times\,\Gamma\left(\frac{k}{2}+1,0,\frac{z}{2\sigma^2}\right)\right\}, \end{aligned} \tag{6.25}$$

where $\Gamma(\cdot,\cdot,\cdot)$ denotes the generalized incomplete gamma function [23, Eq. (8.2.3)].

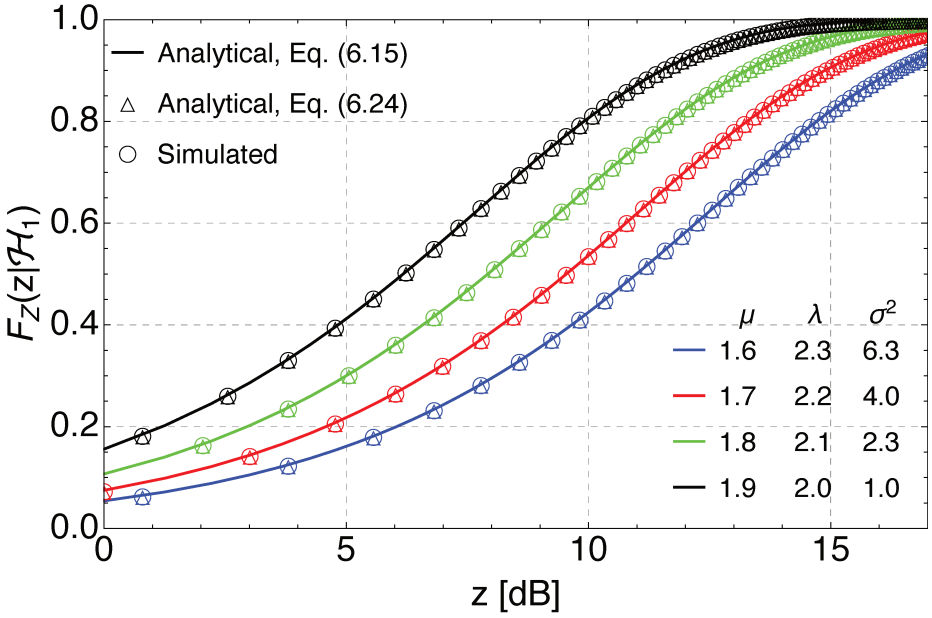

Figure 6.1 – Simulated and analytical CDFs of Z under hypothesis $\mathcal{H}_1$ and different values of $\mu < 2$, λ, and σ^2.

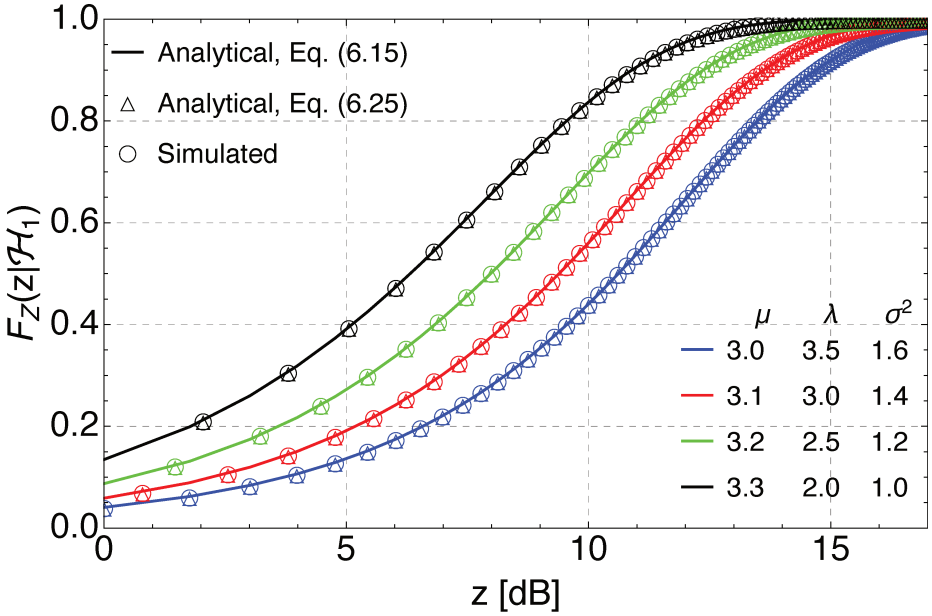

Figure 6.2 – Simulated and analytical CDFs of Z under hypothesis $\mathcal{H}_1$ and different values of $\mu \geq 2$, λ, and σ^2.

6.5.3 Probability of Detection

The series representation for (6.21) when $\mu < 2$ and $\mu \geq 2$ can be respectively expressed as

$$P_{\mathrm{D}_{\mu<2}} = 1 - \frac{\sqrt{\pi}\Phi_{F_Z}\left[-\lambda^{\mu}\ln(P_{\mathrm{FA}})\right]^{2/\mu}}{\sigma^2} \sum_{l=0}^{\infty} \left\{ \frac{(-1)^{-l}\left(\frac{\sqrt{2}\sigma}{\lambda}\right)^{l\mu}}{l!} \times {}_1F_1\left(-\frac{l\mu}{2} - \frac{\mu}{2} + 1; 2; -\frac{\left[-\lambda^{\mu}\ln(P_{\mathrm{FA}})\right]^{2/\mu}}{2\sigma^2}\right) \right\} \tag{6.26}$$

$$P_{\mathrm{D}_{\mu\geq2}} = 1 - \frac{1}{2}\sum_{k=0}^{\infty}\sum_{l=0}^{\infty} \left\{ \frac{\left[(-1)^k + 1\right](-1)^{-k-l}\left(\frac{\sqrt{2}\sigma}{\lambda}\right)^{-k-2l}\Gamma\left(\frac{k+2l+\mu}{\mu}\right)}{l!\ \left[\Gamma\left(\frac{k}{2}+1\right)\right]^2} \times \Gamma\left(\frac{k}{2}+1, 0, \frac{\left[-\lambda^{\mu}\ln(P_{\mathrm{FA}})\right]^{2/\mu}}{2\sigma^2}\right) \right\}. \tag{6.27}$$

It is worth mentioning that (6.22)–(6.27) are also original contributions of this work, proving to be highly efficient and computationally tractable, as illustrated in the next section.

6.6 Sample Numerical Results

In this section, we validate our analytical results by means of Monte-Carlo simulations.[2] In addition, we compare our results with those in [13], which are approximate, as explained in the Introduction. Here, (6.15) and (6.21) were computed using MATHEMATICA's built-in numerical integration.

Figs. 6.1 and 6.2 depict the analytical and simulated CDFs of Z under $\mathcal{H}_1$, for $\mu < 2$ and $\mu \geq 2$, respectively. The distribution parameters have been selected to show the broad range of shapes that the CDFs can exhibit. Note the perfect match between our analytical expressions and the simulation results.

Fig. 6.3 depicts P_{D} as a function of P_{FA} (analytical and simulated) for $\mu < 2$. To illustrate the validity of our expressions, we consider the following scenarios: (i) $\mu = 1.0$, $\lambda = 0.5$, and $\sigma^2 = 9.0$; (ii) $\mu = 1.0$, $\lambda = 0.5$, and $\sigma^2 = 7.5$; (iii) $\mu = 1.0$, $\lambda = 0.5$, and $\sigma^2 = 6.5$; and (iv) $\mu = 1.0$, $\lambda = 0.5$, and $\sigma^2 = 5.5$. Once again, note the perfect match between our analytical expressions and the simulation results. Also, note how the approximation in [13] departs from the true performance as the target's power (per component) σ^2 is increased.

[2] It is worth noting that the provided series converge quickly, requiring between 70 and 95 terms to achieve an accuracy of 10^{-5}. Besides, 10^7 system realizations were simulated for each sample scenario.

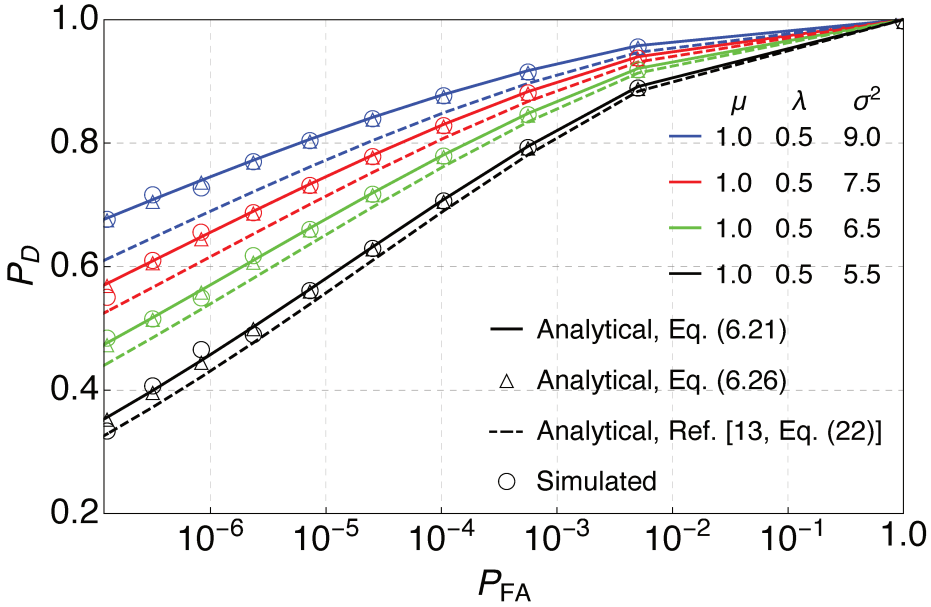

Figure 6.3 – Simulated and analytical PDs for different values of $\mu < 2$, λ, and σ^2.

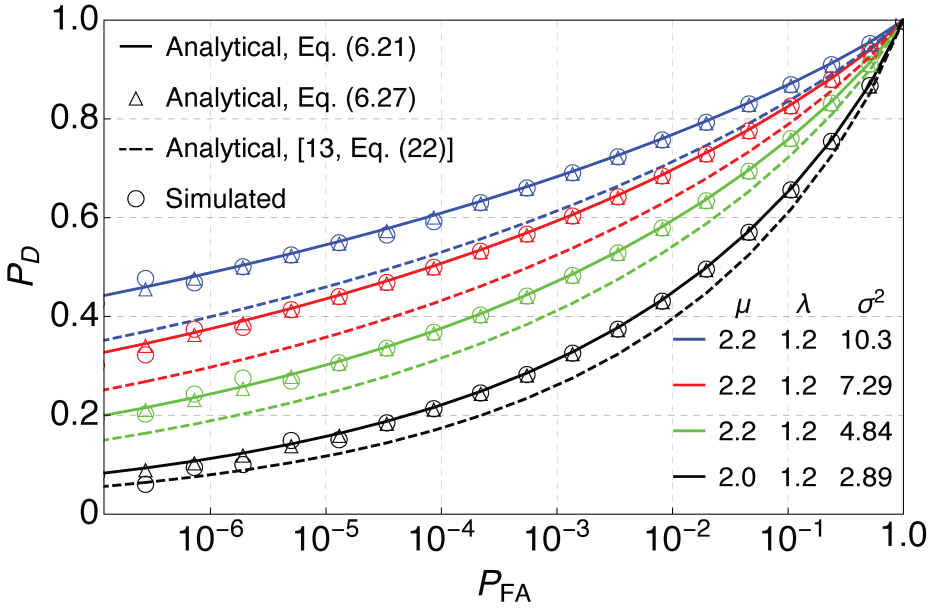

Figure 6.4 – Simulated and analytical PDs for different values of $\mu \geq 2$, λ, and σ^2.

Fig. 6.4 shows $P_{\rm D}$ as a function of $P_{\rm FA}$ (analytical and simulated) for $\mu \geq 2$. Here, we consider the following scenarios: (i) $\mu = 2.2$, $\lambda = 1.2$, and $\sigma^2 = 10.3$; (ii) $\mu = 2.2$, $\lambda = 1.2$, and $\sigma^2 = 7.29$; (iii) $\mu = 2.2$, $\lambda = 1.2$, and $\sigma^2 = 4.84$; and (iv) $\mu = 2.2$, $\lambda = 1.2$, and $\sigma^2 = 2.89$. As before, note the perfect match between our analytical expressions and the simulation results, and how the approximation in [13] departs from the true performance as the target's power (per component) σ^2 is increased.

6.7 Conclusions

In this work, we derived a closed-form exact expression for the probability of detection of a square-law radar receiver subject to an exponential target embedded in Weibull clutter — a plausible scenario in modern radar systems. Our solution is given in terms of the Fox H-function. Alternatively, we obtained a fast convergent series that can be executed quickly on an ordinary desktop computer. Monte-Carlo simulations validated the accuracy of our analytical expressions. Our exact approach avoided a common assumption that the target has a small power as compared to the clutter, explored elsewhere as an approximate solution.

6.8 Bibliography

[1] M. A. Richards, J. Scheer, W. A. Holm, and W. L. Melvin, *Principles of Modern Radar: Basic Principles*, 1st ed. West Perth, WA, Australia: SciTech, 2010.

[2] T. Bucciarelli, "CFAR problems in Weibull clutter," *Electron. Lett.*, vol. 21, no. 8, pp. 286–304, Apr. 1985.

[3] M. Sekine, S. Ohtani, T. Musha, T. Irabu, E. Kiuchi, T. Hagisawa, and Y. Tomita, "Weibull-distributed ground clutter," *IEEE Trans. Aerosp. Electron. Syst.*, vol. AES-17, no. 4, pp. 596–598, Jul. 1981.

[4] X. W. Meng, "Performance analysis of OS-CFAR with binary integration for Weibull background," *IEEE Trans. Aerosp. Electron. Syst.*, vol. 49, no. 2, pp. 1357–1366, Apr. 2013.

[5] A. Ephrath, Z. Eshcoli, and F. Berkowitz, "Probability of detection for $\mathcal{X}^2$ radar target in Weibull clutter," in *Proc. IEEE International Conference on Microwaves, Communications, Antennas and Electronic Systems (COMCAS)*, Tel Aviv, Israel, Nov 2011, pp. 1–5.

[6] A. Abbadi, H. Bouhedjeur, A. Bellabas, T. Menni, and F. Soltani, "Generalized closed-form expressions for CFAR detection in heterogeneous environment," *IEEE Geosci. Remote Sens. Lett.*, vol. 15, no. 7, pp. 1011–1015, Jul. 2018.

[7] M. Baadeche and F. Soltani, "Performance analysis of mean level constant false alarm rate detectors with binary integration in Weibull background," *IET Radar Sonar Navig.*, vol. 9, no. 3, pp. 233–240, Mar. 2015.

[8] D. M. Drumheller, "General expressions for Rician density and distribution functions," *IEEE Trans. Aerosp. Electron. Syst.*, vol. 29, no. 2, pp. 580–588, Apr. 1993.

[9] P. Swerling, "Probability of detection for fluctuating targets," *IRE Transactions on Information Theory*, vol. IT-6, pp. 269–308, Apr. 1960.

[10] H. Rohling, "Radar CFAR thresholding in clutter and multiple target situations," *IEEE Trans. Aerosp. Electron. Syst.*, vol. AES-19, no. 4, pp. 608–621, Jul. 1983.

[11] V. Anastassopoulos and G. A. Lampropoulos, "Optimal CFAR detection in Weibull clutter," *IEEE Trans. Aerosp. Electron. Syst.*, vol. 31, no. 1, pp. 52–64, Jan. 1995.

[12] D. C. Schleher, "Radar detection in Weibull clutter," *IEEE Trans. Aerosp. Electron. Syst.*, vol. AES-12, no. 6, pp. 736–743, Nov. 1976.

[13] F. D. G. Almeida, A. C. F. Rodriguez, G. Fraidenraich, and J. C. S. S. Filho, "CA-CFAR detection performance in homogeneous Weibull clutter," *IEEE Geosci. Remote Sens. Lett.*, vol. 16, no. 6, pp. 887–891, Jun. 2019.

[14] A. A. Nilsson and T. H. Glisson, "On the derivation and numerical evaluation of the Weibull-Rician distribution," *IEEE Trans. Aerosp. Electron. Syst.*, vol. AES-16, no. 6, pp. 864–867, Nov. 1980.

[15] R. Rifkin, "Analysis of CFAR performance in Weibull clutter," *IEEE Trans. Aerosp. Electron. Syst.*, vol. 30, no. 2, pp. 315–329, Apr. 1994.

[16] A. Papoulis, *Probability, Random Variables, and Stochastic Processes*, 4th ed. Ney York, NY, USA: McGraw-Hill, 2002.

[17] A. P. Prudnikov, Y. A. Bryčkov, and O. I. Maričev, *Integral and Series: Vol. 3*, 2nd ed., Fizmatlit, Ed. Moscow, Russia: Fizmatlit, 2003.

[18] M. D. Springer, *The Algebra of Random Variables*. New York, NY, USA: Wiley, 1979.

[19] P. K. Mittal and K. C. Gupta, "An integral involving generalized function of two variables," *Proc. Indian Acad. Sci.-Sec. A*, vol. 75, no. 3, pp. 117–123, Mar. 1972.

[20] A. M. Mathai, R. K. Saxena, and H. J. Haubold, *The H-function: Theory and Applications*. New York, NY, USA: Springer, 2009.

[21] E. Kreyszig, *Advanced Engineering Mathematics*, 10th ed. New Jersey, NJ, USA: John Wiley & Sons, 2010.

[22] F. W. J. Olver, D. W. Lozier, R. F. Boisvert, and C. W. Clark, *NIST Handbook of Mathematical Functions*, 1st ed. Washington, DC: US Dept. of Commerce: National Institute of Standards and Technology (NIST), 2010.

[23] M. Abramowitz and I. A. Stegun, *Handbook of Mathematical Functions with Formulas, Graphs, and Mathematical Tables*, 10th ed. Washington, DC: US Dept. of Commerce: National Bureau of Standards, 1972.

7 Contribution VI

This chapter is a replica of the paper below:

- F. D. A. García, A. S. Guerreiro, G. R. de Lima Tejerina, J. C. S. Santos Filho, G. Fraidenraich, and M. D. Yacoub, "Doppler estimation for high-velocity targets using subpulse processing and the Chinese remainder theorem", *IEEE Trans. Signal Process.*, under review, 2021. This work was partially published in the Proceedigs of the *53th IEEE Asilomar Conference on Signals, Systems, and Computers.*

Doppler Estimation for High-Velocity Targets Using Subpulse Processing and the Chinese Remainder Theorem

Fernando Darío Almeida García, André Saito Guerreiro, Gustavo Rodrigues de Lima Tejerina, José Cândido S. Santos Filho, Gustavo Fraidenraich, and Michel Daoud Yacoub

Abstract

In pulsed Doppler radars, the classic Chinese remainder theorem (CCRT) is a common method to resolve Doppler ambiguities caused by fast-moving targets. Another issue concerning high-velocity targets is related to the loss in the signal-to-noise ratio (SNR) after performing *range compression*. In particular, this loss can be partially mitigated by the use of subpulse processing (SP). Modern radars combine these techniques in order to reliably unfold the target velocity. However, the presence of background noise may compromise the Doppler estimates. Hence, a rigorous statistical analysis is imperative. In this work, we provide a comprehensive analysis on Doppler estimation. In particular, we derive novel closed-form expressions for the probability of detection (PD) and probability of false alarm (PFA). To this end, we consider the newly introduce SP along with the CCRT. A comparison analysis between SP and the classic pulse processing (PP) technique is also carried out. Numerical results and Monte-Carlo simulations corroborate the validity of our expressions and show that the SP–plus–CCRT technique helps to greatly reduce the PFA compared to previous studies, thereby improving radar detection.

7.1 Introduction

One important concern in modern pulsed radars is related to the Doppler frequency estimation of fast-velocity targets. Due to the high target's radial velocity, ambiguous estimates are more likely to occur. More specifically, ambiguous estimates appear whenever the target's Doppler shift is greater than the pulse repetition frequency (PRF) [1]. It seems obvious to think that increasing the PRF will overcome this problem. However, if we are interested in detecting targets located at long distances, then the PRF will be restricted to a maximum value. Therefore, the choice of PRF is a trade-off between range and Doppler requirements [2]. Fortunately, there are some techniques that can resolve ambiguities, although at the cost of extra measurement time and processing load. These techniques make use of multiples PRFs [3, 4, 5, 6, 7]. The most known and

used technique is the classic Chinese remainder theorem (CCRT). The CCRT is a fast and accurate method to resolve the unambiguous Doppler frequency. This is accomplished by solving a set of congruences, formed by the estimated measurements of each PRF [7, 8, 9]. Nevertheless, in this method, the number of PRFs will not be sufficient to resolve a certain quantity of targets. In general, L PRFs are required to successfully disambiguate $L-1$ targets. If the number of targets exceeds $L-1$, then *ghosts* can appear.[1] Unless additional data (e.g., tracking information) is available, the radar has no way of recognizing possible false detections [4]. Care must be taken in the analysis and design since the number of PRFs and the number of targets to be detected have a direct relationship.

Another issue concerning high-velocity targets is related to the signal-to-noise ratio (SNR) loss. This occurs because the Doppler shift of fast-moving targets will provoke a mismatch between the received signal and its replica [2]. Consequently, the SNR after *range compression* may be drastically reduced.[2] Some radar systems estimate and remove the Doppler shift prior to applying *range compression*. Nonetheless, some residual or uncompensated Doppler typically remains. This concern was partially alleviated in [11, 12]. Specifically, in [11], the authors proposed a subpulse processing (SP), which proved to have a higher Doppler tolerance,[3] increasing the ability to detect fast-moving targets. The shortcomings of SP are computation time (critical for most radars), processing load, and poor velocity resolution.

As stated before, the CCRT and SP have hardware and physical limitations when it comes to estimating high target velocities. In practice, modern pulsed radars take advantage of these two techniques so as to improve the system's capability to accurately detect the target's true Doppler frequency. Since SP the CCRT are affected by the presence of background noise, then a thorough statistical analysis involving these two estimation techniques must be carried out. Recently in [14], the authors proposed a novel expression for the probability to correctly estimate the unambiguous Doppler frequency considering the CCRT and the common pulse processing (PP) technique [2]. However, to the best of our knowledge, there is no performance analysis considering the SP–plus–CCRT technique.

The main objective of this research is to combine the statistical analysis conducted in [14] along with the newly introduced SP and the CCRT. To do so, we adopt a stochastic model that suits our Doppler estimation techniques. Then, we derive novel and closed-form expressions for: **i)** the probability to correctly estimate the Doppler frequency,

[1] *Ghosts* are false targets resulting from false coincidences of Doppler-ambiguous or range–ambiguous data [4].

[2] *Range compression* refers to the convolution operation between the received signal and the replica of the transmitted signal [10].

[3] Doppler tolerance refers to the degree of degradation in the compressed response due to uncompensated Doppler [13].

also called probability of detection (PD); and **ii)** the probability to erroneously estimate the Doppler frequency, also called probability of false alarm (PFA).

In what follows, $(a)\text{mod}(b)$ denotes the remainder of the euclidean division of a by b; $|\cdot|$, absolute value; $\lfloor\cdot\rfloor$, floor operation; round$(\cdot)$, rounding operation; $\Pr[\cdot]$, probability; $\mathbb{E}(\cdot)$, expectation; Var$(\cdot)$, variance; $(\cdot)^*$, complex conjugate; $\bigcap$, intersection of events; $\bigcup$, union of events; $\mathcal{N}(\mu, \sigma^2)$ denotes a Gaussian distribution with mean μ and variance σ^2; $\mathcal{N}_c(\mu, \sigma^2)$ denotes a complex Gaussian distribution with mean μ and variance σ^2, and $j = \sqrt{-1}$ is the imaginary unit.

7.2 Preliminaries

In this section, we present a brief introduction about the PP and SP techniques. Latter, we describe the basis to understand the CCRT algorithm. Finally, we show how the combined technique SP–plus–CCRT works in order to improve Doppler estimation.

7.2.1 Pulse Processing

PP is the common technique employed by the radar to estimate the target velocity and improve the SNR. In this processing technique, the radar transmits a sequence of M pulses during a coherent processing interval (CPI) [15]. Then, *range compression* is performed on each pulse to improve the radar's range resolution. Finally, the discrete Fourier transform (DFT) is applied along the slow-time samples to increase the SNR and to estimate the target Doppler frequency [2]. These samples are collected at a rate equal to the PRF. The maximum Doppler frequency shift that the radar manages to detect using PP is $\Psi_{max} = \pm\text{PRF}/2$. If the target Doppler frequency, f_d, exceeds this value, then the radar will deliver ambiguous Doppler measurements. The Doppler frequency shift will be positive for closing targets and negative for receding targets. The target velocity, v_t, and its corresponding Doppler shift are related by the following equation [16]:

$$f_d = \frac{2v_t f_R}{c} = \frac{2v_t}{\lambda}, \tag{7.1}$$

where f_R is the radar's operation frequency, c is the speed of light, and λ is the radar wavelength.

7.2.2 Subpulse Processing

SP improves Doppler tolerance by mitigating the loss in SNR caused by the uncompensated Doppler shift of fast-moving targets [2, 11]. Moreover, SP is used to overcome the problem of ambiguous Doppler measurements. The SP algorithm runs as follows:

1. First, the replica of the transmitted signal is divided into N subpulses – unlike PP that used the entire replica.

2. Latter, *range compression* is carried out between each subpulse and the received signal (cf. [11, 12] for a detailed discussion on this). The use of shorter replicas will enhance the system's Doppler tolerance [10], increasing the detection capability of fast-moving targets. Of course, this process leads to a reduction in the peak amplitude of the sub-compression response (by a factor of $1/N$). Here, the slow-time samples are collected at a rate of $\Phi = N/\tau$, where τ is the pulse width. It is important to emphasize that PP and SP are performed simultaneously, that is, for each of the M compressions, the radar carried out N sub-compressions [12].

3. Finally, the slow-time samples are coherently integrated to estimate the target Doppler frequency and to "restore" the peak amplitude of the sub-compression response.

The number of subpulses can be chosen as high as needed, as long as it is taken into consideration that each additional subpulse requires an extra *range compression* operation, increasing the computational load and computation time. The maximum Doppler frequency shift that the radar can now manage to detect is $\Phi_{max} = \pm N/2\tau$ [11]. Since $\Phi_{max} > \Psi_{max}$, SP provides a higher frequency range of detection for fast-moving targets.

Computation time is critical for most radars and depends strongly on the radar's operation mode (e.g. tracking, searching or imaging), thereby limiting the number of subpulses. Commonly, the number of subpulses is set between 5 and 10. However, this small number yields to a poor discretization in the frequency domain and, consequently, producing inaccurate estimates.

7.2.3 Classic Chinese Remainder Theorem

The use of multiples PRFs is a common approach to resolve range and Doppler ambiguities [3, 8, 17, 4]. In this work, we only focus on solving Doppler ambiguities. Consider for the moment a target with Doppler shift $f_d > \Psi_{max}$. In this scenario, the radar will detect the target with an apparent Doppler shift, $f_{d_{ap}}$, that satisfies

$$f_d = f_{d_{ap}} + n\text{PRF}, \tag{7.2}$$

where n is some integer. It is convenience to express the target's Doppler shift f_d in terms of its corresponding Doppler bin, b_d. Thus, (7.2) becomes

$$b_d = b_{ap} + nM, \tag{7.3}$$

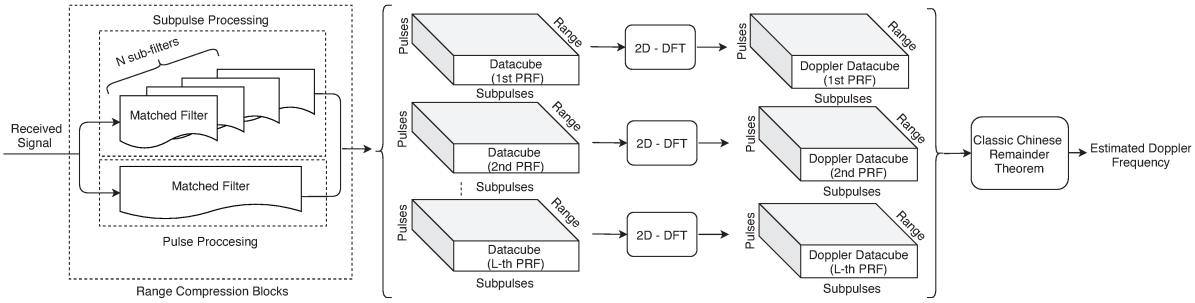

Figure 7.1 – Block diagram for Doppler estimation.

in which $b_{ap} \in \{0, 1, 2, \ldots, M-1\}$ is the apparent Doppler bin, defined as

$$b_{ap} = \left\lfloor \left| \frac{f_{d_{ap}}}{\Delta D} \right| \right\rfloor, \qquad f_{d_{ap}} \geq 0 \tag{7.4}$$

$$b_{ap} = M - \left\lfloor \left| \frac{f_{d_{ap}}}{\Delta D} \right| \right\rfloor, \qquad f_{d_{ap}} < 0 \tag{7.5}$$

with $\Delta D = \text{PRF}/M$ being the Doppler bin spacing. Under this scenario, the radar is incapable to detect the target's true Doppler frequency.

Now, suppose that we have L PRFs. Then, the unambiguous target's Doppler bin must satisfies the following congruences:

$$b_d \equiv b_{ap_i} + n_i M_i, \qquad 1 \leq i \leq L \tag{7.6}$$

The CCRT states that if all PRFs are pairwisely coprimes, then the set of congruences in (7.6) will have a unique solution given by [17, 4, 18]

$$b_d = \left(\sum_{i=1}^{L} b_{ap_i} \beta_i \right) \bmod (\Theta), \tag{7.7}$$

where $\Theta = \prod_{i=1}^{L} M_i$, $\beta_i = b_i \Theta / \text{PRF}_i$, and b_i is the smaller integer which can be computed by solving the following expression:

$$\left(\frac{b_i \Theta}{M_i} \right) \bmod (M_i) = 1. \tag{7.8}$$

7.2.4 Doppler Estimation

Fig. 7.1 depicts the entire block diagram for Doppler estimation. First, the received signal passes through two types of independent *range compression* blocks, one for PP and one for SP. This process is performed in sequence for each pulse repetition interval (PRI). The outputs of both blocks are combined and stored in memory to form a datacube [2]. (The datacube's data is organized by range, number of pulses, and number of subpulses.) More datacubes are needed when using more than one PRF, as shown in Fig. 7.1. Next, a 2D-DFT block is applied to each datacube to perform coherent integration. (The 2D-DFT block is referred to as a two-dimensional DFT applied along with

pulses and subpulses.) Latter, the output of the 2D-DFT block is a matrix with the same size containing the estimated Doppler shifts. This new matrix is referred to as Doppler datacube. Finally, the CCRT is applied over the Doppler datacubes. This process will be clarified in Section 7.5 by means of simulation.

Noise, jammer, and clutter are major concerns in all radar systems. In this work, we consider the presence of additive complex white Gaussian noise (CWGN). Thus, the Doppler spectrum of fast moving targets will be compromised due to the intrinsic characteristics of noise. For example, a high noise power could mask small target returns, degrading radar performance. Even if the target return is entirely deterministic, the combined signal (target–plus–noise) is a random process and must be treated as such. Therefore, we need to assess the statistics underlying Doppler analysis, but first, we need to come up with a specific stochastic model that suits the requirements and design of our radar's estimation scheme. This is discussed in the next section.

7.3 System Model

In this section, we propose a stochastic model that fits our signal processing schemes. In addition, we describe the premises (hypotheses) used for Doppler estimation.

According to Sections 7.2.1 and 7.2.2, the collected signals in the slow-time domain corresponding to PP and SP can be expressed, respectively, as

$$\begin{aligned} g_1[m] &= s_1[m] + w_1[m] \\ &= a_1 \exp(j2\pi f_d m/\mathrm{PRF}) + w_1[m], \quad 0 \le m \le M-1 \end{aligned} \tag{7.9}$$

$$\begin{aligned} g_2[n] &= s_2[n] + w_2[n] \\ &= a_2 \exp(j2\pi f_d n/\Phi) + w_2[n], \qquad 0 \le n \le N-1 \end{aligned} \tag{7.10}$$

where $s_1[m]$ and $s_2[n]$ are discrete complex sine signals[4] originated by changes in the target position; $w_1[m]$ and $w_2[n]$ are discrete additive complex Gaussian noises; and finally, a_1 and a_2 are the amplitudes at the output of the matched filters. Depending on the target velocity, the output amplitudes a_1 and a_2 maybe be greatly attenuated. However, the attenuation in a_2 is partially mitigated by the use of SP. In particular, it follows that $a_2 > a_1$ for high-velocity targets [11]. Additionally, we define $2\sigma_{t_1}^2$ and $2\sigma_{t_2}^2$ as the total mean powers – in the time domain – for $w_1[m]$ and $w_2[n]$, respectively. As seen in practice, and due to the stationary characteristic of noise, we have that $\sigma_{t_1}^2 = \sigma_{t_2}^2$ [19]. However, we will remain using separate notations for $\sigma_{t_1}^2$ and $\sigma_{t_2}^2$ so as to distinguish the

[4] In most systems, the radio frequency (RF) signal is mixed to baseband prior to compression, and a coherent detector is used in the downconversion process to form in-phase (I) and quadrature (Q) receive channels, thereby creating a complex baseband signal.

noise power from PP and SP. Of course, these separate notations will not alter, in any form, our performance analysis.

The SNR measured in the time domain considering PP and SP, can be expressed, respectively, as

$$\mathrm{SNR}_{t_1} = \frac{|a_1|^2}{2\sigma_{t_1}^2} \tag{7.11}$$

$$\mathrm{SNR}_{t_2} = \frac{|a_2/N|^2}{2\sigma_{t_2}^2}. \tag{7.12}$$

Observe in (7.12) that the fact of dividing the replica into N subpulses causes a reduction in the SNR by a factor of $1/N^2$, as mentioned in Section 7.2.2.

The DFT is the primary operation to implement coherent integration. More precisely, the DFT provides a mechanism to test multiple candidate frequencies to maximize the *integration gain* [2]. The corresponding DFTs for (7.9) and (7.10) are given, respectively, by

$$\begin{aligned} G_1[k'] &\triangleq \mathscr{F}\{g_1[m]\} \\ &= \sum_{m=0}^{M-1} g_1[m] \exp(-j2\pi k'm/M) \\ &= S_1[k'] + W_1[k'], \quad 0 \le k' \le M-1 \end{aligned} \tag{7.13}$$

$$\begin{aligned} G_2[l'] &\triangleq \mathscr{F}\{g_2[n]\} \\ &= \sum_{n=0}^{N-1} g_2[n] \exp(-j2\pi l'n/N) \\ &= S_2[l'] + W_2[l'], \qquad 0 \le l' \le N-1 \end{aligned} \tag{7.14}$$

The SNR measured in the frequency domain considering PP and SP, are given, respectively, by [2, Eq. (17.37)]

$$\mathrm{SNR}_1 = \frac{|Ma_1|^2}{2\sigma_1^2} \tag{7.15}$$

$$\mathrm{SNR}_2 = \frac{|a_2|^2}{2\sigma_2^2}, \tag{7.16}$$

in which $\sigma_1^2 = M\sigma_{t_1}^2$ and $\sigma_2^2 = N\sigma_{t_1}^2$ are half of the noise powers – in the frequency domain – for $W_1[k']$ and $W_2[l']$, respectively.

The Doppler estimates are based on the absolute values of $G_1[k']$ and $G_2[l']$. That is, (7.13) and (7.14) will provide estimates for f_d, say $\hat{f}_1$ and $\hat{f}_2$, by searching k' and l', in which the absolute values of $G_1[k']$ and $G_2[l']$ are maximum. It is worth mentioning that if $\Psi_{max} < f_d$ and $\Phi_{max} < f_d$, then $\hat{f}_1$ and $\hat{f}_2$ will display ambiguous Doppler estimates.

Now, considering L PRFs (say, $\mathrm{PRF}_1, \ldots, \mathrm{PRF}_L$), we can define the absolute values for $G_1[k']$ and $G_2[l']$ at the i-th PRF, respectively, as

$$H_{1,i}[k'] \triangleq |G_{1,i}[k']| \qquad 0 \leq k' \leq M_i - 1 \tag{7.17}$$

$$H_{2,i}[l'] \triangleq |G_{2,i}[l']| \qquad 0 \leq l' \leq N_i - 1 \tag{7.18}$$

where the subscript $i \in \{1, \ldots, L\}$ denotes the association to the i-th PRF.

Herein, we assume that $G_{1,i}[k']$ is composed of $M_i - 1$ independent and identically distributed noise samples and one target–plus–noise sample, denoted as $\mathcal{G}_{1,i}$. On the other hand, $G_{2,i}[l']$ is composed of $N_i - 1$ independent and identically distributed noise samples and one combined sample, denoted as $\mathcal{G}_{2,i}$. The target–plus–noise samples $\mathcal{G}_{1,i}$ and $\mathcal{G}_{2,i}$ can be modeled, respectively, by [20, Eq. (1)]

$$\mathcal{G}_{1,i} = \sigma_{1,i}\left(\sqrt{1-\lambda_{1,i}^2}A_{1,i} + \lambda_{1,i}A_{0,i}\right) + j\sigma_{1,i}\left(\sqrt{1-\lambda_{1,i}^2}B_{1,i} + \lambda_{1,i}B_{0,i}\right) \tag{7.19}$$

$$\mathcal{G}_{2,i} = \sigma_{2,i}\left(\sqrt{1-\lambda_{2,i}^2}A_{2,i} + \lambda_{2,i}A_{0,i}\right) + j\sigma_{2,i}\left(\sqrt{1-\lambda_{2,i}^2}B_{2,i} + \lambda_{2,i}B_{0,i}\right), \tag{7.20}$$

where $A_{p,i}$ and $B_{p,i}$ $(p = 1, 2)$ are mutually independent random variables (RVs) distributed as $\mathcal{N}(0, \frac{1}{2})$, and $\lambda_{p,i}, \in (0, 1]$. Then, for any p and q $(q = 1, 2)$, it follows that $\mathbb{E}(A_{p,i}B_{q,i}) = 0$ and $\mathbb{E}(A_{p,i}A_{q,i}) = \mathbb{E}(B_{p,i}B_{q,i}) = \frac{1}{2}\delta_{pq}$. ($\delta_{pq} = 1$ if $p = q$, and $\delta_{pq} = 0$ otherwise.) In addition, $A_{0,i}$ and $B_{0,i}$ are mutually independent RVs distributed as $\mathcal{N}(m_{\mathbf{Re},i}, \frac{1}{2})$ and $\mathcal{N}(m_{\mathbf{Im},i}, \frac{1}{2})$, respectively. Thus, $\mathcal{G}_{1,i}$ and $\mathcal{G}_{2,i}$ are non-zero mean complex Gaussian RVs with probability density functions (PDFs) given, respectively, by $\mathcal{N}_c(\lambda_{1,i}(m_{\mathbf{Re},i} + jm_{\mathbf{Im},i}), \sigma_{1,i}^2)$ and $\mathcal{N}_c(\lambda_{2,i}(m_{\mathbf{Re},i} + jm_{\mathbf{Im},i}), \sigma_{2,i}^2)$. The correlation coefficient between any pair of $(\mathcal{G}_{1,i}, \mathcal{G}_{2,i})$, can be calculated as [20, Eq. (2)]

$$\begin{aligned}\rho_{kl,i} &\triangleq \frac{\mathbb{E}(\mathcal{G}_{1,i}\mathcal{G}_{2,i}^*) - \mathbb{E}(\mathcal{G}_{1,i})\mathbb{E}(\mathcal{G}_{2,i}^*)}{\sqrt{\mathrm{Var}(\mathcal{G}_{1,i})\mathrm{Var}(\mathcal{G}_{2,i})}} \\ &= \lambda_{1,i}\lambda_{2,i}.\end{aligned} \tag{7.21}$$

This correlation exists because both PP and SP use the same received signal when performing *range compression* [2]. Observe that the parameters $\lambda_{1,i}^2$, $\lambda_{2,i}^2$, $m_{\mathbf{Re},i}$ and $m_{\mathbf{Im},i}$ can be used to model the compressed responses $|M_i a_{1,i}|^2$ and $|a_{2,i}|^2$. This can be done by making the following substitutions: $|M_i a_{1,i}|^2 = \lambda_{1,i}^2(m_{\mathbf{Re},i}^2 + m_{\mathbf{Im}}^2)$ and $|a_{2,i}|^2 = \lambda_{2,i}^2(m_{\mathbf{Re},i}^2 + m_{\mathbf{Im}}^2)$. On the other hand, $\lambda_{1,i}$ and $\lambda_{2,i}$ can be chosen to meet a desire correlation coefficient.

By the above, it follows that $H_{1,i}[k']$ is composed of $M_i - 1$ Rayleigh distributed samples, denoted as $X_{k,i}$ $(k \in \{1, 2, \ldots, M_i - 1\})$, and one Rice distributed sample, denoted as $R_{1,i}$. Similarly, $H_{2,i}[l']$ is composed of $N_i - 1$ Rayleigh distributed samples, denoted as $Y_{l,i}$ $(l \in \{1, 2, \ldots, N_i - 1\})$, and one Rice distributed sample, denoted as $R_{2,i}$.

The PDFs of $X_{k,i}$ and $Y_{l,i}$ are given, respectively, by

$$f_{X_{k,i}}(x_{k,i}) = \frac{x_{k,i} \exp\left(-\frac{x_{k,i}^2}{2\sigma_{k,i}^2}\right)}{\sigma_{k,i}} \tag{7.22}$$

$$f_{Y_{l,i}}(y_{l,i}) = \frac{y_{l,i} \exp\left(-\frac{y_{l,i}^2}{2\sigma_{l,i}^2}\right)}{\sigma_{l,i}}. \tag{7.23}$$

Moreover, since $R_{1,i}$ and $R_{2,i}$ bear a certain degree of correlation, they are governed by a bivariate Rician distribution, given by [20, 21]

$$f_{R_{1,i},R_{2,i}}(r_{1,i}, r_{2,i}|\mathcal{H}_1) = \int_0^\infty \exp(-t\xi_i) \exp(-\mathbf{m}_i) I_0\left(2\sqrt{\mathbf{m}_i t}\right) \prod_{p=1}^{2} \frac{r_{p,i}}{\Omega_{p,i}^2} \times \exp\left(-\frac{r_{p,i}^2}{2\Omega_{p,i}^2}\right) I_0\left(\frac{r_{p,i}\sqrt{t\sigma_{p,i}^2\lambda_{p,i}^2}}{\Omega_{p,i}^2}\right) \mathrm{d}t, \tag{7.24}$$

where $I_0(\cdot)$ is the modified Bessel function of the first kind and order zero [22, Eq. (9.6.16)], $\mathbf{m}_i = m_{\mathbf{Re},i}^2 + m_{\mathbf{Im},i}^2$, and

$$\Omega_{p,i}^2 = \sigma_{p,i}^2 \left(\frac{1-\lambda_{p,i}^2}{2}\right) \tag{7.25a}$$

$$\xi_i = 1 + \sum_{p=1}^{2} \frac{\sigma_{p,i}^2 \lambda_{p,i}^2}{2\Omega_{p,i}^2}. \tag{7.25b}$$

7.4 Doppler Analysis

In this section, we provide a comprehensive statistical analysis on Doppler estimation. To do so, we derive the performance metrics for both SP and SP–plus–CCRT.

7.4.1 SP Analysis

First, let us define the following events:

$$\mathcal{A}_{k,i} = \{R_{1,i} > X_{k,i}\} \tag{7.26}$$

$$\mathcal{B}_{l,i} = \{R_{2,i} > Y_{l,i}\} \tag{7.27}$$

$$\mathcal{C}_{k,i} = \{X_{k,i} > R_{1,i}\} \tag{7.28}$$

$$\mathcal{D}_{l,i} = \{Y_{l,i} > R_{2,i}\}. \tag{7.29}$$

Proposition I. *Let PD_i be the probability of detection at the i-th PRF. Specifically, PD_i is defined as the probability that $R_{1,i}$ is greater than $X_{k,i}$ and, simultaneously, that $R_{2,i}$ is greater than $Y_{l,i}$, i.e.,*

$$PD_i \triangleq Pr\left[\left(\bigcap_{k=1}^{M_i-1} \mathcal{A}_{k,i}\right) \bigcap \left(\bigcap_{l=1}^{N_i-1} \mathcal{B}_{l,i}\right)\right]. \tag{7.30}$$

Then, from (7.22)–(7.24), (7.30) *can be expressed in closed form as*

$$PD_i = \sum_{k=0}^{M_i-1} \sum_{l=0}^{N_i-1} \left(\begin{array}{c} M_i - 1 \\ k \end{array} \right) \left(\begin{array}{c} N_i - 1 \\ l \end{array} \right) \frac{(-1)^{-k-l+M_i+N_i} \mathcal{V}_i(k,l)}{\mathcal{U}_i(k,l)} \exp\left(-\boldsymbol{m}_i + \frac{\boldsymbol{m}_i}{\mathcal{U}_i(k,l)} \right), \tag{7.31}$$

wherein $\mathcal{U}_i(k,l)$ *and* $\mathcal{V}_i(k,l)$ *are auxiliary functions defined, respectively, as*

$$\mathcal{U}_i(k,l) = \xi_i - \frac{\xi_i \lambda_{1,i}^2 \sigma_{1,i}^4}{2\Omega_{1,i}^2 \left(\Omega_{1,i}^2 (k - M_i + 1) - \sigma_{1,i}^2 \right)} - \frac{\xi_i \lambda_{2,i}^2 \sigma_{2,i}^4}{2\Omega_{2,i}^2 \left(\Omega_{2,i}^2 (l - N_i + 1) - \sigma_{2,i}^2 \right)} \tag{7.32a}$$

$$\mathcal{V}_i(k,l) = \frac{\sigma_{1,i}^2 \sigma_{2,i}^2}{\left(\Omega_{1,i}^2 (-k + M_i - 1) + \sigma_{1,i}^2 \right) \left(\Omega_{2,i}^2 (-l + N_i - 1) + \sigma_{2,i}^2 \right)}. \tag{7.32b}$$

Proof. See Appendix D.1. ■

Corollary I. *Let* PFA_i *be the probability of false alarm at the* i*-th PRF. More precisely,* PFA_i *is defined as the probability that at least one of* $X_{k,i}$ *is greater than* $R_{1,i}$ *and, simultaneously, that at least one of* $Y_{l,i}$ *is greater than* $R_{2,i}$*, i.e.,*

$$PFA_i \triangleq Pr\left[\bigcup_{k=1}^{M_i-1} \bigcup_{l=1}^{N_i-1} \left(\mathcal{C}_{k,i} \bigcap \mathcal{D}_{l,i} \right) \right]. \tag{7.33}$$

Then, from (7.22)–(7.24), (7.33) *can be written in closed form as*

$$\begin{aligned} PFA_i = & \frac{(M_i - 1)(N_i - 1)\, \mathcal{Q}_i(1,1)}{\mathcal{P}_i(1,1)} \exp\left(-\boldsymbol{m}_i + \frac{\boldsymbol{m}_i}{\mathcal{P}_i(1,1)} \right) - \binom{M_i - 1}{2} \binom{N_i - 1}{2} \\ & \times \frac{\mathcal{Q}_i(2,2)}{\mathcal{P}_i(2,2)} \exp\left(-\boldsymbol{m}_i + \frac{\boldsymbol{m}_i}{\mathcal{P}_i(2,2)} \right) + \cdots + (-1)^{M_i - N_i - 1} \frac{\mathcal{Q}_i(M_i - 1, N_i - 1)}{\mathcal{P}_i(M_i - 1, N_i - 1)} \\ & \times \exp\left(-\boldsymbol{m}_i + \frac{\boldsymbol{m}_i}{\mathcal{P}_i(M_i - 1, N_i - 1)} \right) \end{aligned} \tag{7.34}$$

where $\mathcal{P}_i(k,l)$ *and* $\mathcal{Q}_i(k,l)$ *are auxiliary functions defined, respectively, by*

$$\mathcal{P}_i(k,l) = \xi_i - \frac{\lambda_{1,i}^2 \sigma_{1,i}^4}{2\Omega_{1,i}^2 \left(k\ \Omega_{1,i}^2 + \sigma_{1,i}^2 \right)} - \frac{\lambda_{2,i}^2 \sigma_{2,i}^4}{2\Omega_{2,i}^2 \left(l\ \Omega_{2,i}^2 + \sigma_{2,i}^2 \right)} \tag{7.35a}$$

$$\mathcal{Q}_i(k,l) = \frac{\sigma_{1,i}^2 \sigma_{2,i}^2}{\left(k\ \Omega_{1,i}^2 + \sigma_{1,i}^2 \right) \left(l\ \Omega_{2,i}^2 + \sigma_{2,i}^2 \right)}. \tag{7.35b}$$

Proof. See Appendix D.2. ■

It is worth mentioning that (7.31) and (7.34) are novel and original contributions of this work, derived in closed form even though (7.24) is given in integral form.

7.4.2 SP–Plus–CCRT Analysis

Similar to [14], we assume that each individual pulse on each sweep results in an independent random value for the target returns.

Now, using (7.31) and taking into account the $\mathcal{M}$–of–L detection criterion,[5] the probability of detection for the combined technique SP–plus–CCR can be calculated as follows [23]

$$\mathrm{PD}_{\mathrm{CCRT}} \triangleq \sum_{l=\mathcal{M}}^{L} \sum_{\mathcal{E}\in\mathcal{F}_l} \left\{ \left(\prod_{i\in\mathcal{E}} \mathrm{PD}_i \right) \left(\prod_{j\in\mathcal{E}^c} (1-\mathrm{PD}_j) \right) \right\}, \tag{7.36}$$

where $\mathcal{F}_l$ is the set of all subsets of l integers that can be selected from $\{1, 2, \ldots, L\}$, and $\mathcal{E}^c$ is the complement of $\mathcal{E}$. For example, if $l = 2$ and $L = 3$, then $\mathcal{F}_2 = \{\{1,2\}, \{1,3\}, \{2,3\}\}$, and $\mathcal{E}^c = \{1, 2, \ldots, L\} \setminus \mathcal{E}$.

On the other hand, the probability of false alarm for the combined technique SP–plus-CCRT can be calculated as [23]

$$\mathrm{PFA}_{\mathrm{CCRT}} \triangleq \sum_{l=\mathcal{M}}^{L} \sum_{\mathcal{E}\in\mathcal{F}_l} \left\{ \left(\prod_{i\in\mathcal{E}} \mathrm{PFA}_i \right) \left(\prod_{j\in\mathcal{E}^c} (1-\mathrm{PFA}_j) \right) \right\}. \tag{7.37}$$

For the case where $\mathcal{M} = L$, (7.36) and (7.37) reduce, respectively, to

$$\mathrm{PD}_{\mathrm{CCRT}} = \prod_{i=1}^{L} \mathrm{PD}_i \tag{7.38}$$

$$\mathrm{PFA}_{\mathrm{CCRT}} = \prod_{i=1}^{L} \mathrm{PFA}_i. \tag{7.39}$$

7.5 Numerical Results

In this section, we illustrate through Figs. 7.2 and 7.3 how the Doppler estimation process is carried out. Latter, we validate our derived expressions by means of Monte-Carlo simulations[6]. To do so, we make use of the following radar setup: $\mathrm{PRF}_1 = 700$ [Hz], $\mathrm{PRF}_2 = 1100$ [Hz], $\mathrm{PRF}_3 = 1300$ [Hz], $\mathrm{PRF}_4 = 1700$ [Hz], $L = \mathcal{M} = 4$, $f_R = 6$ [GHz], $\tau = 25$ [μs], $\lambda = 0.05$ [m], $M_1 = 11$, $M_2 = 13$, $M_3 = 17$, $M_4 = 19$, and $N_i = 8\ \forall i \in \{1, 2, 3, 4\}$. In addition, we consider a linear frequency-modulated pulse with bandwidth $B = 2$ [MHz].

Figs. 7.2 and 7.3 illustrate the output data after the 2D-DFT blocks. In this simulation example, we placed a target at an initial range of 10 [Km], traveling with a

[5] Instead of detecting a target on the basis of at least one detection in L tries, system designers often require that some number $\mathcal{M}$ or more detections be required in L tries before a target detection is accepted [2].

[6] The number of realizations in Monte-Carlo simulations was set to 10^6.

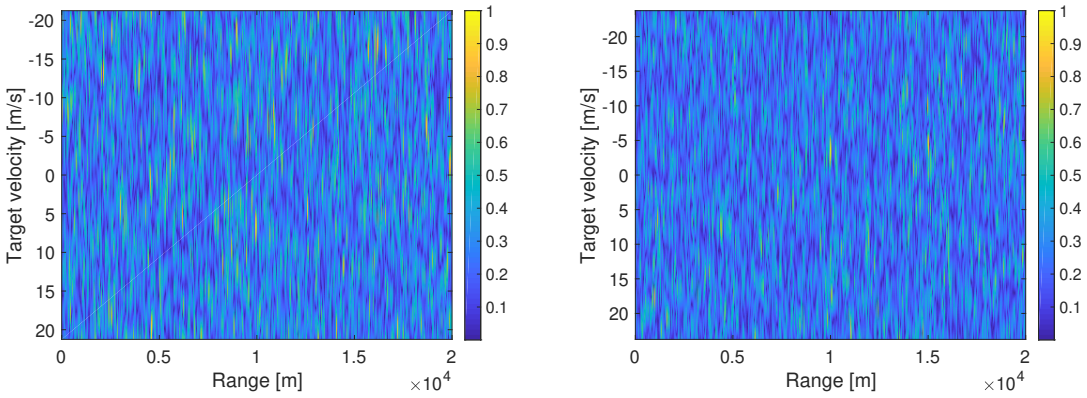

(a–1) $\mathrm{PRF}_1 = 1700$ [Hz], $M_1 = 11$

(a–2) $\mathrm{PRF}_2 = 1900$ [Hz], $M_2 = 13$

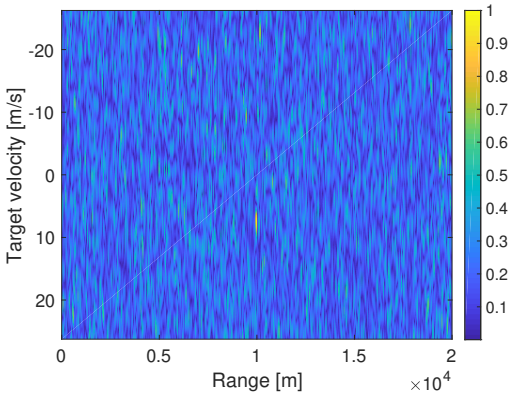

(a–3) $\mathrm{PRF}_3 = 2100$ [Hz], $M_3 = 17$

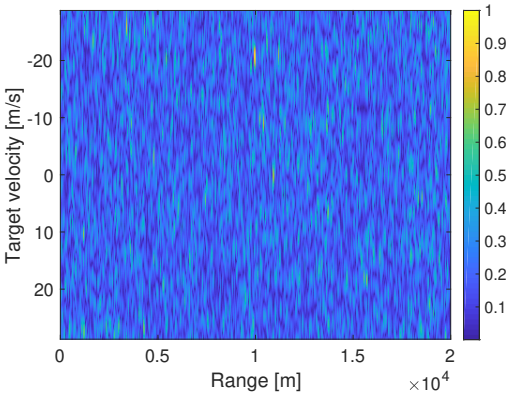

(a–4) $\mathrm{PRF}_4 = 2300$ [Hz], $M_4 = 19$

Figure 7.2 – Velocity versus range: normalized output data using pulse information.

constant velocity of $v_t = 300$ m/s in the opposite direction of the radar (i.e., the target is receding).

Fig. 7.2 shows the normalized output data – Velocity vs Range – using only pulse information. Observe that in all 4 scenarios, the target at 10 [Km] is unlikely to be detected due to the high loss in SNR. On the other hand, Fig. 7.3 shows the normalized output data – Velocity vs Range – using subpulse information. Fig. 7.4 shows the normalized output data – Velocity vs Range – using SP. Observe that the loss in SNR is partially mitigated by means of SP. Therefore, the target located at 10 [Km] can now be easily be detect without further processing. At last, Fig. 7.4 shows the combined pulse and subpulse information. Note in Fig. 7.4 that SP provides a better intuition about the target location, but due to its poor discretization, it is not sufficient to determine the exact velocity. Conversely, PP provides a better discretization but, unfortunately, its velocity estimation is more likely to be ambiguous. Thus, by combining SP and the CCRT, we provide the system a high capability to unfold the target's true velocity.

Fig. 7.5 shows PD_i versus SNR_1 using different values of M_i. Note how radar performance improves as M_i increases, requiring a lower SNR for a given PD. This is

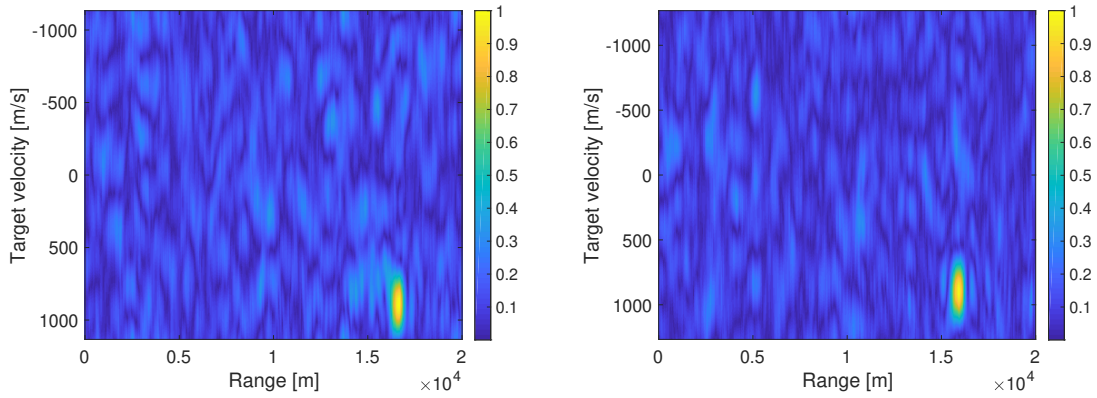

(b–1) $\mathrm{PRF}_1 = 1700$ [Hz], $N_1 = 8$

(b–2) $\mathrm{PRF}_2 = 1900$ [Hz], $N_2 = 8$

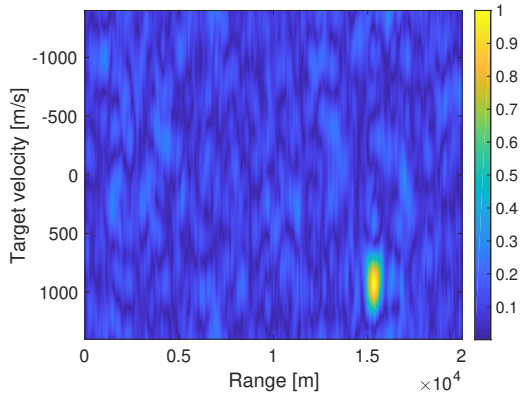

(b–3) $\mathrm{PRF}_3 = 2100$ [Hz], $N_3 = 8$

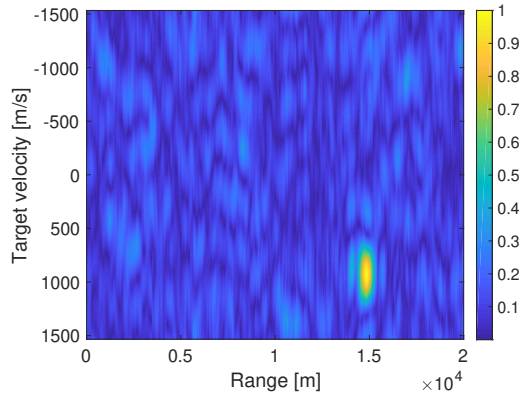

(b–4) $\mathrm{PRF}_4 = 2300$ [Hz], $N_4 = 8$

Figure 7.3 – Velocity versus range: normalized output data using subpulse information.

because when increasing M_i, we are, in fact, increasing the compressed response of PP by means of coherent integration. In particular, for a fixed $\mathrm{SNR}_1 = 10$ [dB], we obtain the following probabilities of detection: $\mathrm{PD}_1 = 0.66$ for $M_1 = 7$; $\mathrm{PD}_2 = 0.78$ for $M_2 = 11$; $\mathrm{PD}_3 = 0.85$ for $M_3 = 13$; and $\mathrm{PD}_4 = 0.93$ for $M_4 = 17$. Also, observe that for the high and medium SNR regime, our derived expression matches perfectly the PD of [14, Eq. (28)]. Nevertheless, there is a small difference in the PD for the low-SNR regime. This occurs because if the compressed response of PP is less than the background noise, then the intersection probability in (7.30) will be less than the probability of $\bigcap_{k=1}^{M_i-1} \mathcal{A}_{k,i}$. For example, given $\mathrm{SNR}_1 = 4$ [dB] and $M_1 = 7$, we obtain $\mathrm{PD}_1 = 0.15$ with our proposed SP–plus–CCRT technique, and $\mathrm{PD}_1 = 0.18$ with [14, Eq. (28)]. However, this small reduction in the PD is compensated by a greater reduction in the PFA, as shall be seen next.

Fig. 7.6 shows PFA_i versus SNR_1 using different values for M_i. Observe how PFA_i decreases as M_i increases. This occurs because as we increase M_i, the received target echo becomes stronger compared to the noise background. For example, for a fixed $\mathrm{SNR}_1 = 5$ [dB], we obtain the following probabilities of false alarm: $\mathrm{PFA}_1 = 0.83$ for $M_1 = 7$; $\mathrm{PFA}_2 = 0.77$ for $M_2 = 11$; $\mathrm{PFA}_3 = 0.73$ for $M_3 = 13$; and $\mathrm{PFA}_4 = 0.60$ for

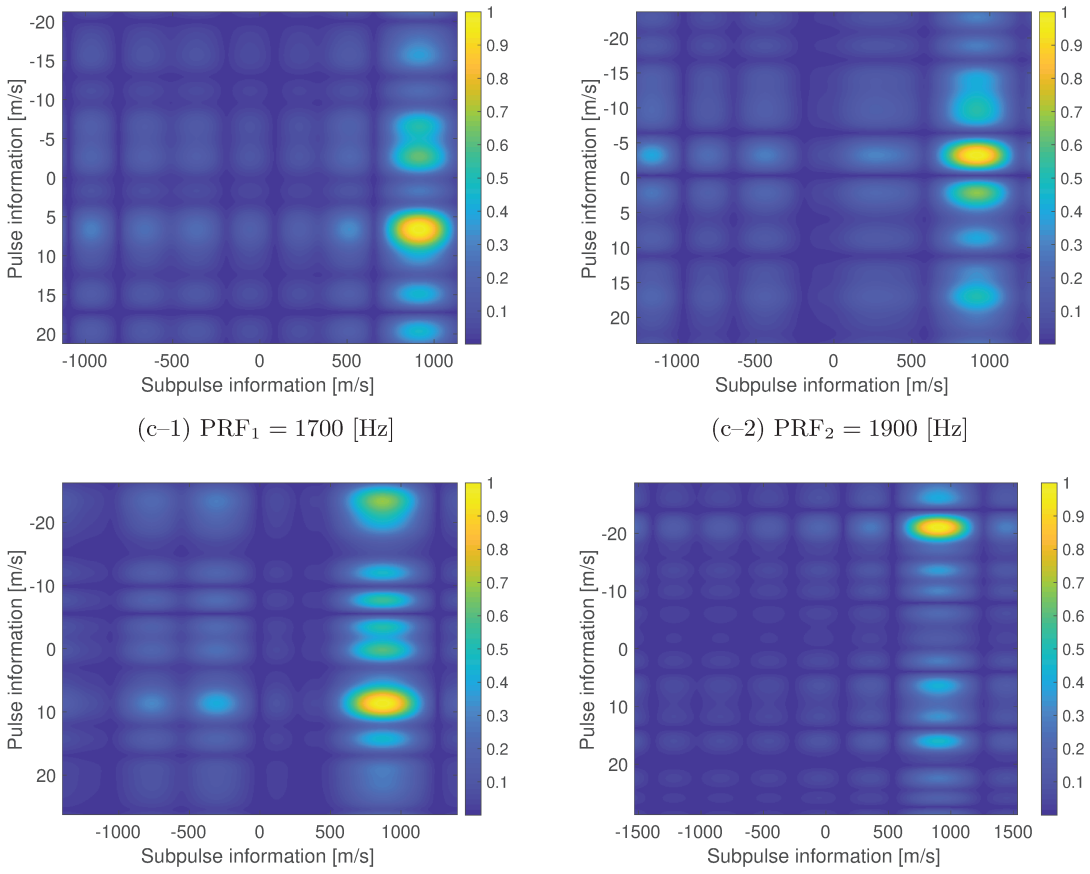

(c–1) $\mathrm{PRF}_1 = 1700$ [Hz]

(c–2) $\mathrm{PRF}_2 = 1900$ [Hz]

(c–3) $\mathrm{PRF}_3 = 2100$ [Hz]

(c–4) $\mathrm{PRF}_4 = 2300$ [Hz]

Figure 7.4 – Combined subpulse and pulse information.

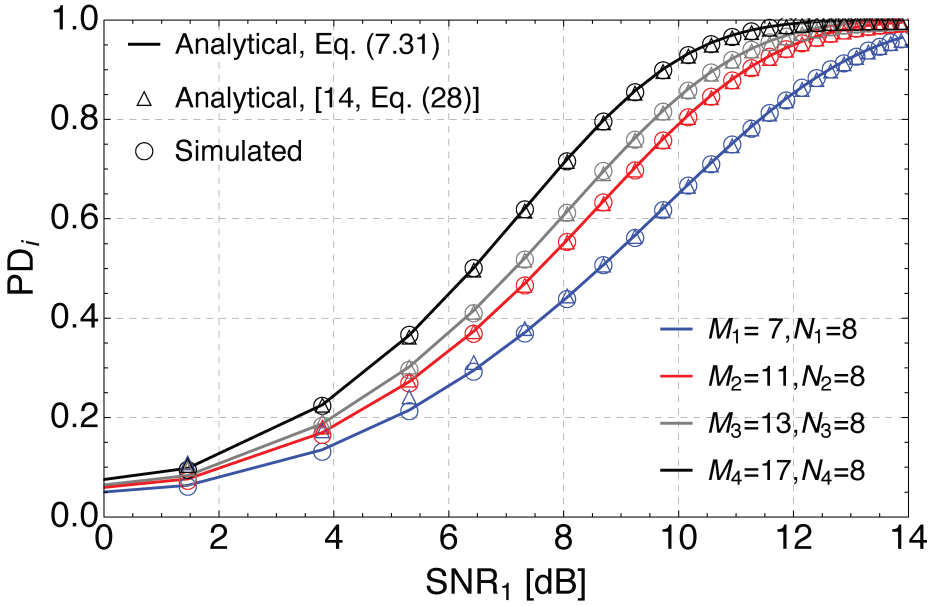

Figure 7.5 – PD_i vs SNR_1 using $N_i = 8$, $\lambda_{1,i} = 0.5$, $\lambda_{2,i} = 0.99$, and different values of M_i ($i \in \{1, 2, 3, 4\}$).

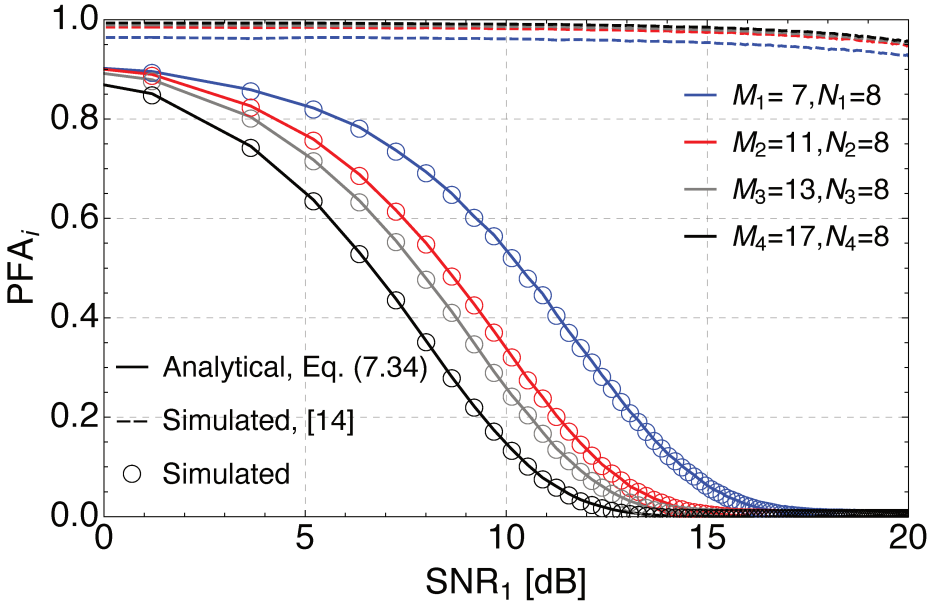

Figure 7.6 – PMD$_i$ vs SNR$_1$ using $N_i = 8$, $\lambda_{1,i} = 0.5$, $\lambda_{2,i} = 0.99$, and different values of M_i ($i \in \{1, 2, 3, 4\}$).

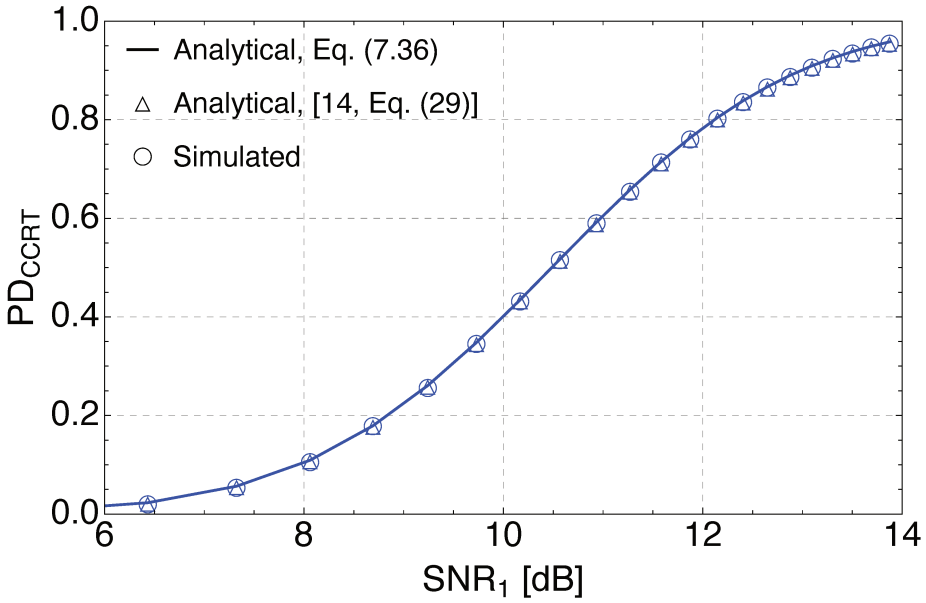

Figure 7.7 – PD$_{\text{CCRT}}$ vs SNR$_1$ using $N_i = 8$, $\lambda_{1,i} = 0.5$, $\lambda_{2,i} = 0.99$, $\mathcal{M} = 4$, and different values of M_i ($i \in \{1, 2, 3, 4\}$).

$M_4 = 17$. More interesting, observe how PFA$_i$ decays rapidly compared to [14]. This difference in PFA$_i$ is because intuitively SP acts as a backup detection process. That is, since the compressed response of SP is greater of the PP response (for high-velocity targets), then the probability in (7.33) is lower than the probability of $\bigcup_{k=1}^{M_i-1} \mathcal{C}_{k,i}$. For example, using the classic PP technique [14], we obtain the following probabilities of false alarm: PFA$_1$ = 0.96 for $M_1 = 7$; PFA$_2$ = 0.97 for $M_2 = 11$; PFA$_3$ = 0.98 for $M_3 = 13$; and PFA$_4$ = 0.99 for $M_3 = 17$.

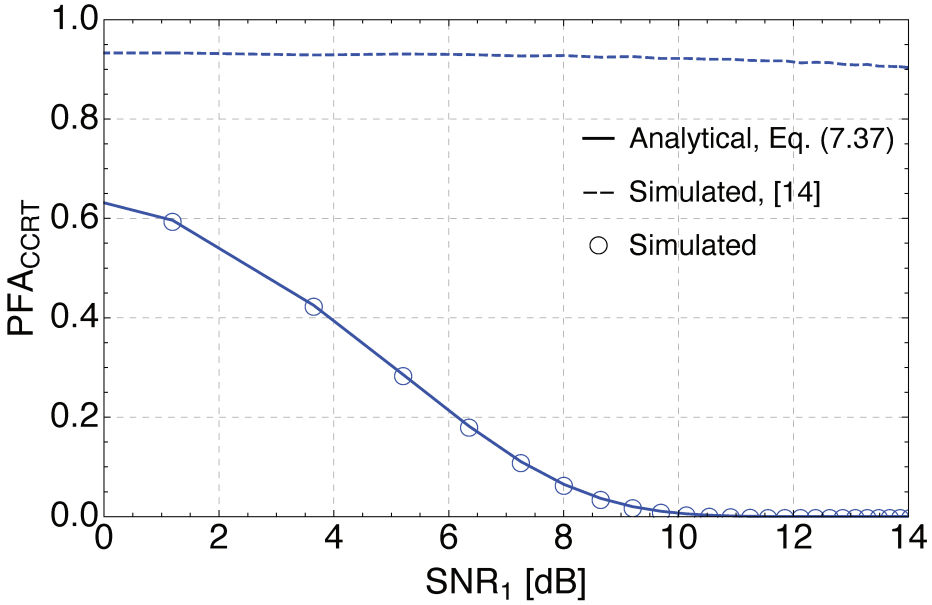

Figure 7.8 – $\mathrm{PMD}_{\mathrm{CCRT}}$ vs SNR_1 using $N_i = 8$, $\lambda_{1,i} = 0.5$, $\lambda_{2,i} = 0.99$, $\mathcal{M} = 4$, and different values of M_i ($i \in \{1, 2, 3, 4\}$).

Finally, Figs. 7.7 and 7.8 show $\mathrm{PD}_{\mathrm{CCRT}}$ and $\mathrm{PFA}_{\mathrm{CCRT}}$ versus SNR_1, respectively. Observe in Fig. 7.7, the perfect agreement between (7.36) and [14, Eq. (29)]. Hence, in this case, we have no advantage when using SP–plus–CCRT. On the other hand, observe in Fig. 7.8, the high difference in the PFA between of (7.37) and that in [14]. In this case, the use of SP–plus–CCRT improves radar performance by considerably reducing the false alarms. For instance, for given $\mathrm{SNR}_1 = 2$ [dB], we obtain probabilities of $\mathrm{PFA}_{\mathrm{CCRT}} = 0.94$ using PP–plus–CCRT, and $\mathrm{PFA}_{\mathrm{CCRT}} = 0.54$ using SP–plus–CCRT.

7.6 Conclusion

In this work, we provided a thorough statistical analysis on Doppler estimation when both SP and the CCRT were employed. To do so, we derived novel and closed-form expressions for the PD and PFA. Moreover, a comparison analysis between our proposed SP–plus–CCRT technique and the classic PP–plus–CCRT was carried out. Numerical results and Monte-Carlo simulations corroborated the validity of our expressions and showed that the PFA when using SP–plus–CCRT technique was greatly reduced compared to [14], thereby enhancing radar detection.

7.7 Bibliography

[1] G. Morris and L. Harkness, *Airborne Pulsed Doppler Radar*, 2nd ed. Norwood, MA, USA: Artech House, 1996.

[2] M. A. Richards, J. Scheer, W. A. Holm, and W. L. Melvin, *Principles of Modern Radar: Basic Principles*, 1st ed. West Perth, WA, Australia: SciTech, 2010.

[3] G. V. Trunk, "Range resolution of targets using automatic detectors," *IEEE Trans. Aerosp. Electron. Syst.*, vol. AES-14, no. 5, pp. 750–755, Sept. 1978.

[4] S. A. Hovanessian, "An algorithm for calculation of range in a multiple PRF radar," *IEEE Trans. Aerosp. Electron. Syst.*, vol. AES-12, no. 2, pp. 287–290, Mar. 1976.

[5] X.-G. Xia and G. Wang, "Phase unwrapping and a robust chinese remainder theorem," *IEEE Signal Process. Lett.*, vol. 14, no. 4, pp. 247–250, Apr. 2007.

[6] X. Li, H. Liang, and X. Xia, "A robust chinese remainder theorem with its applications in frequency estimation from undersampled waveforms," *IEEE Trans. Signal Process.*, vol. 57, no. 11, pp. 4314–4322, Nov. 2009.

[7] W. Wang and X. Xia, "A closed-form robust chinese remainder theorem and its performance analysis," *IEEE Trans. Signal Process.*, vol. 58, no. 11, pp. 5655–5666, Nov. 2010.

[8] G. V. Trunk and W. M. Kim, "Ambiguity resolution of multiple targets using pulse-Doppler waveforms," *IEEE Trans. Aerosp. Electron. Syst.*, vol. 30, no. 4, pp. 1130–1137, Oct. 1994.

[9] F. D. A. García, A. S. Guerreiro, G. R. L. Tejerina, J. C. S. Santos Filho, G. Fraidenraich, M. D. Yacoub, M. A. M. Miranda, and H. Cioqueta, "Probability of detection for unambiguous doppler frequencies in pulsed radars using the chinese remainder theorem and subpulse processing," in *Proc. 53rd Asilomar Conference on Signals, Systems, and Computers*, Pacific Grove, CA, USA, Nov. 2019, pp. 138–142.

[10] M. I. Skolnik, *Introduction to Radar Systems*, 3rd ed. Ney York, NY, USA: McGraw-Hill, 2001.

[11] G. Beltrao, L. Pralon, M. Menezes, P. Vyplavin, B. Pompeo, and M. Pralon, "Subpulse processing for long range surveillance noise radars," in *Proc. International Conference on Radar Systems (Radar 2017)*, Belfast, UK, Oct. 2017, pp. 1–4.

[12] A. Barreto, L. Pralon, B. Pompeo, G. Beltrao, and M. Pralon, "FPGA design and implementation of a real-time subpulse processing architecture for noise radars," in *Proc. 2019 International Radar Conference (RADAR)*, Toulon, France, Sept. 2019, pp. 1–6.

[13] D. S. Doviak and R. J. Zrnic, *Doppler Radar and Weather Observations*, 2nd ed. San Diego, CA, USA: Academic Press, 2001.

[14] B. Silva and G. Fraidenraich, "Performance analysis of the classic and robust chinese remainder theorems in pulsed doppler radars," *IEEE Trans. Signal Process.*, vol. 66, no. 18, pp. 4898–4903, Sept. 2018.

[15] M. A. Richards, *Fundamentals of Radar Signal Processing*, 2nd ed. Ney York, NY, USA: McGraw-Hill, 2014.

[16] D. K. Barton, *Radar Equations for Modern Radar*, 1st ed. Massachusetts, MA, USA: Artech House, 2013.

[17] G. Trunk and S. Brockett, "Range and velocity ambiguity resolution," in *Proc. Record IEEE Nat. Radar Conf.*, Lynnfield, MA, USA, Apr. 1993, pp. 146–149.

[18] A. Ferrari, C. Berenguer, and G. Alengrin, "Doppler ambiguity resolution using multiple PRF," *IEEE Trans. Aerosp. Electron. Syst.*, vol. 33, no. 3, pp. 738–751, Jul. 1997.

[19] A. Papoulis, *Probability, Random Variables, and Stochastic Processes*, 4th ed. Ney York, NY, USA: McGraw-Hill, 2002.

[20] N. C. Beaulieu and K. T. Hemachandra, "Novel representations for the bivariate rician distribution," *IEEE Trans. Commun.*, vol. 59, no. 11, pp. 2951–2954, Nov. 2011.

[21] A. Behnad, N. C. Beaulieu, and K. T. Hemachandra, "Correction to "Novel representations for the bivariate rician distribution"," *IEEE Trans. Commun.*, vol. 60, no. 6, pp. 1486–1486, Jun. 2012.

[22] M. Abramowitz and I. A. Stegun, *Handbook of Mathematical Functions with Formulas, Graphs, and Mathematical Tables*, 10th ed. Washington, DC: US Dept. of Commerce: National Bureau of Standards, 1972.

[23] Y. H. Wang, "On the number of successes in independent trials," *Statistica Sinica*, vol. 3, no. 2, pp. 295–312, 1993.

8 Conclusions and Future Directions

This chapter highlights the main contributions of this dissertation and suggests possible directions for future related works.

8.1 Concluding Remarks

In this dissertation, we tackled three main aspects in the field of radar systems: (i) detection of distributed and point-like targets embedded in CWGN; (ii) radar performance in the presence of Weibull-distributed ground clutter; and (iii) Doppler estimation for high-velocity targets in background Gaussian noise.

In the first part of this dissertation (Chapters 2–4), we focused on the design and evaluation of optimal and suboptimal detectors for both distributed and point-like targets. For the case of distributed targets, we designed and analyzed an optimal detector by making use of the LRT framework (i.e., assuming known distribution parameters). Here, the decision on whether a distributed target is present or absent capitalized on the degree of correlation between the signal samples collected by a linear phased-array radar. For comparison purposes, a suboptimal detector using a regular phased-array approach was also derived and analyzed. For the case of point-like targets, we assessed the standard detection problem of weak signals in background noise and provided two important contributions. First, we derived alternative representations for the PD of a phased array radar operating with non-fluctuating targets embedded in CWGN. Second, we designed and analyzed a new GLRT detector (i.e., under unknown distribution parameters). The detection was carried out after a beamforming operation. This particular feature allows this detector to enjoy lower demands on hardware, processing, and data storage than traditional GLRT detectors. The PFA and PD were also obtained in closed form. A series representation for the PD was also derived. It was shown that, in the low-SNR regime, the proposed post-beamforming GLRT detector outperforms both the classic pre-beamforming GLRT detector and the brute-force square-law detector. It was also shown that the PFA of the post-beamforming GLRT detector is independent of the number of antennas, which allows for tuning the PD while maintaining a fixed PFA.

In the second part of this dissertation (Chapters 5 and 6), we investigated the radar performance over Weibull-distributed ground clutter. With this aim, we provided highly accurate approximations and exact solutions for the PD and PFA of a square-law detector operating in homogeneous Weibull clutter environments. In passing, we obtained

the exact and approximate PDF and CDF of the sum statistics that govern the output of a square-law detector. Besides, a complete CA-CFAR analysis was carried out by considering that the clutter residues and target returns lie within the CUT. All metrics were obtained in terms of both closed-form solutions and series representations. The closed-form solutions capitalized on the Fox H-function, whereas the series representations were obtained by performing a thorough calculus of residues.

Finally, in the third part of this dissertation (Chapter 7), we provided a complete statistical analysis for the Doppler estimation of high-velocity targets. To do so, we made use of the combined technique CCRT–plus–SP. This technique intends to mitigate the SNR loss caused by the mismatch between the received signal and its replica, as well as to resolve Doppler ambiguities that appear whenever the target's Doppler shift is greater than the PRF. The PD and PFA were derived in closed form when the CCRT–plus–SP scheme is applied. It was shown that the performance of the CCRT–plus–SP scheme is superior to that of the classic PP scheme, rendering a remarkable reduction in the PFA.

Exhaustive numerical results and Monte-Carlo simulations were used to validated the analytical contributions in this dissertation.

8.2 Future Directions

Some possible directions for future related works are summarized next.

1. An immediate direction to be followed would be to carry out a comprehensive analysis for distributed target (e.g., clouds and precipitation) detection using our post-beamforming GRLT-based approach.

2. Another direction would be to complete the post-beamforming GRLT-based detection analysis carried out in Chapter 4 for some fluctuating target models, e.g., Swerling I and II.

3. A third direction would be to extend the CA-CFAR analysis carried out in Chapter 5 to other types of CFAR detectors, such as GOCA-CFAR and SOCA-CFAR. As done in that chapter, one may consider the presence of clutter residues and target returns within the CUT.

4. A last direction would be to perform a thorough statistical analysis as in Chapter 7, but using instead the so-called Robust Chinese Remainder Theorem (RCRT), which has a better response to small measurement errors.

8.3 Bibliography

[1] G. Morris and L. Harkness, *Airborne Pulsed Doppler Radar*, 2nd ed. Norwood, MA, USA: Artech House, 1996.

[2] M. A. Richards, J. Scheer, W. A. Holm, and W. L. Melvin, *Principles of Modern Radar: Basic Principles*, 1st ed. West Perth, WA, Australia: SciTech, 2010.

[3] G. V. Trunk, "Range resolution of targets using automatic detectors," *IEEE Trans. Aerosp. Electron. Syst.*, vol. AES-14, no. 5, pp. 750–755, Sept. 1978.

[4] S. A. Hovanessian, "An algorithm for calculation of range in a multiple PRF radar," *IEEE Trans. Aerosp. Electron. Syst.*, vol. AES-12, no. 2, pp. 287–290, Mar. 1976.

[5] X.-G. Xia and G. Wang, "Phase unwrapping and a robust chinese remainder theorem," *IEEE Signal Process. Lett.*, vol. 14, no. 4, pp. 247–250, Apr. 2007.

[6] X. Li, H. Liang, and X. Xia, "A robust chinese remainder theorem with its applications in frequency estimation from undersampled waveforms," *IEEE Trans. Signal Process.*, vol. 57, no. 11, pp. 4314–4322, Nov. 2009.

[7] W. Wang and X. Xia, "A closed-form robust chinese remainder theorem and its performance analysis," *IEEE Trans. Signal Process.*, vol. 58, no. 11, pp. 5655–5666, Nov. 2010.

[8] G. V. Trunk and W. M. Kim, "Ambiguity resolution of multiple targets using pulse-Doppler waveforms," *IEEE Trans. Aerosp. Electron. Syst.*, vol. 30, no. 4, pp. 1130–1137, Oct. 1994.

[9] F. D. A. García, A. S. Guerreiro, G. R. L. Tejerina, J. C. S. Santos Filho, G. Fraidenraich, M. D. Yacoub, M. A. M. Miranda, and H. Cioqueta, "Probability of detection for unambiguous doppler frequencies in pulsed radars using the chinese remainder theorem and subpulse processing," in *Proc. 53rd Asilomar Conference on Signals, Systems, and Computers*, Pacific Grove, CA, USA, Nov. 2019, pp. 138–142.

[10] M. I. Skolnik, *Introduction to Radar Systems*, 3rd ed. Ney York, NY, USA: McGraw-Hill, 2001.

[11] G. Beltrao, L. Pralon, M. Menezes, P. Vyplavin, B. Pompeo, and M. Pralon, "Subpulse processing for long range surveillance noise radars," in *Proc. International Conference on Radar Systems (Radar 2017)*, Belfast, UK, Oct. 2017, pp. 1–4.

[12] A. Barreto, L. Pralon, B. Pompeo, G. Beltrao, and M. Pralon, "FPGA design and implementation of a real-time subpulse processing architecture for noise radars," in

Proc. 2019 International Radar Conference (RADAR), Toulon, France, Sept. 2019, pp. 1–6.

[13] D. S. Doviak and R. J. Zrnic, *Doppler Radar and Weather Observations*, 2nd ed. San Diego, CA, USA: Academic Press, 2001.

[14] B. Silva and G. Fraidenraich, "Performance analysis of the classic and robust chinese remainder theorems in pulsed doppler radars," *IEEE Trans. Signal Process.*, vol. 66, no. 18, pp. 4898–4903, Sept. 2018.

[15] M. A. Richards, *Fundamentals of Radar Signal Processing*, 2nd ed. Ney York, NY, USA: McGraw-Hill, 2014.

[16] D. K. Barton, *Radar Equations for Modern Radar*, 1st ed. Massachusetts, MA, USA: Artech House, 2013.

[17] G. Trunk and S. Brockett, "Range and velocity ambiguity resolution," in *Proc. Record IEEE Nat. Radar Conf.*, Lynnfield, MA, USA, Apr. 1993, pp. 146–149.

[18] A. Ferrari, C. Berenguer, and G. Alengrin, "Doppler ambiguity resolution using multiple PRF," *IEEE Trans. Aerosp. Electron. Syst.*, vol. 33, no. 3, pp. 738–751, Jul. 1997.

[19] A. Papoulis, *Probability, Random Variables, and Stochastic Processes*, 4th ed. Ney York, NY, USA: McGraw-Hill, 2002.

[20] N. C. Beaulieu and K. T. Hemachandra, "Novel representations for the bivariate rician distribution," *IEEE Trans. Commun.*, vol. 59, no. 11, pp. 2951–2954, Nov. 2011.

[21] A. Behnad, N. C. Beaulieu, and K. T. Hemachandra, "Correction to "Novel representations for the bivariate rician distribution"," *IEEE Trans. Commun.*, vol. 60, no. 6, pp. 1486–1486, Jun. 2012.

[22] M. Abramowitz and I. A. Stegun, *Handbook of Mathematical Functions with Formulas, Graphs, and Mathematical Tables*, 10th ed. Washington, DC: US Dept. of Commerce: National Bureau of Standards, 1972.

[23] Y. H. Wang, "On the number of successes in independent trials," *Statistica Sinica*, vol. 3, no. 2, pp. 295–312, 1993.

Appendices

APPENDIX A – Permission to Reproduce Copyrighted Material

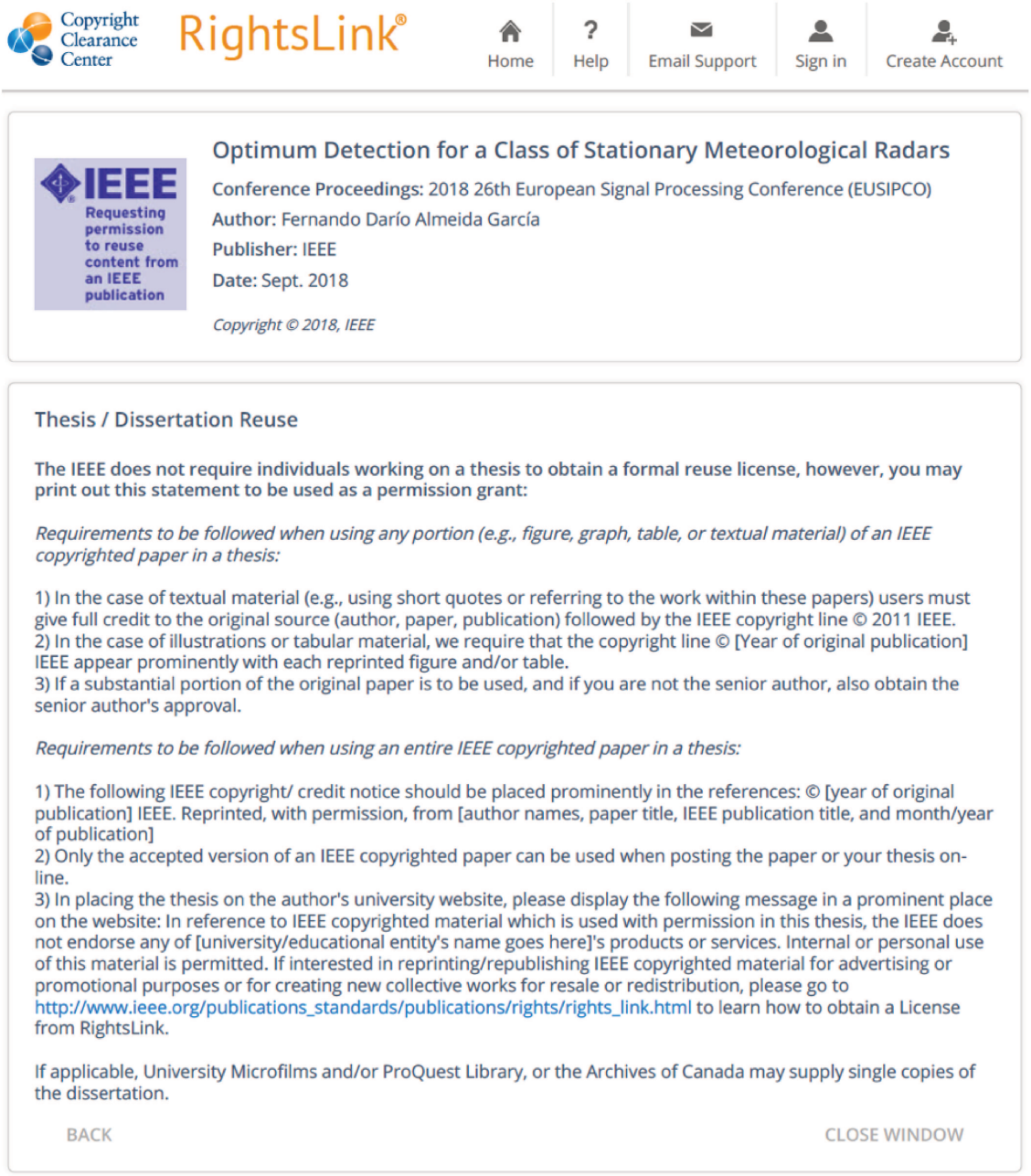

Copyright Clearance Center RightsLink®

Home | Help | Email Support | Sign in | Create Account

IEEE Requesting permission to reuse content from an IEEE publication

Optimum Detection for a Class of Stationary Meteorological Radars

Conference Proceedings: 2018 26th European Signal Processing Conference (EUSIPCO)

Author: Fernando Darío Almeida García

Publisher: IEEE

Date: Sept. 2018

Copyright © 2018, IEEE

Thesis / Dissertation Reuse

The IEEE does not require individuals working on a thesis to obtain a formal reuse license, however, you may print out this statement to be used as a permission grant:

Requirements to be followed when using any portion (e.g., figure, graph, table, or textual material) of an IEEE copyrighted paper in a thesis:

1) In the case of textual material (e.g., using short quotes or referring to the work within these papers) users must give full credit to the original source (author, paper, publication) followed by the IEEE copyright line © 2011 IEEE.
2) In the case of illustrations or tabular material, we require that the copyright line © [Year of original publication] IEEE appear prominently with each reprinted figure and/or table.
3) If a substantial portion of the original paper is to be used, and if you are not the senior author, also obtain the senior author's approval.

Requirements to be followed when using an entire IEEE copyrighted paper in a thesis:

1) The following IEEE copyright/ credit notice should be placed prominently in the references: © [year of original publication] IEEE. Reprinted, with permission, from [author names, paper title, IEEE publication title, and month/year of publication]
2) Only the accepted version of an IEEE copyrighted paper can be used when posting the paper or your thesis on-line.
3) In placing the thesis on the author's university website, please display the following message in a prominent place on the website: In reference to IEEE copyrighted material which is used with permission in this thesis, the IEEE does not endorse any of [university/educational entity's name goes here]'s products or services. Internal or personal use of this material is permitted. If interested in reprinting/republishing IEEE copyrighted material for advertising or promotional purposes or for creating new collective works for resale or redistribution, please go to http://www.ieee.org/publications_standards/publications/rights/rights_link.html to learn how to obtain a License from RightsLink.

If applicable, University Microfilms and/or ProQuest Library, or the Archives of Canada may supply single copies of the dissertation.

BACK CLOSE WINDOW

Alternative representations for the probability of detection of non-fluctuating targets

Author(s): F.D.A. García [1] ; H.R.C. Mora [2] ; N. V.O. Garzón [2] ; J.C.S. Santos Filho [1]

View affiliations

Source: Volume 56, Issue 21, 15 October 2020, p. 1136 – 1139

DOI: 10.1049/el.2020.1810 , Print ISSN 0013-5194, Online ISSN 1350-911X

Received 22/06/2020, Published 07/09/2020

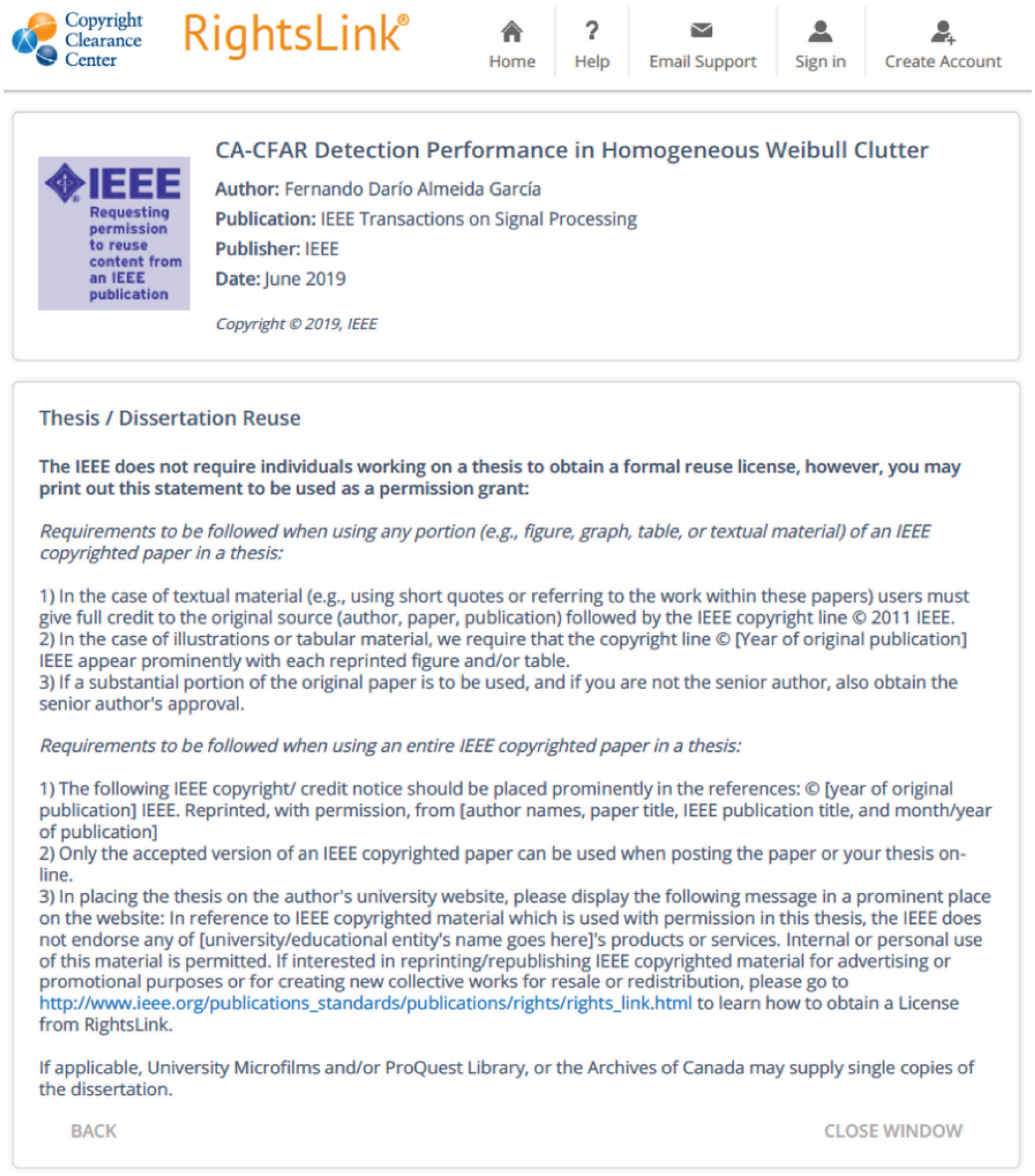

Copyright Clearance Center RightsLink®

Home | Help | Email Support | Sign in | Create Account

IEEE Requesting permission to reuse content from an IEEE publication

CA-CFAR Detection Performance in Homogeneous Weibull Clutter

Author: Fernando Darío Almeida García
Publication: IEEE Transactions on Signal Processing
Publisher: IEEE
Date: June 2019

Copyright © 2019, IEEE

Thesis / Dissertation Reuse

The IEEE does not require individuals working on a thesis to obtain a formal reuse license, however, you may print out this statement to be used as a permission grant:

Requirements to be followed when using any portion (e.g., figure, graph, table, or textual material) of an IEEE copyrighted paper in a thesis:

1) In the case of textual material (e.g., using short quotes or referring to the work within these papers) users must give full credit to the original source (author, paper, publication) followed by the IEEE copyright line © 2011 IEEE.
2) In the case of illustrations or tabular material, we require that the copyright line © [Year of original publication] IEEE appear prominently with each reprinted figure and/or table.
3) If a substantial portion of the original paper is to be used, and if you are not the senior author, also obtain the senior author's approval.

Requirements to be followed when using an entire IEEE copyrighted paper in a thesis:

1) The following IEEE copyright/ credit notice should be placed prominently in the references: © [year of original publication] IEEE. Reprinted, with permission, from [author names, paper title, IEEE publication title, and month/year of publication]
2) Only the accepted version of an IEEE copyrighted paper can be used when posting the paper or your thesis on-line.
3) In placing the thesis on the author's university website, please display the following message in a prominent place on the website: In reference to IEEE copyrighted material which is used with permission in this thesis, the IEEE does not endorse any of [university/educational entity's name goes here]'s products or services. Internal or personal use of this material is permitted. If interested in reprinting/republishing IEEE copyrighted material for advertising or promotional purposes or for creating new collective works for resale or redistribution, please go to http://www.ieee.org/publications_standards/publications/rights/rights_link.html to learn how to obtain a License from RightsLink.

If applicable, University Microfilms and/or ProQuest Library, or the Archives of Canada may supply single copies of the dissertation.

BACK CLOSE WINDOW

Copyright Clearance Center RightsLink®

Home | Help | Email Support | Sign in | Create Account

IEEE Requesting permission to reuse content from an IEEE publication

Square-Law Detection of Exponential Targets in Weibull-Distributed Ground Clutter

Author: Fernando Darío Almeida García

Publication: IEEE Transactions on Signal Processing

Publisher: IEEE

Date: Dec 31, 1969

Copyright © 1969, IEEE

Thesis / Dissertation Reuse

The IEEE does not require individuals working on a thesis to obtain a formal reuse license, however, you may print out this statement to be used as a permission grant:

Requirements to be followed when using any portion (e.g., figure, graph, table, or textual material) of an IEEE copyrighted paper in a thesis:

1) In the case of textual material (e.g., using short quotes or referring to the work within these papers) users must give full credit to the original source (author, paper, publication) followed by the IEEE copyright line © 2011 IEEE.
2) In the case of illustrations or tabular material, we require that the copyright line © [Year of original publication] IEEE appear prominently with each reprinted figure and/or table.
3) If a substantial portion of the original paper is to be used, and if you are not the senior author, also obtain the senior author's approval.

Requirements to be followed when using an entire IEEE copyrighted paper in a thesis:

1) The following IEEE copyright/ credit notice should be placed prominently in the references: © [year of original publication] IEEE. Reprinted, with permission, from [author names, paper title, IEEE publication title, and month/year of publication]
2) Only the accepted version of an IEEE copyrighted paper can be used when posting the paper or your thesis on-line.
3) In placing the thesis on the author's university website, please display the following message in a prominent place on the website: In reference to IEEE copyrighted material which is used with permission in this thesis, the IEEE does not endorse any of [university/educational entity's name goes here]'s products or services. Internal or personal use of this material is permitted. If interested in reprinting/republishing IEEE copyrighted material for advertising or promotional purposes or for creating new collective works for resale or redistribution, please go to http://www.ieee.org/publications_standards/publications/rights/rights_link.html to learn how to obtain a License from RightsLink.

If applicable, University Microfilms and/or ProQuest Library, or the Archives of Canada may supply single copies of the dissertation.

BACK CLOSE WINDOW

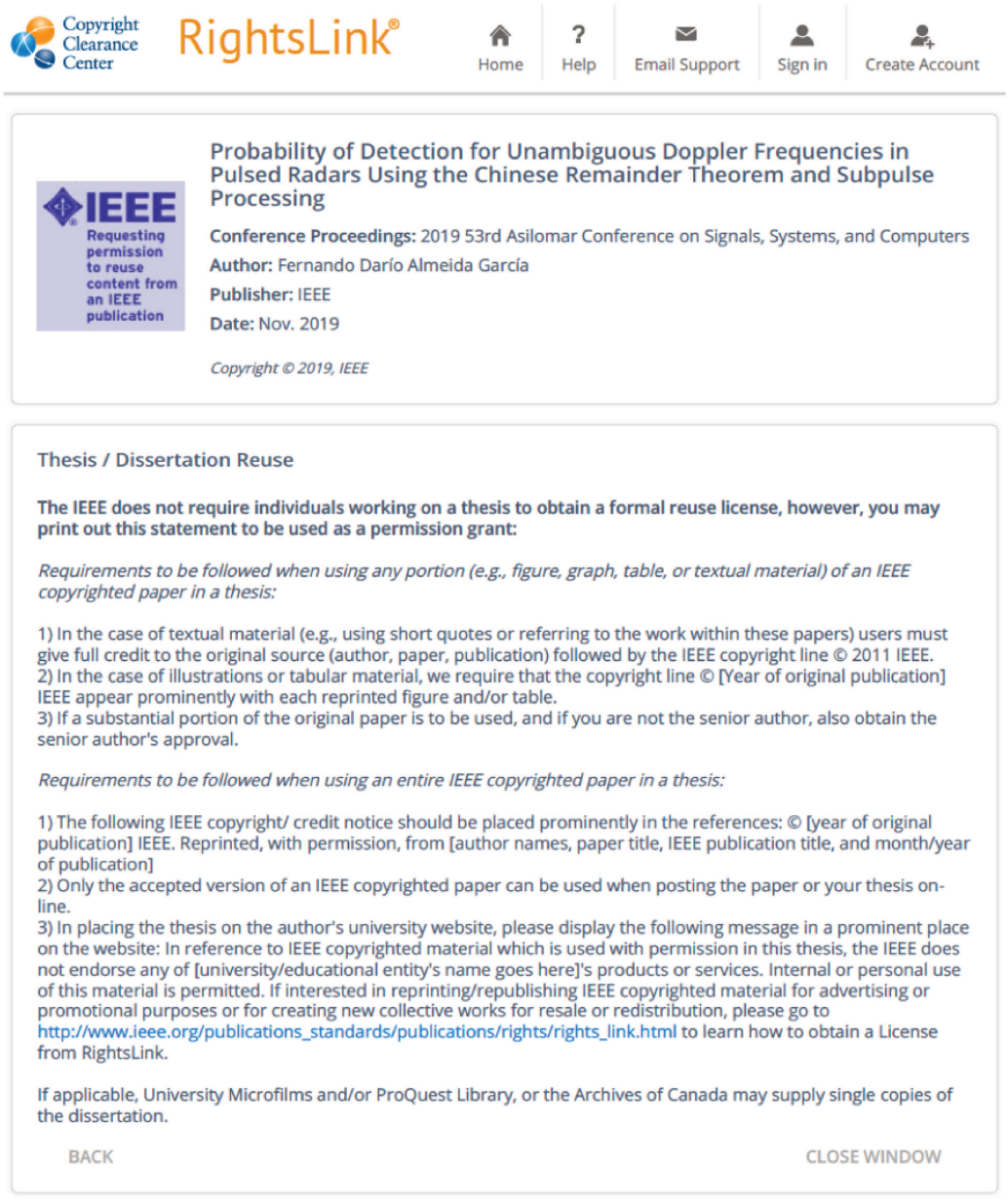

Copyright Clearance Center RightsLink®

Home | Help | Email Support | Sign in | Create Account

IEEE Requesting permission to reuse content from an IEEE publication

Probability of Detection for Unambiguous Doppler Frequencies in Pulsed Radars Using the Chinese Remainder Theorem and Subpulse Processing

Conference Proceedings: 2019 53rd Asilomar Conference on Signals, Systems, and Computers

Author: Fernando Darío Almeida García

Publisher: IEEE

Date: Nov. 2019

Copyright © 2019, IEEE

Thesis / Dissertation Reuse

The IEEE does not require individuals working on a thesis to obtain a formal reuse license, however, you may print out this statement to be used as a permission grant:

Requirements to be followed when using any portion (e.g., figure, graph, table, or textual material) of an IEEE copyrighted paper in a thesis:

1) In the case of textual material (e.g., using short quotes or referring to the work within these papers) users must give full credit to the original source (author, paper, publication) followed by the IEEE copyright line © 2011 IEEE.
2) In the case of illustrations or tabular material, we require that the copyright line © [Year of original publication] IEEE appear prominently with each reprinted figure and/or table.
3) If a substantial portion of the original paper is to be used, and if you are not the senior author, also obtain the senior author's approval.

Requirements to be followed when using an entire IEEE copyrighted paper in a thesis:

1) The following IEEE copyright/ credit notice should be placed prominently in the references: © [year of original publication] IEEE. Reprinted, with permission, from [author names, paper title, IEEE publication title, and month/year of publication]
2) Only the accepted version of an IEEE copyrighted paper can be used when posting the paper or your thesis on-line.
3) In placing the thesis on the author's university website, please display the following message in a prominent place on the website: In reference to IEEE copyrighted material which is used with permission in this thesis, the IEEE does not endorse any of [university/educational entity's name goes here]'s products or services. Internal or personal use of this material is permitted. If interested in reprinting/republishing IEEE copyrighted material for advertising or promotional purposes or for creating new collective works for resale or redistribution, please go to http://www.ieee.org/publications_standards/publications/rights/rights_link.html to learn how to obtain a License from RightsLink.

If applicable, University Microfilms and/or ProQuest Library, or the Archives of Canada may supply single copies of the dissertation.

BACK CLOSE WINDOW

APPENDIX B – Supporting Material for Chapter 4

B.1 Proof of Lemma 1

Let us define the following RV

$$\mathcal{I}_3 \triangleq \frac{1}{N\sigma^2}\sum_{k=1}^{M}\left(\mathbf{Re}\left[r_k\right]-\mu_X\right)^2, \tag{B.1}$$

where μ_X is the total sum of the target echoes for the in-phase components.

Rewriting (D.4), we have

$$\mathcal{I}_3 = \sum_{k=1}^{M}\left(\frac{\mathbf{Re}\left[r_k\right]-\mu_X}{\sqrt{N}\sigma}\right)^2. \tag{B.2}$$

It can be noticed that $\mathcal{I}_3$ is a sum of the squares of M standard Gaussian (zero mean and unit variance) RVs. Therefore, $\mathcal{I}_3$ can be modeled by a CCS RV with M degrees of freedom.

Now, after performing some manipulations, we can rewrite (B.2) as

$$\begin{aligned}
\mathcal{I}_3 =& \sum_{k=1}^{M}\left(\frac{\mathbf{Re}\left[r_k\right]-\hat{\mu}_X}{\sqrt{N}\sigma}+\frac{\hat{\mu}_X-\mu_X}{\sqrt{N}\sigma}\right)^2 \\
\overset{(a)}{=}& \sum_{k=1}^{M}\left(\frac{\mathbf{Re}\left[r_k\right]-\hat{\mu}_X}{\sqrt{N}\sigma}\right)^2 + 2\left(\frac{\hat{\mu}_X-\mu_X}{\sqrt{N}\sigma}\right) \\
& \times\left(\frac{\sum_{k=1}^{M}\mathbf{Re}\left[r_k\right]-M\hat{\mu}_X}{\sqrt{N}\sigma}\right)+\sum_{k=1}^{M}\left(\frac{\hat{\mu}_X-\mu_X}{\sqrt{N}\sigma}\right)^2 \\
\overset{(b)}{=}& \underbrace{\sum_{k=1}^{M}\left(\frac{\mathbf{Re}\left[r_k\right]-\hat{\mu}_X}{\sqrt{N}\sigma}\right)^2}_{\triangleq\ \mathcal{I}_4} + \underbrace{\left(\frac{\hat{\mu}_X-\mu_X}{\sqrt{N}\sigma/M}\right)^2}_{\triangleq\ \mathcal{I}_5},
\end{aligned} \tag{B.3}$$

where in step (b) we use the fact that $M\hat{\mu}_X = \sum_{k=1}^{M}\mathbf{Re}\left[r_k\right]$ and, consequently, the second term in step (a) vanishes. Observe that $\mathcal{I}_5$ represents the square of a standard Gaussian variable and, therefore, can be modeled by a CCS distribution with one degree of freedom.

Employing the additivity property of the CCS distribution [2] and taking into account the distributions of $\mathcal{I}_3$ and $\mathcal{I}_5$, we can now describe $\mathcal{I}_4$ by a CCS RV with $M-1$ degrees of freedom. Also, observe that $\mathcal{I}_4$ is just the first term of (4.22).

Following the same approach, it can be prove that the second term in (4.22) also follows a CCS distribution with $M-1$ degrees of freedom. Since $\mathcal{I}_2$ is formed by

the sum of two CCS RVs, then its distribution is governed by a CCS RV with $2(M-1)$ degrees of freedom, which completes the proof. It is worth mentioning that this result remains true regardless of the hypothesis, because any value of μ_X or μ_Y will not affect the distribution of $\mathcal{I}_2$.

B.2 Proof of Lemma 2

Let

$$P_1 = \mathbf{L}\left(\mathbf{L}^T\mathbf{L}\right)^{-1}\mathbf{L}^T = \frac{1}{M}\mathbf{L}\,\mathbf{L}^T \tag{B.4}$$

$$P_2 = \mathbf{I} - P_1 = \mathbf{I} - \frac{1}{M}\mathbf{L}\,\mathbf{L}^T \tag{B.5}$$

be symmetric and idempotent matrices such that $\text{rank}\,(P_1) = \mathbf{L}$, $\text{rank}\,(P_2) = M-1$ and $P_1 + P_2 = \mathbf{I}$, where $\mathbf{I} \in \mathbb{N}^{M\times M}$ represents the identity matrix and $\mathbf{L} = [1, 1, \cdots, 1]^T \in \mathbb{N}^M$ is the unitary vector. In addition, let

$$\mathbf{Re}\,[\underline{r}] = [\mathbf{Re}\,[r_1], \mathbf{Re}\,[r_2], \cdots, \mathbf{Re}\,[r_M]]^T \tag{B.6}$$

be a random vector with $\mathbb{E}\,[\mathbf{Re}\,[\underline{r}]] = \mu_X\mathbf{L}$ and $\mathbb{COV}\,[\mathbf{Re}\,[\underline{r}]] = N\sigma^2\mathbf{I}$. Then, the Cochran's Theorem [3] states that

$$\omega_1 = \frac{\mathbf{Re}\,[\underline{r}]^T P_1\,\mathbf{Re}\,[\underline{r}]}{N\sigma^2} \tag{B.7}$$

$$\omega_2 = \frac{\mathbf{Re}\,[\underline{r}]^T P_2\,\mathbf{Re}\,[\underline{r}]}{N\sigma^2} \tag{B.8}$$

are independently distributed.

Now, replacing (B.4) in (B.7), we have

$$\begin{aligned}\omega_1 &= \frac{1}{N\sigma^2}\mathbf{Re}\,[\underline{r}]^T\left(\frac{1}{M}\mathbf{L}\,\mathbf{L}^T\right)\mathbf{Re}\,[\underline{r}]\\ &= \frac{1}{MN\sigma^2}\mathbf{Re}\,[\underline{r}]^T\,\mathbf{L}\,\mathbf{L}^T\mathbf{Re}\,[\underline{r}]\\ &= \frac{1}{MN\sigma^2}\left(\sum_{k=1}^{M}\mathbf{Re}\,[r_k]\right)^2.\end{aligned} \tag{B.9}$$

Similarly, inserting (B.5) in (B.8), we have

$$\begin{aligned}\omega_2 &\overset{(a)}{=} \frac{1}{N\sigma^2}\mathbf{Re}\,[\underline{r}]^T P_2^T P_2\mathbf{Re}\,[\underline{r}]\\ &= \frac{1}{N\sigma^2}\left\|P_2\mathbf{Re}\,[\underline{r}]\right\|^2\\ &\overset{(b)}{=} \frac{1}{N\sigma^2}\left\|\left(\mathbf{I} - \frac{1}{M}\mathbf{L}\,\mathbf{L}^T\right)\mathbf{Re}\,[\underline{r}]\right\|^2\\ &\overset{(c)}{=} \frac{1}{N\sigma^2}\left\|\mathbf{Re}\,[\underline{r}] - \mathbf{L}\hat{\mu}_X\right\|^2\\ &\overset{(d)}{=} \frac{1}{N\sigma^2}\sum_{k=1}^{M}\left(\mathbf{Re}\,[r_k] - \hat{\mu}_X\right)^2,\end{aligned} \tag{B.10}$$

where in step (a), we have used the definition of idempotent and symmetric matrices [4], in step (b), we have used (B.5), in step (c), we have employed (4.11), and in step (d), we have used (B.6) and applied the Euclidean norm. Observe that ω_1 and ω_2 are the first terms of (4.21) and (4.22), respectively. The same approach can also be applied to prove the independence between the second terms. Finally, since $\mathbf{Re}\left[r_k\right]$ and $\mathbf{Im}\left[r_k\right]$ are also independent statistics (cf. Section 4.3.1), then $\mathcal{I}_1$ and $\mathcal{I}_2$ are mutually independent RVs, which completes the proof.

B.3 Derivation of (4.25)

To prove (4.25), we make use of the doubly noncentral F-distribution, defined as [5]

$$f_Z\left(z|\mathcal{H}_1\right) = \sum_{k=0}^{\infty}\sum_{l=0}^{\infty} \frac{z^{-1}\exp\left[\frac{-\lambda_1-\lambda_2}{2}\right]\left(\frac{\alpha_1 z}{\alpha_1 z+\alpha_2}\right)^{\frac{\alpha_1}{2}}\left(\frac{\alpha_2}{\alpha_1 z+\alpha_2}\right)^{\frac{\alpha_2}{2}}\left(\frac{\lambda_1\alpha_1 z}{2(\alpha_1 z+\alpha_2)}\right)^{k}\left(\frac{\lambda_2\alpha_2}{2(\alpha_1 z+\alpha_2)}\right)^{l}}{k!\; l!\; B\left(k+\frac{\alpha_1}{2}, l+\frac{\alpha_2}{2}\right)} \tag{B.11}$$

Rearranging some terms, and after applying [6, Eq. (07.20.02.0001.01)], (B.11) simplifies to

$$\begin{aligned} f_Z\left(z|\mathcal{H}_1\right) =& z^{-1}\exp\left[\frac{-\lambda_1-\lambda_2}{2}\right]\left(\frac{\alpha_1 z}{\alpha_1 z+\alpha_2}\right)^{\frac{\alpha_1}{2}}\left(\frac{\alpha_2}{\alpha_1 z+\alpha_2}\right)^{\frac{\alpha_2}{2}}\sum_{k=0}^{\infty}\left\{\left(\frac{\lambda_1\alpha_1 z}{2\alpha_1 z+2\alpha_2}\right)^{k}\right. \\ &\left.\times\frac{{}_1F_1\left(\frac{1}{2}\left(2k+\alpha_1+\alpha_2\right); \frac{\alpha_2}{2}; \frac{\alpha_2\lambda_2}{2(z\alpha_1+\alpha_2)}\right)}{k!\; B\left(k+\frac{\alpha_1}{2}, \frac{\alpha_2}{2}\right)}\right\}. \end{aligned} \tag{B.12}$$

Now, replacing $\alpha_1 = 2$, $\alpha_2 = 2(M-1)$, $\lambda_1 = M(\mu_X^2+\mu_Y^2)/N\sigma^2$, and $\lambda_2 = 0$ (cf. Section 4.4.1) in (B.12), and after applying [7, Eq. (15.2.1)], and [7, Eq. (5.12.1)], we obtain

$$f_Z\left(z|\mathcal{H}_1\right) = \frac{\exp\left[-\frac{M\left(\mu_X^2+\mu_Y^2\right)}{2N\sigma^2}\right]}{\Gamma(M)}\left(\frac{M-1}{M+z-1}\right)^{M}\sum_{k=0}^{\infty}\frac{\Gamma(k+M)}{\Gamma(k+1)^2}\left(\frac{Mz\left(\mu_X^2+\mu_Y^2\right)}{2N\sigma^2(M+z-1)}\right)^{k}. \tag{B.13}$$

Finally, after using the definition of the Kummer confluent hypergeometric function [6, Eq. (07.20.02.0001.01)], along with minor simplifications, we obtain (4.25), which completes the derivation.

APPENDIX C – Supporting Material for Chapter 5

C.1 MATHEMATICA'S Implementation for the Bivariate Fox H-function

```
ClearAll["Global`*"]; Remove[s];
H[x_, delta_, D_,beta_, B_]
 := Module[{UpP, LoP, Theta,R1, T1, R2, T2, m, n},
 L=Length[Transpose[D]]; (*L represents the dimension of the
 Fox's H-function*)
 m=Length[D];(*Number of Gamma functions in the numerator*)
 n=Length[B];(*Number of Gamma functions in the denominator*)
 S=Table[Subscript[s,i],{i,1,L}];(*s is the
 vector containing the number of branches, in our case s=[s_1,s_2]*)
 UpP=Product[Gamma[delta[[1,j]]+Sum[D[[j,k]]
     S[[k]],{k,1, L}]], {j,1,m}];
 LoP=Product[Gamma[beta[[1,j]]+Sum[B[[j,k]]
     S[[k]],{k,1,L}]],{j,1,n}];
 Theta=UpP/LoP (*Theta computes Eq. (2)*);
 W=50; (*Limit for the complex integration*)
  T=Table[delta[[1,j]]+Sum[D[[j,k]]
  S[[k]],{k,1,L}]>0,{j,1,m}]; (*Generates a restriction table*)
 R1=Reduce[And@@Flatten[{T[[1]],T[[3]]}]];
 (*R1 computes the real interval that separates the poles of
 Gamma[s_1] from the poles of Gamma[M-1-s_1] and Gamma[M-s_1-s_2]*)
 T1=Mean[{First@R1,Last@R1}];
 R2=Reduce[And@@Flatten[{T[[2]],T[[4]]}]];
 (*R2 computes the real interval that separates the poles of
 Gamma[s_2] from the poles of Gamma[M-s_1-s_2]*)
 T2=Mean[{First@R2,Last@R2}];
 kernel=Theta(x[[1,1]])^(-S[[1]])(x[[1,2]])^(-S[[2]])
   /.{S[[1]]->s1,S[[2]]->s2}; (*Prepare the Kernel
   for Mathematica's Integration*)
 N[1/(2*Pi*I)^2 NIntegrate[kernel,{s1,T1-I W,T1+I W},
 {s2,T2-I W,T2+I W}],20]]
```

APPENDIX D – Supporting Material for Chapter 7

D.1 Proof of Proposition I

Applying [8, Eq. (5.48)] and using the fact that $X_{k,i}$ and $Y_{l,i}$ are independent RVs, (7.30) can be rewritten as follows:

$$\mathrm{PD}_i = \int_0^\infty \int_0^\infty \left(\prod_{k=1}^{M_i-1} \Pr\left[X_{k,i} < r_{1,i} | R_{1,i} = r_{1,i}\right] \right) \times \left(\prod_{l=1}^{N_i-1} \Pr\left[Y_{l,i} < r_{2,i} | R_{2,i} = r_{2,i}\right] \right) \times f_{R_{1,i},R_{2,i}}(r_{1,i}, r_{2,i})\, \mathrm{d}r_{1,i}\, \mathrm{d}r_{2,i}. \tag{D.1}$$

Now, with the aid of [8, Eq. (4.11)] and taking into account that $X_{k,i}$ and $Y_{l,i}$ are identically distributed RVs, yields

$$\mathrm{PD}_i = \int_0^\infty \int_0^\infty \left(\int_0^{r_{1,i}} f_{X_{1,i}}(x_{1,i})\, \mathrm{d}x_{1,i} \right)^{M_i-1} \left(\int_0^{r_{2,i}} f_{Y_{1,i}}(y_{1,i})\, \mathrm{d}y_{1,i} \right)^{N_i-1} \times f_{R_{1,i},R_{2,i}}(r_{1,i}, r_{2,i})\, \mathrm{d}r_{1,i}\, \mathrm{d}r_{2,i}. \tag{D.2}$$

Replacing (7.22)–(7.24) in (D.2), we obtain

$$\mathrm{PD}_i = \int_0^\infty \int_0^\infty \underbrace{\left(\int_0^{r_{1,i}} \frac{x_{1,i} \exp\left(-\frac{x_{1,i}^2}{2\sigma_{1,i}^2}\right)}{\sigma_{1,i}} \mathrm{d}x_{1,i} \right)^{M_i-1}}_{\triangleq\, \mathcal{I}_1} \underbrace{\left(\int_0^{r_{2,i}} \frac{y_{1,i} \exp\left(-\frac{y_{1,i}^2}{2\sigma_{2,i}^2}\right)}{\sigma_{2,i}} \mathrm{d}y_{1,i} \right)^{N_i-1}}_{\triangleq\, \mathcal{I}_2} \times \int_0^\infty \exp(-\xi_i t) \exp\left(-\mathbf{m}_i\right) I_0\left(2\sqrt{\mathbf{m}_i t}\right) \prod_{p=1}^{2} \frac{r_{p,i}}{\Omega_{p,i}^2} \exp\left(-\frac{r_{p,i}^2}{2\Omega_{p,i}^2}\right) \times I_0\left(\frac{r_{p,i}\sqrt{t\sigma_{p,i}^2\lambda_{p,i}^2}}{\Omega_{p,i}^2}\right) \mathrm{d}t\, \mathrm{d}r_{1,i}\, \mathrm{d}r_{2,i}. \tag{D.3}$$

In order to solve (D.3), we must first evaluate $\mathcal{I}_1$ and $\mathcal{I}_2$. In particular, $\mathcal{I}_1$ can be calculated as follows:

$$\begin{aligned} \mathcal{I}_1 &\overset{(a)}{=} \left(1 - \exp\left(-\frac{r_{1,i}^2}{2\sigma_{1,i}^2}\right)\right)^{M_i-1} \\ &\overset{(b)}{=} \sum_{k=0}^{M_i-1} \binom{M_i-1}{k} \left(-\exp\left(-\frac{r_{1,i}^2}{2\sigma_{1,i}^2}\right)\right)^{M_i-1-k}, \end{aligned} \tag{D.4}$$

where in step (a), we have developed the inner integral; and in step (b), we have used the binomial Theorem [8].

Using a similar approach to that used in (D.4), $\mathcal{I}_2$ can be calculated as

$$\mathcal{I}_2 = \sum_{l=0}^{N_i-1} \binom{N_i-1}{l} \left(-\exp\left(-\frac{r_{2,i}^2}{2\sigma_{2,i}^2}\right)\right)^{N_i-1-l}. \tag{D.5}$$

Inserting (D.4) and (D.5) in (D.3), followed by changing the order of integration[1] and along with minor manipulations, we obtain

$$\begin{aligned}\mathrm{PD}_i = \sum_{k=0}^{M_i-1}\sum_{l=0}^{N_i-1} 1^{k+l}\binom{M_i-1}{k}\binom{N_i-1}{l}\int_0^\infty \exp(-\xi_i t)\exp\left(-\mathbf{m}_i\right) I_0\left(2\sqrt{\mathbf{m}_i t}\right)\\ \times \underbrace{\int_0^\infty \left(-\exp\left(-\frac{r_{1,i}^2}{2\sigma_{1,i}^2}\right)\right)^{M_i-1-k} \frac{r_{1,i}}{\Omega_{1,i}^2}\exp\left(-\frac{r_{1,i}^2}{2\Omega_{1,i}^2}\right) I_0\left(\frac{r_{1,i}\sqrt{t\sigma_{1,i}^2\lambda_{1,i}^2}}{\Omega_{1,i}^2}\right)\mathrm{d}r_{1,i}}_{\triangleq\, \mathcal{I}_3}\\ \times \underbrace{\int_0^\infty \left(-\exp\left(-\frac{r_{2,i}^2}{2\sigma_{2,i}^2}\right)\right)^{N_i-1-l} \frac{r_{2,i}}{\Omega_{2,i}^2}\exp\left(-\frac{r_{2,i}^2}{2\Omega_{2,i}^2}\right) I_0\left(\frac{r_{2,i}\sqrt{t\sigma_{2,i}^2\lambda_{2,i}^2}}{\Omega_{2,i}^2}\right)\mathrm{d}r_{2,i}}_{\triangleq\, \mathcal{I}_4}\mathrm{d}t.\end{aligned} \tag{D.6}$$

Now, it remains to find $\mathcal{I}_3$ and $\mathcal{I}_4$. More precisely, $\mathcal{I}_3$ can be computed as

$$\begin{aligned}\mathcal{I}_3 &\overset{(a)}{=} \int_0^\infty \left(-\exp\left(-\frac{r_{1,i}^2}{2\sigma_{1,i}^2}\right)\right)^{M_i-1-k}\frac{r_{1,i}}{\Omega_{1,i}^2}\exp\left(-\frac{r_{1,i}^2}{2\Omega_{1,i}^2}\right)\sum_{q=0}^{\infty}\frac{\left(\frac{r_{1,i}\sqrt{t\lambda_{1,i}^2\sigma_{1,i}^2}}{2\Omega_{1,i}^2}\right)^{2q}}{q!\,\Gamma(q+1)}\mathrm{d}r_{1,i}\\ &\overset{(b)}{=} \frac{(-1)^{-k+M_i+1}}{\Omega_{1,i}^2\left(\frac{-k+M_i-1}{\sigma_{1,i}^2}+\frac{1}{\Omega_{1,i}^2}\right)}\sum_{q=0}^{\infty}\frac{\left(\frac{t\lambda_{1,i}^2\sigma_{1,i}^4}{2\Omega_{1,i}^2\left(\Omega_{1,i}^2(-k+M_i-1)+\sigma_{1,i}^2\right)}\right)^q}{q!}\\ &\overset{(c)}{=} \frac{(-1)^{-k+M_i+1}}{\Omega_{1,i}^2\left(\frac{-k+M_i-1}{\sigma_{1,i}^2}+\frac{1}{\Omega_{1,i}^2}\right)}\exp\left(\frac{t\lambda_{1,i}^2\sigma_{1,i}^4}{2\Omega_{1,i}^2\left(\Omega_{1,i}^2(-k+M_i-1)+\sigma_{1,i}^2\right)}\right),\end{aligned} \tag{D.7}$$

where in step (a), we have used the series representation of the modified Bessel function of the first kind and order zero [6, Eq. (03.02.02.0001.01)]; in step (b), we have solved the integral by first changing the order of integration; finally, in step (c), we have used [6, Eq. (01.03.06.0002.01)] and performed some algebraic manipulations.

In like manner as in (D.7), $\mathcal{I}_4$ can be computed as

$$\mathcal{I}_4 = \frac{(-1)^{-l+N_i+1}}{\Omega_{2,i}^2\left(\frac{-l+N_i-1}{\sigma_{2,i}^2}+\frac{1}{\Omega_{2,i}^2}\right)}\exp\left(\frac{t\lambda_{2,i}^2\sigma_{2,i}^4}{2\Omega_{2,i}^2\left(\Omega_{2,i}^2(-l+N_i-1)+\sigma_{2,i}^2\right)}\right). \tag{D.8}$$

[1] The change in the order of integration was performed without loss of generality since (7.22), (7.23) and (7.24) are non-negative real functions [9].

Now, replacing (D.7) and (D.8) in (D.6), we obtain

$$\begin{aligned}\mathrm{PD}_i = &\sum_{k=0}^{M_i-1}\sum_{l=0}^{N_i-1}\binom{M_i-1}{k}\binom{N_i-1}{l}\exp\left(-\mathbf{m}_i\right)\left(\frac{\sigma_{1,i}^2(-1)^{-k+M_i+1}}{\Omega_{1,i}^2(-k+M_i-1)+\sigma_{1,i}^2}\right)\\ &\times\left(\frac{\sigma_{2,i}^2(-1)^{-l+N_i+1}}{\Omega_{2,i}^2(-l+N_i-1)+\sigma_{2,i}^2}\right)\int_0^\infty \exp(-\xi_i t)I_0\left(2\sqrt{\mathbf{m}_i t}\right)\\ &\times\exp\left(\frac{t\lambda_{1,i}^2\sigma_{1,i}^4}{2\Omega_{1,i}^2\left(\Omega_{1,i}^2(-k+M_i-1)+\sigma_{1,i}^2\right)}\right)\\ &\times\exp\left(\frac{t\lambda_{2,i}^2\sigma_{2,i}^4}{2\Omega_{2,i}^2\left(\Omega_{2,i}^2(-l+N_i-1)+\sigma_{2,i}^2\right)}\right)\mathrm{d}t. \end{aligned} \tag{D.9}$$

Finally, using the following identity [10, Eq. (1.11.2.4)]

$$\int_0^\infty \exp(tb)I_0(\sqrt{t}a)\ \mathrm{d}t = -\frac{\exp\left(-\frac{a^2}{4b}\right)}{b}, \tag{D.10}$$

and after performing some minor simplifications, we can express (D.9) in closed-form as in (7.31), which completes the proof.

D.2 Proof of Corollary I

By making use of [8, Coroll. 6], we can express (7.33) as

$$\begin{aligned}\mathrm{PFA}_i = &\sum_{k=1}^{M_i-1}\sum_{l=1}^{N_i-1}\Pr\left[\mathcal{C}_{k,i}\bigcap\mathcal{D}_{l,i}\right]\\ &-\sum_{k=1}^{M_i-1}\sum_{\substack{l=1\\k<p,l<q}}^{N_i-1}\sum_{p=2}^{M_i-1}\sum_{q=2}^{N_i-1}\Pr\left[\mathcal{C}_{k,i}\bigcap\mathcal{D}_{l,i}\bigcap\mathcal{C}_{p,i}\bigcap\mathcal{D}_{q,i}\right]+\cdots\\ &+(-1)^{M_i-N_i-1}\Pr\left[\mathcal{C}_{1,i}\bigcap\mathcal{D}_{1,i}\bigcap\ldots\bigcap\mathcal{C}_{M_i-1,i}\bigcap\mathcal{D}_{N_i-1,i}\right]. \end{aligned} \tag{D.11}$$

Now, we need to find the event probabilities. First, let us derive the last event probability of (D.11), that is,

$$\begin{aligned}\Pr\left[\mathcal{C}_{1,i}\bigcap\mathcal{D}_{1,i}\bigcap\ldots\bigcap\mathcal{C}_{M_i-1,i}\bigcap\mathcal{D}_{N_i-1,i}\right] &\overset{a}{=}\int_0^\infty\int_0^\infty\left(\prod_{k=1}^{M_i-1}\Pr\left[X_{k,i}>r_{1,i}|R_{1,i}=r_{1,i}\right]\right)\\ &\times\left(\prod_{l=1}^{N_i-1}\Pr\left[Y_{l,i}>r_{2,i}|R_{2,i}=r_{2,i}\right]\right)f_{R_{1,i},R_{2,i}}(r_{1,i},r_{2,i})\ \mathrm{d}r_{1,i}\ \mathrm{d}r_{2,i}\\ &\overset{b}{=}\int_0^\infty\int_0^\infty\left(\int_{r_{1,i}}^\infty f_{X_{1,i}}(x_{1,i})\ \mathrm{d}x_{1,i}\right)^{M_i-1}\left(\int_{r_{2,i}}^\infty f_{Y_{1,i}}(y_{1,i})\ \mathrm{d}y_{1,i}\right)^{N_i-1}\\ &\times f_{R_{1,i},R_{2,i}}(r_{1,i},r_{2,i})\ \mathrm{d}r_{1,i}\ \mathrm{d}r_{2,i}, \end{aligned} \tag{D.12}$$

where in step (a) we have used [8, Eq. (5.48)]; and in step (b) we have used [8, Eq. (4.11)] along with the fact that $X_{k,i}$ and $Y_{l,i}$ are identically distributed RVs.

Replacing (7.22)–(7.24) in (D.12), yields

$$\Pr\left[\mathcal{C}_{1,i}\bigcap\mathcal{D}_{1,i}\bigcap\ldots\bigcap\mathcal{C}_{M_i-1,i}\bigcap\mathcal{D}_{N_i-1,i}\right]=\int_0^\infty\int_0^\infty\underbrace{\left(\int_{r_{1,i}}^\infty\frac{x_{1,i}\exp\left(-\frac{x_{1,i}^2}{2\sigma_{1,i}^2}\right)}{\sigma_{1,i}}\mathrm{d}x_{1,i}\right)^{M_i-1}}_{\triangleq\ \mathcal{I}_5}$$
$$\times\underbrace{\left(\int_{r_{2,i}}^\infty\frac{y_{1,i}\exp\left(-\frac{y_{1,i}^2}{2\sigma_{2,i}^2}\right)}{\sigma_{2,i}}\mathrm{d}y_{1,i}\right)^{N_i-1}}_{\triangleq\ \mathcal{I}_6}\int_0^\infty\exp(-\xi_i t)\exp\left(-\mathbf{m}_i\right)I_0\left(2\sqrt{\mathbf{m}_i t}\right)$$
$$\times\prod_{p=1}^{2}\frac{r_{p,i}}{\Omega_{p,i}^2}\exp\left(-\frac{r_{p,i}^2}{2\Omega_{p,i}^2}\right)I_0\left(\frac{r_{p,i}\sqrt{t\sigma_{p,i}^2\lambda_{p,i}^2}}{\Omega_{p,i}^2}\right)\mathrm{d}t\ \mathrm{d}r_{1,i}\ \mathrm{d}r_{2,i}. \tag{D.13}$$

After some mathematical manipulations, $\mathcal{I}_5$ and $\mathcal{I}_6$ can be calculated, respectively, as

$$\mathcal{I}_5=\exp\left(-\frac{r_{1,i}^2(M_i-1)}{2\sigma_{1,i}^2}\right) \tag{D.14}$$

$$\mathcal{I}_6=\exp\left(-\frac{r_{2,i}^2(N_i-1)}{2\sigma_{2,i}^2}\right). \tag{D.15}$$

Now, replacing (D.14) and (D.15) in (D.13), and after solving remaining three integrals by applying the same procedure as in (D.9), we obtain

$$\Pr\left[\mathcal{C}_{1,i}\bigcap\mathcal{D}_{1,i}\bigcap\ldots\bigcap\mathcal{C}_{M_i-1,i}\bigcap\mathcal{D}_{N_i-1,i}\right]=\frac{\mathcal{Q}_i\left(M_i-1,N_i-1\right)}{\mathcal{P}_i\left(M_i-1,N_i-1\right)}$$
$$\times\exp\left(-\mathbf{m}_i+\frac{\mathbf{m}_i}{\mathcal{P}_i\left(M_i-1,N_i-1\right)}\right), \tag{D.16}$$

where $\mathcal{P}_i\left(k,l\right)$ and $\mathcal{Q}_i\left(k,l\right)$ are auxiliary functions defined in (7.35), and the parameters $k\in\{1,2,\ldots,M_i-1\}$ and $l\in\{1,2,\ldots,N_i-1\}$ denote the number of events for $\mathcal{C}_{k,i}$ and $\mathcal{D}_{l,i}$, respectively. Thus, the remaining event probabilities in (D.11) can be easily obtained by a proper choice of the parameters k and l. For example, for $k=1$ and $l=3$, we obtain

$$\Pr\left[\mathcal{C}_{1,i}\bigcap\mathcal{D}_{1,i}\bigcap\mathcal{D}_{2,i}\bigcap\mathcal{D}_{3,i}\right]=\frac{\mathcal{Q}_i\left(1,3\right)}{\mathcal{P}_i\left(1,3\right)}\exp\left(-\mathbf{m}_i+\frac{\mathbf{m}_i}{\mathcal{P}_i\left(1,3\right)}\right), \tag{D.17}$$

whereas for $k=3$ and $l=2$, we have

$$\Pr\left[\mathcal{C}_{1,i}\bigcap\mathcal{D}_{1,i}\bigcap\mathcal{C}_{2,i}\bigcap\mathcal{D}_{2,i}\bigcap\mathcal{C}_{3,i}\right]=\frac{\mathcal{Q}_i\left(3,2\right)}{\mathcal{P}_i\left(3,2\right)}\exp\left(-\mathbf{m}_i+\frac{\mathbf{m}_i}{\mathcal{P}_i\left(3,2\right)}\right). \tag{D.18}$$

Later, with the aid of (D.16) and after some algebraic manipulations, we can rewrite (D.11) as

$$\mathrm{PFA}_i=\binom{M_i-1}{1}\binom{N_i-1}{1}\frac{\mathcal{Q}_i\left(1,1\right)}{\mathcal{P}_i\left(1,1\right)}\exp\left(-\mathbf{m}_i+\frac{\mathbf{m}_i}{\mathcal{P}_i\left(1,1\right)}\right)-\binom{M_i-1}{2}\binom{N_i-1}{2}$$
$$\times\frac{\mathcal{Q}_i\left(2,2\right)}{\mathcal{P}_i\left(2,2\right)}\exp\left(-\mathbf{m}_i+\frac{\mathbf{m}_i}{\mathcal{P}_i\left(2,2\right)}\right)+\cdots+(-1)^{M_i-N_i-1}\binom{M_i-1}{M_i-1}\binom{N_i-1}{N_i-1}$$
$$\times\frac{\mathcal{Q}_i\left(M_i-1,N_i-1\right)}{\mathcal{P}_i\left(M_i-1,N_i-1\right)}\exp\left(-\mathbf{m}_i+\frac{\mathbf{m}_i}{\mathcal{P}_i\left(M_i-1,N_i-1\right)}\right). \tag{D.19}$$

Finally, and after minor simplifications, (D.19) reduces to (7.34), which completes the proof.

D.3 Bibliography

[1] S. A. Hovanessian, "An algorithm for calculation of range in a multiple PRF radar," *IEEE Trans. Aerosp. Electron. Syst.*, vol. AES-12, no. 2, pp. 287–290, Mar. 1976.

[2] A. Papoulis, *Probability, Random Variables, and Stochastic Processes*, 4th ed. Ney York, NY, USA: McGraw-Hill, 2002.

[3] W. G. Cochran, "The distribution of quadratic forms in a normal system, with applications to the analysis of covariance," *Proc. Camb. Phil. Soc.*, vol. 30, no. 2, p. 178–191, 1934.

[4] M. D. Springer, *The Algebra of Random Variables*. New York, NY, USA: Wiley, 1979.

[5] W. G. Bulgren, "On representations of the doubly non-central F distribution," *J. Amer. Statist.*, vol. 66, no. 333, pp. 184–186, Mar. 1971.

[6] Wolfram Research, Inc. (2018), *Wolfram Research*, Accessed: Sept. 19, 2020. [Online]. Available: http://functions.wolfram.com

[7] F. W. J. Olver, D. W. Lozier, R. F. Boisvert, and C. W. Clark, *NIST Handbook of Mathematical Functions*, 1st ed. Washington, DC: US Dept. of Commerce: National Institute of Standards and Technology (NIST), 2010.

[8] A. Leon-Garcia, *Probability and Random Processes for Electrical Engineering*, 3rd ed. New Jersey, NJ, USA: Pearson Prentice Hall, 1994.

[9] H. Friedman, "A consistent Fubini-Tonelli theorem for nonmeasurable functions," *Illinois J. Math.*, vol. 24, no. 3, pp. 390–395, 1980.

[10] A. P. Prudnikov, Y. A. Bryčkov, and O. I. Maričev, *Integral and Series: Vol. 2*, 2nd ed., Fizmatlit, Ed. Moscow, Russia: Fizmatlit, 1992.